

Fall 12-1-2015

Effects of Expected Service Life Exposures on the Functional Properties and Impact Performance of an American Football Helmet Outer Shell Material

David E. Krzeminski
University of Southern Mississippi

Follow this and additional works at: <https://aquila.usm.edu/dissertations>

 Part of the [Polymer and Organic Materials Commons](#), and the [Sports Sciences Commons](#)

Recommended Citation

Krzeminski, David E., "Effects of Expected Service Life Exposures on the Functional Properties and Impact Performance of an American Football Helmet Outer Shell Material" (2015). *Dissertations*. 168.
<https://aquila.usm.edu/dissertations/168>

This Dissertation is brought to you for free and open access by The Aquila Digital Community. It has been accepted for inclusion in Dissertations by an authorized administrator of The Aquila Digital Community. For more information, please contact Joshua.Cromwell@usm.edu.

The University of Southern Mississippi

EFFECTS OF EXPECTED SERVICE LIFE EXPOSURES
ON THE FUNCTIONAL PROPERTIES AND IMPACT PERFORMANCE
OF AN AMERICAN FOOTBALL HELMET OUTER SHELL MATERIAL

by

David Edward Krzeminski

Abstract of a Dissertation
Submitted to the Graduate School
of The University of Southern Mississippi
in Partial Fulfillment of the Requirements
for the Degree of Doctor of Philosophy

December 2015

ABSTRACT

EFFECTS OF EXPECTED SERVICE LIFE EXPOSURES
ON THE FUNCTIONAL PROPERTIES AND IMPACT PERFORMANCE
OF AN AMERICAN FOOTBALL HELMET OUTER SHELL MATERIAL

by David Edward Krzeminski

December 2015

The purpose of this dissertation is to gain a greater scientific understanding of the changes in functional material properties and impact performance of an American football helmet outer shell material under expected service life exposures. The research goals are to (i) quantify chemical, physical, thermal, and mechanical degradation of an American football outer shell material under expected environmental conditions and (ii) develop a linear drop test impact protocol to employ expected on-field impact conditions to American football helmet components and a plaque-foam (i.e., shell-liner) surrogate. Overall, a step-wise progression of analysis was demonstrated to concurrently quantify and understand changes in material properties at the molecular, microscopic, and macroscopic levels. Changes across chemical, physical, thermal, and mechanical properties were evaluated following laboratory exposures to 480 hours of accelerated weathering, increasing intensities of n-Butyl acetate solvent, and 12 repetitive linear plaque-foam impacts.

In Chapter II, an instrumented drop test setup was substantiated to investigate linear impact attenuation performance. In Chapter III, laboratory exposure to UV light, oxygen, moisture, and elevated temperatures induced molecular degradative bi-products and physical aging up to ~1% into the plaque thickness which led to altered aesthetic

properties, chemi-crystallization, and an increased resistance to surface indentation and tensile deformation. In Chapter IV, solvent-induced plasticization, crystallization, and stress-cracking of up to ~3% into the plaque thickness led to an increase in surface porosity which scattered light and decreased tensile properties. In Chapter V, impact exposure induced rubber-toughener (RT) cavitation that generated voids via delamination at the RT-matrix interface at which led to rings of stress-whitening, strain-induced crystallization, increased butadiene RT density, and shifts surface modulus and tensile properties. This dissertation preliminarily substantiated (i) a drop test setup attempting to accurately replicate on-field impact conditions to investigate linear impact attenuation performance, and (ii) polymer techniques and protocols that could elucidate the rates and degrees of material degradation.

COPYRIGHT BY
DAVID EDWARD KRZEMINSKI
2015

EFFECTS OF EXPECTED SERVICE LIFE EXPOSURES ON
THE FUNCTIONAL PROPERTIES AND IMPACT PERFORMANCE OF
AN AMERICAN FOOTBALL HELMET OUTER SHELL MATERIAL

by

David Edward Krzeminski

A Dissertation
Submitted to the Graduate School
the Schools of Kinesiology and
Polymers and High Performance Materials
at The University of Southern Mississippi
in Partial Fulfillment of the Requirements
for the Degree of Doctor of Philosophy

Approved:

Dr. Scott G. Piland, Committee Co-Chair
Associate Professor, School of Kinesiology

Dr. James W. Rawlins, Committee Co-Chair
Associate Professor, School of Polymers and High Performance Materials

Dr. Sergei I. Nazarenko, Committee Member
Associate Professor, School of Polymers and High Performance Materials

Dr. Trenton E. Gould, Committee Member
Associate Professor, School of Kinesiology

Dr. Jeffrey S. Wiggins, Committee Member
Associate Professor, School of Polymers and High Performance Materials

Dr. Karen S. Coats
Dean of the Graduate School

December 2015

DEDICATION

This work is dedicated to my Mother and Father for their endless love, sacrifice, and support towards the pursuit and fulfillment of my education.

ACKNOWLEDGMENTS

First and foremost, I would like to acknowledge each of my co-advisors, Dr. Scott Piland and Dr. James Rawlins. Throughout your mentorship, each of you have challenged me to become a better scientist, and granted me the freedom to pursue my academic and personal interests. Most importantly, you never stopped supporting my pursuit of a Sports and High Performance Materials doctoral degree. I would also like to acknowledge Dr. Trenton Gould for his support and guidance as an additional pseudo-co-advisor. I would also like to thank additional members of my PhD committee, Dr. Jeffrey Wiggins and Dr. Sergei Nazarenko, for their contributions to my education.

I would like to acknowledge the financial support of the School of Kinesiology, the School of Polymers and High Performance Materials, and the Engineer Research and Development Center (ERDC W9132T-09-2-0019), as well as the Bayer Corporation and the Der-Tex Corporation for supplying materials. I would also like to thank the equipment operations staff of the University of Southern Mississippi football team, specifically Patrick Stewart and Zack Gatwood.

I would like to thank Nadine Lipka, for over the past 4 years you have been my friend, my colleague, and my partner. You have been my foundation every step of the way, and have enriched my life beyond what I ever thought was possible. I would also like to thank Jim Goetz, we started our paths together as graduate students from Day 1 and our friendship will forever be rooted in the memories of 101 and 807.

I would like to thank my sister Tanya, for teaching me the courage to speak even when my voice shakes, and being someone her little brother will always look up to. I would also like to thank my grandparents, for the countless sacrifices for their grandson.

I would like to thank my coaches Irv Sigler, Brett Kempema, and David Belowich, for teaching me the relentless pursuit of excellence, to execute the fundamentals to be successful, and that I, too, can be a champion. I would also like to thank Pat Snyder, Andy Douglass, Mike Bailey, Evan Powell, Brian Hunter, Gerry Mayer, Luis Vega, Brian McCarthy, Brian Belowich, Will Schmidt, Katie Benintende, Jess Woods, Jake Cook, Matt Medendorp, Mike Vandervelde, and Paul Reynolds.

Additional academic and personal contributions from numerous graduate students, faculty, and staff across the Schools of Polymers and Kinesiology also made this possible: Stephen Foster, Joshua Hanna, Brandon Achord, Stephanie (Messer) Foster, Pirro Cipi, Chrissy Caroselli, Kevin Harman, Greg Curtzwiler, Christina Konecki, Steven Wand, Eric Fowler, Stephen Heinz, Matt Jackson, Sam Tucker, Jeremy Decker, Adam Richardson, Travis Ball, Jake Ray, Olivia McNair, Ashely Johnson, Lea Paslay, Sarah Exley, Brooks Abel, Emily Hoff, Andrew Janisse, Maliha Syed, Kat Frank, Lauren Kucera, Brian Greenhoe, Kyler Knowles, Hanna Knowles, Greg Strange, Daniel Savin, Gary Krebs, Kim Luck, Kim Brandon, Kathy Lee, Debbie Kleckner, Michael Blanton, Dilhan Fernando, Sharathkumar Mendon, Monoj Pramanik, Eric Williams, Michael McDonald, Kevin Davis, Dwaine Braash, Thomas Harris, Kenton McNeese, and Ty Posey.

TABLE OF CONTENTS

ABSTRACT	ii
DEDICATION	iv
ACKNOWLEDGMENTS	v
LIST OF TABLES	ix
LIST OF ILLUSTRATIONS	xi
CHAPTER	
I. RESEARCH BACKGROUND	1
Introduction	
American Football Helmet Evolution	
Brain Injury of Concussion	
Football Helmet Testing	
Current Football Helmet Technologies	
Reconditioning and Recertification	
Service Life Exposures	
Helmet Impact Exposure	
Research Overview	
References	
II. INVESTIGATION OF LINEAR IMPACT ENERGY MANAGEMENT AND PRODUCT CLAIMS OF A NOVEL AMERICAN FOOTBALL HELMET LINER COMPONENT	27
Abstract	
Introduction	
Experimental	
Results	
Discussion	
Conclusions	
Supplemental Information	
References	
III. QUANTIFYING THE EFFECTS OF ACCELERATED WEATHERING AND LINEAR DROP IMPACT EXPOSURES OF AN AMERICAN FOOTBALL HELMET OUTER SHELL MATERIAL	50
Abstract	

	Introduction	
	Experimental	
	Results	
	Discussion	
	Conclusions	
	Supplemental Information	
	References	
IV.	EFFECTS OF SOLVENT EXPOSURE ON MATERIAL PROPERTIES AND IMPACT PERFORMANCE OF AN AMERICAN FOOTBALL HELMET OUTER SHELL MATERIAL	97
	Abstract	
	Introduction	
	Experimental	
	Results	
	Discussion	
	Conclusions	
	References	
V.	CHARACTERIZATION OF REPETITIVE LINEAR IMPACT EXPOSURE AND IMPACT-INDUCED STRESS-WHITENING OF AN AMERICAN FOOTBALL HELMET OUTER SHELL MATERIAL ...	125
	Abstract	
	Introduction	
	Experimental	
	Results	
	Discussion	
	Conclusions	
	References	
VI.	SUMMARY AND FUTURE WORK	176
	Summary	
	Future Work Introduction	
	Thermal Annealing	
	Infrared Thermography	
	Additive Helmet Technology	
	Monitoring in situ degradation	
	References	

LIST OF TABLES

Table

1.	Summary of football helmet policies and warranties across organizations	11
2.	Comparison of the prototype TWC component mean peak force values reported with air vent diameters of 2 and 3 mm (19) to mean F_{COLL} and F_{COMP} results of the off-the-shelf Xenith [®] X1 [™] shock absorber (air vent diameter: \bar{x} =2.3 mm)	39
3.	Summary of measurement techniques and statistical analyses performed	61
4.	Summary of statistical analyses with statistically significant outcomes	62
5.	MDSC Heat Flow thermogram peak temperatures across plaque surface conditions.....	66
6.	MDSC Heat Flow thermogram peak areas across plaque surface conditions	68
7.	MDSC Reversible and Non-reversible thermogram step change temperatures across plaque surface conditions.....	68
8.	Tensile mechanical properties between plaque conditions	70
9.	Summary of measurement techniques, independent and dependent variables, sample sizes, and statistical analysis performed	104
10.	L* whiteness values across solvent exposures.....	105
11.	Thickness of surface swelling across solvent exposures	106
12.	MDSC thermogram peak areas and temperatures across solvent exposures	108
13.	Tensile properties across solvent exposures	109
14.	Linear drop test peak force across solvent exposures	110
15.	Summary of measurement techniques and statistical analyses performed	135
16.	Summary of statistical analyses with statistically significant outcomes	136
17.	Heating ramp reversible and non-reversible MDSC thermogram peak temperatures and areas between plaque conditions	140
18.	Cooling and heating ramp reversible and non-reversible MDSC thermogram	

	step change temperatures between plaque conditions	141
19.	DMA thermogram temperatures, areas, heights, and widths between plaque conditions for Region 1 (85 to -65 °C)	142
20.	DMA thermogram temperatures between plaque conditions for Region 2 (70 to 85 °C) and Region 3 (135 to 155 °C)	142
21.	TMA thermogram temperatures and heights between plaque conditions	145
22.	TMA thermogram slopes between plaque conditions	145
23.	Tensile mechanical properties between plaque conditions	147
24.	Tensile properties across material conditions	185
25.	Impact performance parameters across sample conditions for anvil-only setup.....	191
26.	Impact performance parameters across sample conditions for plaque-foam setup	192

LIST OF ILLUSTRATIONS

Figure

1.	Schematic of NOCSAE (top) linear drop test setup and (bottom) proposed pneumatic ram test used for helmet testing.....	7
2.	Schematic of the myriad of service life exposures on a football helmet outer shell under expected on-field use and storage.	12
3.	Xenith® X1™ football helmet with revealed liner system and single Aware-Flow® shock absorber	30
4.	Schematic of Xenith® X1™ Aware-Flow® shock absorber and corresponding air vent location.....	30
5.	Instron® Dynatup® 9250HV instrumented drop tower system	33
6.	Impulse curve progression for increasing impact velocities.....	35
7.	(a) SA _{Pad} and (b) SA _{No Pad} time-averaged impulse curves of first impact trials.....	35
8.	(a) SA _{Pad} and (b) SA _{No Pad} time-averaged impulse curves for 1.3 – 3.0 m/sec.....	36
9.	Maximum SA _{Pad} compression behavior and percent compression across increasing impact velocities.....	36
10.	(a) Mean peak collapse forces and (b) mean peak compression forces for repetitive impact testing of SA _{Pad} and SA _{No Pad} at 3.0 and 4.0 m/sec.....	37
11.	(a) SA _{Pad} and (b) SA _{No Pad} impulse curve shape progression at 3.0 m/sec for a single absorber across 15 repetitive trials	38
12.	SA _{Pad} characteristic phases of the time-averaged impulse curve at 4.0 m/sec.....	40
13.	Schematic of (a) hexagonal cells in a cellular solid and (b) a redrawn compressive stress-strain curve of array of identical hexagonal cells or a polymeric elastic-plastic foam.....	40
14.	SA _{Pad} impact progression at 4.0 m/sec.....	42
15.	Common American football helmet components: (left) vinyl nitrile foam inner liner and (right) injection molded polycarbonate blend outer shell	52

16.	Chemical structures of the primary polymers, (left) bisphenol A polycarbonate and (right) polyethylene terephthalate that comprise the engineered outer shell helmet-grade blend material	56
17.	(left) UV spectrum of direct terrestrial sunlight compared to radiation spectrum of UVA-340 nm lamp (33, 34). (right) QUV Accelerated Weathering tester shown with weathered plaques under UV radiation (illuminated 2.5" x 4.0" area)	57
18.	Instron Dynatup 9250HV instrumented drop tower system shown with plaque-foam helmet surrogate system at pre-impact.	60
19.	(left) Example of (a) Non-W plaque, (b) W _{EXPOSED} with yellow discoloration of exposed area bracketed, (c) inverted image to highlight the visible area of discoloration. (right) Yellowing Index across plaque surface conditions.....	63
20.	Full ATR-IR spectra across plaque surface conditions. Inset spectra showcase the differential of Non-W and W _{EXPOSED} area specific to alkyl composition consumption (\downarrow -CH _x) at 3000-2800 cm ⁻¹ and carbonyl linkage(s) formation (\uparrow -C=O) at 1800-1600 cm ⁻¹	65
21.	Fluorescence response (350 nm last light source) across plaque surface conditions. Only the W _{EXPOSED} surface exhibited a fluorescence emission (illuminated depth of ~30-35 μ m)	65
22.	MDSC thermograms across plaque surface conditions for (a) total heat flow, (b) non-reversible heat flow, and (c) reversible heat flow. Note: The general locations of the six distinctive bands are highlighted in the total heat flow plot...67	67
23.	Reduced modulus as a function of depth of surface penetration across plaque surface conditions	69
24.	Stress-strain curves for (left) Non-weathered and (right) Weathered plaque conditions.....	70
25.	(left) Smoothed force-time curves for a single representative Weathered plaque-foam system across five repetitive impact trials. (right) Peak force and time to peak force across five repetitive trials on Weathered and Non-weathered plaque-foam systems.....	71
26.	(left) Maximum compression and deformation of plaque-foam system during an impact test. (right) Backside of a Weathered plaque after five impact trials displaying impact-induced rings of whitening.....	71
27.	Full ATR-IR spectra between a helmet-grade plaque and an off-the-shelf outer shell	86

28.	TGA thermogram of a procured pellet at a heating rate of 10 °C/min in air. Blend composition is shown to be approximately equal amounts of PC and PET.	86
29.	Instron Dynatup 9250 HV instrumented drop tower system shown with a Pristine plaque-foam helmet surrogate system at pre-impact	103
30.	Solvent-exposed plaque surfaces (left-to-right): Pristine, Spray (3 coats), 5 mL Pool, Immerse - 1 hr, and Immerse - 2 hr	105
31.	Cross-section of Immerse - 1 hr plaque surface showcasing the non-solvent/solvent boundary and thickness of surface swelling.....	106
32.	SEM surface images for (left) Pristine and (right) Immerse - 1 hr.	107
33.	MDSC total heat flow thermograms across the solvent exposures of Pristine, 5mL Pool, and Immerse – 1 hr. Note: The general locations of the eight notable bands are highlighted.	107
34.	(left) Immerse – 1hr plaque showcasing the location and shape of the harvested tensile specimen. (right) Stress-strain curves across solvent exposures.	109
35.	Smoothed force-time curves of single plaque-foam systems across solvent exposures.....	110
36.	(left) Maximum deformation of a Pristine plaque-foam system during impact; (right) Backside of Immerse – 1 hr post-impact, highlighting the impact-induced rings of whitening	110
37.	(A) Example of new collegiate American football helmet. (B and C) Areas of whitening were visually observed (circled) across the outside of helmet shells after one season of use. (D) Whitening was observed to transfer through to the inside of the outer shell.	128
38.	Instron Dynatup 9250 HV instrumented drop tower system shown with a football helmet surrogate plaque-foam system at pre-impact.	130
39.	Smoothed force-time curves for Trial 1 (history of zero impact trials) and Trial 12 (history of 11 impact trials) plaque-foam helmet surrogate systems.	137
40.	(left) Maximum compression and deformation of plaque-foam helmet surrogate system during a first impact trial. (middle) The backside of a Trial 1 plaque displaying impact-induced rings of whitening. (right) The backside of a Trial 12 plaque (i.e., Impacted plaque) displaying the increase in rings of whitening.....	138
41.	(left) Backside of an Impacted plaque showcasing the location and shape of the harvested specimen used for optical microscopy. (right) Comparison of Non-	

	impacted and Impacted specimens highlighting the uniform depth of whitening into the material, measured at $1.4 \text{ mm} \pm 0.1$. (Note: DMA specimens were produced by removing top $\sim 1.5 \text{ mm}$ of material via sanding).	139
42.	Scanning electron microscopy images of cryo-fracture surfaces of (left) Non-impacted and (right) Impacted outer shell plaque material.	139
43.	Non-reversible and reversible heat flow MDSC thermograms between Non-impacted and Impacted plaque conditions for (top) cooling ramp and (bottom) heating ramp. (Note: Difference in scale across y-axes.)	141
44.	DMA thermograms of (top) tan delta ($\text{Tan } \delta$), (middle) storage modulus (E'), and (bottom) loss modulus (E'') between Non-impacted and Impacted plaque conditions. Inset thermograms showcase the -100°C to -50°C temperature range for (top) $\text{Tan } \delta$, (middle) derivative of E' (dE'), and (bottom) E'' to highlight the consistent $\sim 5^\circ\text{C}$ shift upwards in Impacted peak temperatures for the selected signals.	143
45.	TMA thermograms between Non-impacted and Impacted plaque conditions. Inset thermograms showcase the -110 to -10°C temperature range to highlight the $\sim 5^\circ\text{C}$ shift upwards in Impacted onset temperature via the intersection point of traced slope lines.	144
46.	Reduced modulus as a function of depth of surface penetration at the backside surface between plaque conditions.	146
47.	(a) Stress-strain curves for Non-impacted and Impacted plaque conditions. (b) Backside of Impacted plaque showcasing the location and shape of the harvested tensile specimen. (c) (left) Non-impacted and (right) Impacted tensile samples post-test with Impacted samples retaining the impact-induced whitening, as well as preferentially yielding and failing along the whitened area.	147
48.	Impacted TMA specimen schematic showcasing the (left) harvested location and shape from an Impacted plaque; (middle) placement during TMA testing and the direction of the impact-oriented chains relative to the expansion probe; and (right) concurrent linear contraction perpendicular to the linear thermal expansion uniaxially measured by the expansion probe.	160
49.	Experimental schematic showing treatments and assessments ($n=5$) across material conditions. (% = Colorimetric test).	182
50.	(a) Backside of Impacted plaque after 12 trials, displaying impact-induced rings of whitening. (b) Backside of Impacted/Annealed plaque showcasing that annealing visually erased whitening. Dashed box: Location of harvested tensile sample. (c) Tensile sample harvested from Impacted/Annealed plaque. (d) Tensile test setup with annealed rings of whitening placed between clamps.	183

51.	(a) L* whiteness values across Pre-impact, Pre-anneal, and Post-anneal conditions (#=p<0.05). (b) Smoothed force-time curves of plaque-foam systems. (c) Trial 13 peak force for Impacted and Impacted/Annealed plaques.	184
52.	(left) Stress-strain curves across material conditions. (right) Impacted and Impacted/Annealed tensile samples post-test showcasing the differential preferential yielding behavior via location of whitening.	185
53.	Reduced modulus as a function of depth of surface penetration for (left) Non-impacted and (right) Impacted material conditions.	186
54.	IRT image showcasing (left) focal maximum temperature increase and (right) step-wise increase versus time of the backside of an impacted plaque.	188
55.	(left) Recommended placement of the Kevlar-PU Foam additive technology within a current American football helmet (Kevlar facing towards inner liner). (right) Separation of the system showcasing the PU Foam padding component and Kevlar fiber mesh component.	189
56.	Instrumented drop tower with plaque-foam helmet surrogate atop Kevlar-PU Foam at pre-impact.	190
57.	Smoothed force-time curves of single impacts across sample conditions for (left) Anvil-only setup and (right) Plaque-foam setup.....	191
58.	Full ATR-FTIR spectra of a helmet-grade plaque comparing Non-weathered Accelerated Weathering, and Natural Weathering conditions. Inset spectra showcase the differential across weathering conditions specific to alkyl composition (\downarrow -CH _x) at 3000-2800 cm ⁻¹ and carbonyl formation (\uparrow -C=O) at 1800-1600 cm ⁻¹	194
59.	Off-the-shelf football helmet outer shells from (left) Riddell and (right) Xenith fixtured into an ATR-FTIR spectrometer.	195
60.	Full ATR-IR spectra across a representative American football helmet outer shell model from each of the four major helmet manufacturers.	196
61.	(a) High definition photograph of deionized water droplet on a helmet outer shell. (b) Zoomed in and cropped image imported into DropSnake Software. (c) Output image of analysis highlighting the water contact angle measurement in blue.....	196
62.	TMA thermograms between a helmet-grade plaque and an off-the-shelf outer shell (Xenith X1).....	197

CHAPTER I

RESEARCH BACKGROUND

Introduction

Participation in contact sports across all levels carries a risk of sustaining a head injury through an impact event (1-4). In effort to mitigate the head injury risk to professional, amateur, and recreational athletes, the use of certified protective head gear is often recommended and even mandated during play (5-7). The ability of sport-specific helmets to provide adequate protection is often due to the maturity of the sport to identify controllable risk and establish standards for design and performance (8, 9). Specific to American football, the implementation of certified helmets has effectively decreased catastrophic head injuries (10) and reduced forces to the brain (11-13). However, there is no evidence to support that helmets mitigate or prevent the brain injury of concussion (11-13). Furthermore, there is no current helmet testing standard that has been established to address a sports-related concussive injury.

The high prevalence of concussion in American football has recently provoked legislative measures at federal and state levels (14-17), lawsuits by athletes against collegiate and professional football associations (18, 19), and funding opportunities to accelerate innovative solutions in the fields of concussion injury prevention, diagnosis, and prognosis (20). The deficiency in medical knowledge has run in parallel with a gap in biomechanical data to collectively result in an injury etiology that is not well understood and helmet technology that underperforms (8, 9, 11-13). Strong research efforts towards improved football helmet performance are focused on the (i) study of on-field impact conditions (21-23), (ii) development of new testing standards (22-24),

(iii) modeling of impact-induced brain deformation (25-27), and (iv) engineering of novel technologies (28). Yet, a review of the scientific literature revealed minimal peer-reviewed evidence to support current materials or components used for head protection (8, 9, 29). As a result, greater scientific understanding of how helmet systems, components, and constituent materials serve to manage the impact energies of play throughout service lifetimes is warranted and will be the focus of this dissertation.

American Football Helmet Evolution

Motivated by the prevalence of catastrophic injuries, American football players began to independently employ custom head protection in the late 1800s (30). Headgear constructed of hardened leather soon became prominent, leading to mandated use by the National Collegiate Athletic Association (NCAA) and the National Football League (NFL) by 1940 (30). Modifications followed as leather was replaced by a polycarbonate (PC) outer shell in the 1950s (10). Helmets then evolved to incorporate soft inner linings to provide wearer comfort and faceguards to prevent facial injuries (30); however, PC has remained the material of choice for football helmet outer shells for over 60 years.

Though headgear use was widespread during the mid-1900s, catastrophic cervical spine and head injuries in American football remained highly prevalent. Recorded fatalities totaled 109 within 1945 - 1954 and 138 within 1955 – 1964 (10). As a result, the National Operating Committee on Standards for Athletic Equipment (NOCSAE) was formed in 1969. NOCSAE was prompted to establish safety standards for helmets with a primary focus to prevent head-related football deaths. The brain injury of concussion, though currently important, lacked the understanding and sufficient scientific definition to be considered a dangerous injury. At the time, injuries without mortality rates were

considered acceptable outcomes, and thus were not addressed by NOCSAE (30). The initial NOCSAE football test standard was published in 1973, and helmets produced in 1974 were the first to undergo certification tests (31). By 1980, the wearing of certified helmets was mandatory for collegiate and high school athletes (31). While total deaths peaked at 204 from 1965 – 1974 (10), NOCSAE certification standards coupled with rule play changes and improved helmet designs (32-34), have directly resulted in the reduction of head-related deaths to an average of three per year (35, 36).

Modern American football helmet systems comprise two main protective components – the outer shell and the inner liner. Helmet shells are commonly constructed of injection-molded engineered PC blends which serve to delocalize focal impact energy by effectively distributing and transferring load to the liner system (37). The liner, commonly consisting of vinyl nitrile (VN) foams, thermoplastic polyurethane (TPU) structures, or pressurized gas chambers, continues to compress and deform thereby spreading impact energy over a larger surface area (37). Contemporary certified helmets offer large shells with complex contours that provide space for thicker and more efficient liners, with a tradeoff of increased weight (34, 38). Compared to 11 brain deaths recorded during the decade of 1995-2004, 25 brain deaths have already occurred within 2005-2013 (35). The increase in brain injury rate has raised concern about emerging helmet policies and technologies, but this time period also coincides with improved detection and medical care for concussion.

Brain Injury of Concussion

The Center for Disease Control and Prevention (CDC) reports that there are 1.7 million annual concussions documented, with estimates up around 3.8 million, and

greater than 170,000 of which are sports-related injuries among children under the age of 19 (39, 40). In the U.S., football has the highest frequency of concussions (1, 2), though this may be attributed to the greater number of participants (estimated at 3 million youth, 1.1 million high school, and 100,000 post-high school for a total 4.2 million in 2013) (35). The estimated injury incidence rate for football athletes is inconsistent as rates are reported per game (41), per impacts (42), and per athlete-exposures (1). Additionally, it is suggested that up to 53% of concussions can go unreported (43). A 2013 study combined these factors and estimated a football concussion incidence rate of 3.88 concussions per 1,000 head impacts (42). In addition to the physical toll of these injuries, the U.S. annual medical costs attributed to concussions are estimated at \$60 billion (44).

While the first clear recognition of concussion as an abnormal physiological state occurred around the 10th century (45), the first scientific-based definitions of sport concussion did not emerge until the beginning of the 21st century (46, 47), and the first international consensus was widely accepted in 2008 (48). As of 2013, it was agreed that the brain injury of concussion is a complex pathophysiological process affecting the brain, induced by biomechanical forces, typically resulting in a brief impairment of brain function, and usually caused by a direct blow to the head, face, or neck (11).

The primary cause of concussive injuries is the instant transfer of kinetic energy and inertial loading (40, 50) resulting in linear and rotational head accelerations inducing elevated brain pressure (51) and shear deformation of brain tissue (52), respectively. At the microscale, biomechanical forces cause axonal stretching and disrupt neuronal cell membranes (53) initiating a cascade of neurochemical and neurometabolic events (54). These events lead to ionic disturbances (55), decreased cerebral blood flow (56), and

metabolic dysfunction (57), and all of which occur without the loss of structural integrity of the involved tissue. As a result of no structural damage, but rather a forced metabolic imbalance, this condition is transient whereby literature supports a 7-10 day post-injury recovery period as demonstrated by clinical symptoms (12, 58).

No single biological marker that serves as a direct measure of concussion currently exists, but strong research efforts are focused on neural substrates, biomarkers, and brain imaging (59-61). Recent literature has reported that metabolic heterogeneity and molecular deficiencies exist for as long as 30 days (59, 62), and the imbalance leads to a condition propagated by the uncontrolled influx of calcium ions (Ca^{2+}) into the neuron (60). The toxic environment serves to not only decrease the overall efficiency of multiple neural networks, but also weakens the physical state of brain tissue which increases the athlete's risk of incurring a more severe, structural (tearing of axons) brain injury from repetitive impacts, called second impact syndrome (63). The cumulative effect of repeated brain injuries in athletes is not fully understood, but recent investigations suggest casual links to neurodegenerative disorders, such as chronic traumatic encephalopathy (CTE), resulting in features similar to Parkinson's and Alzheimer's diseases (64). As the body of knowledge for concussion continues to grow, the testing standards surrounding head injury in American football have also progressed.

Football Helmet Testing

Newly manufactured and reconditioned football helmets are certified to NOCSAE standards through testing designed to recreate linear biomechanical forces in American football and measure the subsequent acceleration experienced by the head. With the facemask removed, a helmeted head form equipped with a triaxial accelerometer

mounted at the center of mass of a biofidelic head form undergoes a series of guided free-falling impact conditions against a Modular Elastomer Programmer (MEP) polyurethane anvil pad (65) (Figure 1). The test protocol for new helmets entails multiple repetitive drop impacts at an interval of 75 ± 15 seconds across ambient and high temperatures at impact velocities of 3.46-5.46 m/sec at predefined helmet locations (65-67).

Among the numerous impulse-based criteria for head injury assessments developed to evaluate helmet impact attenuation performance, NOCSAE utilizes the Gadd Severity Index (SI). SI is calculated as an integral of the head form's linear acceleration (a) as measured across the duration of impact (t) ($SI = \int [a(t)]^{2.5} dt$) (65). The original performance requirement was set at 1500 SI in 1973 to decrease the occurrence of blunt head and spine injuries (68). The threshold remained unchanged until 1998, when it was lowered to 1200 SI because new helmets were easily passing (68). The current acceptance threshold for new helmets requires that no impact shall exceed 1200 SI, and 3.46 m/sec impacts must not exceed 300 SI (66).

Football helmet manufacturers and technologies focus on the reduction of concussion indirectly by aiming to minimize the SI value produced during a NOCASE drop test, as well as minimize a newly calculated qualitative concussion risk. In 2011, the Summation of Tests for the Analysis of Risk (STAR) formula was published whereby the peak acceleration from each NOCSAE drop test configuration is multiplied by a theoretical exposure-specific value (69, 70). All test values are summated to produce a STAR value which is used to evaluate and rank helmet performance. Critics of the STAR system claim the shortcomings of the still-evolving analysis are that the protocol tests only size Large helmets and the rating is calculated only using NCAA

biomechanical data (71). The widespread use of STAR ratings has grown rapidly, but NOCSAE certification still remains the accepted industry standard.

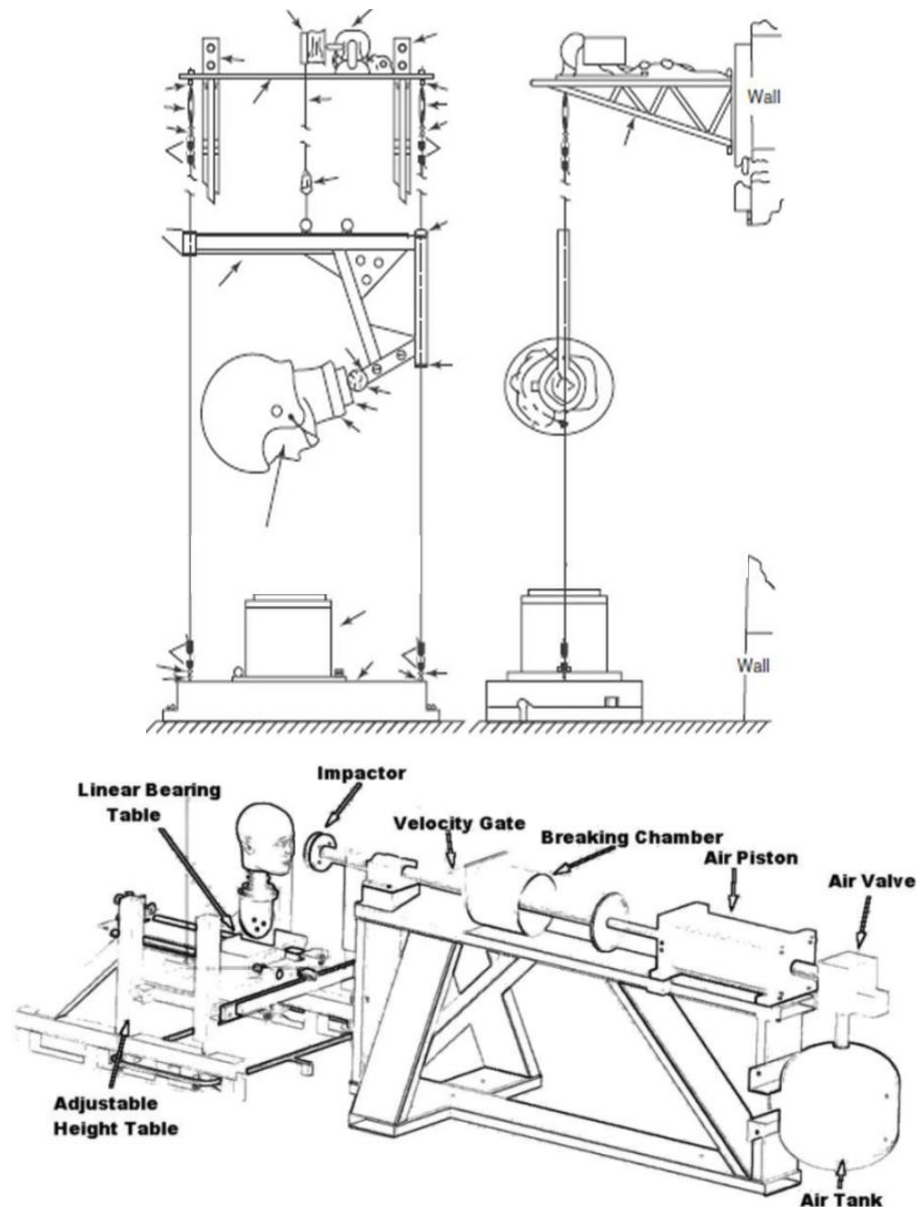


Figure 1. Schematic of NOCSAE (top) linear drop test setup (65) and (bottom) proposed pneumatic ram test used for helmet testing (66).

A new NOCSAE testing protocol purported to better simulate impact kinetics has been proposed (72), tested (26, 27, 33, 34) and recently approved (24). A linear impact setup (Figure 1) using a pneumatic ram is claimed to address concussion-causing forces by incorporating the rotational acceleration component of an on-field impact that is

absent with a linear drop test. The NOCSAE and STAR helmet assessments are expected to adopt a rotational performance protocol (73), which serve to stimulate new innovative helmet technologies (74).

Current Football Helmet Technologies

Examination of football helmets across manufacturers reveals systematic similarities and differences across select models. The various approaches in inner liners and their constituent polymeric materials across systems showcase efforts to reduce SI and STAR (29, 33, 34). Conversely, the outer shell of elite models is consistently a 3-4 mm thick, one-piece injection molded shell constructed of an engineered PC blend (37). A review of scientific literature in this area reveals a paucity of studies to support helmet models designed towards concussion reduction (8, 9). Furthermore, there is no evidence to support helmet efficacy related to the prevention of concussion (11-13).

For reasons unknown, helmet manufacturers rarely incorporate fundamental scientific investigation or the peer-review process into the product development cycle. Only a single manufacturer has provided procedural evidence of product development and efficacy specific to the impact attenuation of the inner liner component (see Chapter II) (75). The same inner liner component lacks comprehensive peer-reviewed data in its finalized off-the-shelf design, and therefore will be investigated in Chapter II. In addition, data is available for an ice hockey plaque-foam helmet surrogate, but testing involved geometric changes to 2.5 mm thick polyethylene outer shell component resulting in impact absorption variations of 4 to 35% (76). Further, full outer shells are reported to absorb between 10 to 40% of the total impact energy delivered, but characterization involved non-PC (77-80) or outdated helmet systems (81). While PC

has been the primary polymer in outer shell materials for over 60 years, the literature is devoid of studies on helmet-grade PC or outer shell components substantiating performance under end-use impact football conditions. Furthermore, PC shells are reused season after season without a comprehensive understanding about impact performance changes due to expected service life exposures.

Reconditioning and Recertification

Sport helmet systems are expected to deteriorate over time. The known reduction in the protective capacity of football helmet systems has led to an accepted restorative process throughout the industry. The reconditioning and recertification (RR) of football helmets is overseen by the National Athletic Equipment Reconditioners' Association (NAERA). NAERA formed in 1976 and a NOCSAE recertification standard for reconditioned helmets was introduced in 1977. Helmets were reportedly reconditioned prior to 1977, but under no recertification standard (82).

The RR process for American football helmets is purported to recover the performance and maintain its service life (see Chapter IV). In general, all helmet components and hardware are removed and replaced, except for the outer shell which is cleaned, sanded, and repainted. A review of the scientific literature reveals that processes mirroring reconditioning steps may serve to accelerate aging and degradation of outer shell materials (83). Furthermore, current reconditioning exposures to helmet outer shells lack scientific data that serve to validate their safe implementation or efficacy.

Upon helmet reassembly, a sample size of reconditioned helmet systems must pass NOCSAE recertification test standards before being approved for play (84). Therefore, a reconditioned helmet that exceeds the 1200 SI threshold indicates the impact

attenuation failure is attributed to aging or degradation of the PC outer shell. For helmets that pass, exposure of the PC shell to service life conditions still occurred, but is considered insignificant. Additionally, not every helmet is recertified; therefore, the true population of deteriorated helmets that exceed the threshold is unknown. Of the reconditioned helmet systems that are tested, the reported frequency of failure during helmet recertification was not found in the open literature.

Athletic equipment associations, legislative bodies, and helmet manufactures have instituted policies and recommendations towards helmet RR and service life (see Chapter IV). Notable variations in recommended reconditioning frequency, helmet shell warranty, and maximum shell service life exist across organizations and a review of the open literature does not substantiate each prescribed age limit (Table 1). Specifically, NAERA released a policy in 2011 that licensed members would no longer RR any football helmet 10 years of age or older (85). The RR of helmets is not mandatory, but is permissible on an annual basis. Since all non-shell components are replaced during RR, an annually reconditioned shell could qualify to endure a minimum 10 year lifespan. Data defining the degree and rate of change in drop test helmet performance across seasons, or within a single season, was not found in the open literature. As a result, the cumulative effect of service life conditions, including multiple reconditioning cycles as well as years of environmental and impact exposure on PC shells is not quantified. Therefore, the relationship between PC aging or degradation and the reduction in impact attenuation performance leading to a potential increased risk of head injury is unknown.

Table 1

Summary of football helmet policies and warranties across organizations

Organization	Reconditioning Frequency	Helmet Shell Warranty	Service Life Policy
NAERA	No time recommendation	-	Max Life: 10 years
NOCSAE	Every 2 years	-	No Max Life Policy (Severity Index: 1200+)
Texas State Legislation	Every 2 years, after 10 years of age	-	Max Life: 16 years
Riddell	Every 2 years	5 years	Max Life: 10 years with annual recertification
Schutt	Every 2 years	5 years	No Max Life Policy
Xenith	Every 2 years	5 years	Replaced no later than 10 years
Rawlings	Annually	5 years	Should be replaced after 10 years
Simpson-Ganassi	Every 2 years	Unstated	Should last well beyond 5-10 year lifespan

Service Life Exposures

Sport helmets are subjected seasonally to a myriad of environmental conditions under expected on-field use and storage. Throughout the lifespan of a helmet, environmental exposures include varying intensities of impact events, temperature ranges, ultraviolet (UV) light, oxygen, moisture, humidity, and chemicals (Figure 2). Such service life exposures alter the properties of constituent helmet materials, singularly and in combination, through a series of degradation mechanisms that serve to alter functionality of available energy dissipation mechanisms (83).

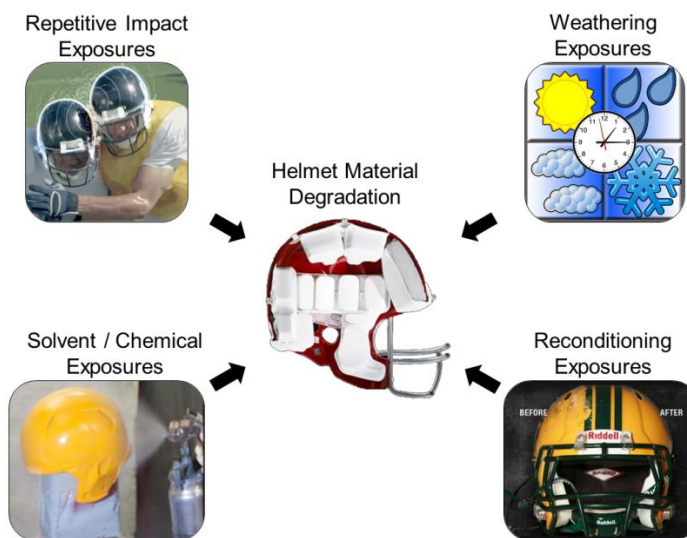


Figure 2. Schematic of the myriad of service life exposures exhibited on a football helmet outer shell under expected on-field use and storage.

The weathering of PC will activate degradation pathways such as photo-degradation, hydrolysis, and thermal-oxidation that induce material property changes (86) (see Chapter III). Exposure to UV light in air will produce nearly 40 degradation products that extend $\sim 40\ \mu\text{m}$ into the surface leading to reductions in tensile yield strength (86). Elevated temperatures will physically age PC causing structural morphology changes in free volume and crystallinity that macroscopically influence stress-strain behaviors (86). Humidity and moisture will induce plasticity and hydrolysis resulting in impact strength reduction (89). The cumulative effects of weathering conditions on the functional material properties and impact performance of helmet-grade PC blends is not reported, and therefore will be investigated in Chapter III.

The exposure of PC to soluble organic solvents will cause solvent-induced crystallization (SIC) and environmental stress cracking (ESC) at the microscopic and macroscopic levels, respectively (87-89) (see Chapter IV). Variations in the absorption of cleaners, adhesives, and paints will serve to expand the physical structure and reduce

the localized glass transition temperature. The failures of plastic materials in commercial use related to ESC have been estimated between 15-40% (90-92). However the degradative effects of expected solvent exposures specific to the helmet painting process have not been quantified, and therefore will be investigated in Chapter IV.

Helmet Impact Exposure

The first major attempt to study on-field helmet impact exposure was in the 1990s by the NFL. Film review of over 170 NFL in-game concussive impacts revealed 71% of cases involved impact by a player's helmet shell, with 62% of collisions being helmet-to-helmet (93, 94). Analysis found that concussion was calculated to occur with an average (i) impact velocity of 9.3 ± 1.9 m/sec, (ii) energy transfer to the head of 118 J (66-184 J ± 1 SD), (iii) peak linear acceleration of 98 ± 28 g, and (iv) strongly correlate with SI (474 ± 252) (93, 94). Since the early 2000s, an accelerometer array that integrates directly into existing football helmets, known as the head impact telemetry system (HITs), has recorded over 2,000,000 head impacts and over 100 concussions. The average linear acceleration associated with concussion recorded with HITs is reported to be 105 ± 27 g and not statistically different from the NFL analysis (69). The cumulative frequency of expected impact events to a single helmet measured by HITs is extensive, as the total number of impact exposures for an athlete has been reported to reach above 2200 in one season (95), with the front of the shell as the predominant location (69). An examination of this research emphasis reveals that comprehensive analysis of helmet performance has not extended beyond on-field biomechanical evaluations and into investigation of potential helmet material property degradation. The analyses are devoid of assessments of material property changes of helmet-grade polymers under expected on-field

environments. On the other hand, the impact testing of PC often utilize traditional testing regimes that simplify specimen shapes and commonly impose fracture events typically uncommon during on-field impacts (see Chapter III). Such testing appears to have minimal value towards improving the understanding of impact characteristics of helmet-grade materials under end-use conditions. As a result, a bridge of knowledge between helmet materials under traditional polymeric failure testing and accurate end-use impact conditions does not exist, and therefore will be investigated in Chapter V.

Research Overview

The purpose of this dissertation is to gain a greater scientific understanding of the changes in functional material properties and impact performance of an American football helmet outer shell material under expected environmental exposures. Helmet outer shells, comprised of engineered polycarbonate (PC) blends, are reused season after season without a comprehensive understanding about impact performance changes due to expected service life exposures. The research goals are to (i) quantify the chemical, physical, thermal, and mechanical degradation of an American football outer shell material under expected environmental conditions and (ii) develop a linear drop test impact protocol to employ expected on-field impact conditions to American football components and a plaque-foam (i.e., shell-liner) helmet surrogate. To determine how service life exposures affect impact performance, we aim to incorporate a step-wise progression of analysis to concurrently quantify and understand changes in material properties at the molecular, microscopic, and macroscopic (i.e., performance) levels. The grand challenge for this research is to identify polymer techniques and protocols that could (i) elucidate the rates and degrees of material degradation as a function treatment

duration and intensity and (ii) serve as a battery of diagnostic tools to analyze on-field outer shells throughout helmet life spans. The long-term mission for this research direction is to comprehensively understand the cumulative relationship between material aging and degradation, a decrease in impact performance, and the potential increased risk of head injury to the athlete throughout the lifecycle of the outer shell. The dissertation will aim to achieve five objectives described in the following chapters:

Objective 1 (Chapters II-V): develop a linear drop test impact protocol to employ expected on-field impact conditions to American football components and plaque foam (i.e., shell-liner) helmet surrogates

Objective 2 (Chapter II): define the linear impulse and compression behavior of a novel American football helmet liner component

Objective 3 (Chapter III): quantify the effects of accelerated weathering exposure on the functional material properties and impact performance of an American football outer shell material

Objective 4 (Chapter IV): (a) develop a method to accurately replicate solvent exposure during the reconditioning painting process and (b) quantify shifts in functional material properties and impact performance of an American football outer shell material

Objective 5 (Chapter V): quantify the effects of repetitive linear drop exposures and impact-induced stress-whitening on the functional material properties of an American football outer shell material

References

- 1 Rosenthal JA, Foraker RE, Collins CL, et al. National high school athlete concussion rates from 2005-2006 to 2011-2012. *Am J Sport Med* 2014, 42(7): 1710-1715
- 2 Marar M, McIlvain NM, Fields SK, et al. Epidemiology of concussions among united states high school athletes in 20 sports. *Am J Sports Med* 2012, 40: 747-755
- 3 Daneshvar DH, Nowinski CJ, McKee AC, et al. The Epidemiology of Sport-Related Concussion. *Clin J Sport Med* 2011 30: 1-17
- 4 Lincoln AE, Caswell SV, Almquist JL, et al. Trends in Concussion Incidence in High School Sports: A prospective 11-year study. *Am J Sport Med* 2011, 39: 958-963
- 5 Football Rules - National Federation of High School Associations. 2014. www.nfhs.org
- 6 Football Rules - National Collegiate Athletic Association. 2013. www.ncaa.org
- 7 Football Rules and Interpretation. National Football League. 2013. www.nfl.com
- 8 Benson BW, Hamilton GM, and Meeuwisse WH. Is protective equipment useful in preventing concussion? A systematic review of the literature. *Br J Sport Med* 2009, 43: i56-i67
- 9 Benson BW, McIntosh AS, Maddocks D, et al. What are the most effective risk-reduction strategies in sport concussion? *Br J Sports Med* 2013, 47: 321-326
- 10 Mueller FO. Fatalities from head and cervical spine injuries occurring in tackle football: 50 years' experience. *Clin J Sports Med* 1998, 17(1): 169–182

- 11 McCrory P, Meeuwisse WH, Aubry M, et al. Consensus statement on concussion in sport: the 4th International Conference on Concussion in Sport held in Zurich, November 2012. *Br J Sports Med* 2013, 47: 250-258
- 12 Broglio SP, Cantu RC, Gioia GA, et al. National Athletic Trainers' Association Position Statement: Management of Sport Concussion. *J Athl Training* 2014, 49(2): 245-265
- 13 Harmon KG, Drezner JA, Gammons M, et al. American Medical Society for Sports Medicine position statement: concussion in sport. *Br J Sports Med* 2013, 47: 15-26
- 14 Children's Sports Athletic Equipment Safety Act, HR1127, 112th Congress, 1st Session, 2011. www.govtrack.us
- 15 Children's Sports Athletic Equipment Safety Act, S601, 112th Congress, 1st Session, 2011. www.govtrack.us
- 16 Protecting Student Athletes from Concussions Act of 2011, HR469, 112th Congress, 1st Session. 2011. www.govtrack.us
- 17 Traumatic Brain Injury Legislation . *National Conference of State Legislatures*. [Accessed November 2014] www.ncsl.org.
- 18 Adrian Arrington v. Adrian Arrington. Case #: 1:11-cv-06356. Filed: September 12, 2011. Indiana Southern District Court.
- 19 National Football League Players' Concussion Injury Litigation. Case #: 2:2012md02323. Filed: January 31, 2012. Pennsylvania Eastern District Court
- 20 General Electric National Football League Head Health Challenge. 2012. NineSigma, Inc. www.ninesigma.com

- 21 Broglio SP, Surma T, and Ashton-Miller JA. High school and collegiate football athlete concussions: a biomechanical review. *Ann of Biomed Eng* 2012, 40(1): 37-46
- 22 Duma SM and Rowson S. Chapter 7: The Biomechanics of Concussion: 60 Years of Experimental Research. In: Slobounov SM and Sebastianielli (eds) *Concussions in Athletics: From Brain to Behavior*. 1st ed. New York: Springer, 2014, 115-137
- 23 Duma SM and Rowson S. Chapter 9: Biomechanical Studies of Impact and Helmet Protection. In: Slobounov SM and Sebastianielli (eds) *Concussions in Athletics: From Brain to Behavior*. 1st ed. New York: Springer, 2014, 167-178
- 24 Bollinger A. June 20 – NOCSAE Newsletter. National Operative Committee on Standards for Athletic Equipment, 2014
- 25 Post A, Hoshizaki TB, and Brien S. Chapter 33: Head Injuries, Measurement Criteria, and Helmet Design. In: Hong Y (ed) *Routledge Handbook of Ergonomics in Sport and Exercise*. 1st ed. New York: Routledge, 2014, 399-412
- 26 Post A, Oeur A, Hoshizaki B, et al. Differences in region-specific brain tissue stress and strain due to impact velocity for simulated American football impacts. *Proc IMechE Part P: J Sports Engineering and Technology* 2014, 228(4): 276-286
- 27 Post A, Oeur A, Hoshizaki B, et al. An examination of American football helmets using brain deformation metrics associated with concussion. *Materials & Design* 2013, 45: 653

- 28 Hoshizaki TB, Post A, Oeur RA, et al. Current and future concepts in helmet and sports injury prevention. *J Neurosurgery* 2014, 75(4): 5136-5148
- 29 Daneshvar DH, Baugh CM, Nowinski CJ, et al. Helmets and mouth guards: the role of personal equipment in preventing sports-related concussions. *Clin J Sports Med* 2011, 30: 145-163
- 30 Hoshizaki TB and Brien SE. (2004). The Science and Design of Head Protection in Sport. *J Neurosurgery* 2004, 55(4): 956-967
- 31 Hodgson, VR. National Operating Committee on Standards for Athletic Equipment football certification program. *Medicine & Science in Sports* 1975, 7(3): 225-231
- 32 Rowson S, Duma SM, Greenwald RM, et al. Can helmet design reduce the risk of concussion in football? *J Neurosurgery* 2014, 120: 919-922
- 33 Viano DC, Withnall C, and Halstead D. Impact Performance of Modern Football Helmets. *Ann of Biomed Eng* 2012, 40(1): 160-174
- 34 Viano DC and Halstead D. Change in size and impact performance of football helmets from the 1970s to 2010. *Ann of Biomed Eng* 2012, 40(1):175-84
- 35 Kucera KL, Klossner D, Colgate B, et al. Annual Survey of Football Injury Research. National Center for Catastrophic Sport Injury Research: UNC - Chapel Hill, 2013
- 36 Mueller FO and Cantu R. Annual Survey of Catastrophic Football Injuries. National Center for Catastrophic Sport Injury Research: UNC - Chapel Hill, 2012

- 37 Caswell SV, Gould TE, and Wiggins JS. Protective Helmets in Sports, Chapter 4
In *Materials in sports equipment*, Vol. 2; Subic A. Ed.; Woodhead: Camdrige,
2007: 87-126
- 38 Moss WC, King MJ, and Blackman EG. Towards reducing impact-induced brain
injury: lessons from a computational study of army and football helmet pads.
Computer Methods in Biomechanics and Biomedical Engineering 2014, 17(11):
1173-1184
- 39 Faul M, Xu L, Wald MM, et al. Traumatic Brain Injury in the United States:
Emergency Department Visits, Hospitalizations, and Deaths. Centers for Disease
Control and Prevention, 2010
- 40 Gilchrist J, Thomas KE, Xu L, et al. Nonfatal sports and recreation related
traumatic brain injuries among children and adolescents treated in emergency
departments in the United States, 2001–2009. *Morbidity Mortality Weekly Report*
2011, 60(39): 1337–1342
- 41 Pellman EJ, Powell JW, Viano DC, et al. Concussion in Professional Football:
Epidemiology Features of Game Injuries and Review of the Literature - Part 3. *J*
Neurosurgery 2004, 54(1): 81-96.
- 42 Rowson SR and Duma SM. Brain Injury Prediction: Assessing the combined
probability of concussion using linear and rotational head acceleration. *Ann of*
Biomed Eng 2013, 41(5): 873-8826
- 43 McCrea M, Hammeke T, Olsen G, et al. Unreported concussion in high school
football players: implications for prevention. *J Clinical Sports Medicine* 2004,
14: 3-17

- 44 Finkelstein EA, Corso PS, and Miller TR. The Incidence and Economic Burden of Injuries in the United States. New York (NY): Oxford University Press; 2006
- 45 McCrory PR and Berkovic SF. Concussion: The history of clinical and pathophysiological concepts and misconceptions. *Neurology* 2001, 57: 2283-2289
- 46 Aubry M, Dvorak J, Graf-Baumann T, et al. Summary and agreement statement of the first International Conference on Concussion in Sport, Vienna 2001. *Br J Sports Med* 2002, 36: 6-18
- 47 Guskiewicz KM, Bruce SL, Cantu RC, et al. National Athletic Trainers' Association Position Statement: Management of Sport-Related Concussion. *J Athl Training* 2004, 39(3): 280-297
- 48 McCrory, P, et al. Consensus Statement on Concussion in Sport 3rd International Conference on Concussion in Sport Held in Zurich, November 2008. *Clin J Sport Med* 2009, 19(3): 185-200
- 49 Shaw, NA. The neurophysiology of concussion. *Neurobiology* 67, 2002, 281-344
- 50 Meaney, DF and Smith, DH. Biomechanics of Concussion. *Clin J Sport Med* 2011, 30: 19-31
- 51 Thibault, LE, et al. Biomechanical Aspects of a Fluid Percussion Model of Brain Injury. *J Neurotrauma* 1992, 9(4): 311-323
- 52 Donnelly, BR and Medige, J. Shear Properties of Human Brain Tissue. *J Biomechanical Engineering* 1997, 119: 423-432
- 53 Farkas, O, Lifshitz, J and Povlishock, JT. Mechanoporation Induced by Diffuse Traumatic Brain Injury: An Irreversible or reversible response to injury? *J Neuroscience* 2006, 26(12): 3130-3140

- 54 Giza, CC and Hovda, DA. The Neurometabolic Cascade of Concussion. *J Athl Training* 2001, 36(3): 228-235
- 55 Yoshino, A, et al. Dynamic changes in local cerebral glucose utilization following cerebral concussion in rats: evidence of a hyper- and subsequent hypometabolic state. *Brain Research* 1991, 561: 106-119
- 56 Martin, NA, Patwardhan, RV and Alexander, MJ. Characterization of cerebral hemodynamic phases following severe head trauma: hypoperfusion, hyperemia, and vasospasm. *J Neurosurgery* 1997, 87(1): 9-19
- 57 Signoretti, S, et al. Biochemical and neurochemical sequelae following mild traumatic brain injury: summary of experimental data and clinical implications. *Neurosurgery Focus* 2010, 29(5): 1-12
- 58 McCrea, M, et al. Acute Effects and Recovery Time Following Concussion in Collegiate Football Players. *JAMA* 2003, 290(19): 2556-2563
- 59 Signoretti S, Tavazzi B, Lazzarino, et al. Chapter 6: The Revelance of Assessing Cerebral Metabolic Recovery for a Safe Return to Play Following Concussion. In: Slobounov SM and Sebastianielli (eds) *Concussions in Athletics: From Brain to Behavior*. 1st ed. New York: Springer, 2014, 89-112
- 60 Hovda DA, Giza CC, Bergsneider M, et al. Chapter 11: Metabolic Dysfunction Following Traumatic Brain Injury. In: Slobounov SM and Sebastianielli (eds) *Concussions in Athletics: From Brain to Behavior*. 1st ed. New York: Springer, 2014, 205-215

- 61 Papa L. Chapter 13: Biomarkers for Concussion. In: Slobounov SM and Sebastianielli (eds) *Concussions in Athletics: From Brain to Behavior*. 1st ed. New York: Springer, 2014, 235-248
- 62 Vagnozzi R, Signoretti S, Cristofore L, et al. Assessment of metabolic brain damage and recovery following mild traumatic brain injury: a multicentre, proton magnetic resonance spectroscopic study in concussed patients. *Brain* 2010, 133: 3232-3242
- 63 Bey T and Ostick B. Second Impact Syndrome. *Western Journal of Emergency Medicine* 2009, 10(1): 6-10
- 64 McKee AC, Cantu RC, Nowinski CJ, et al. Chronic Traumatic Encephalopathy in Athletes: Progressive Tauopathy After Repetitive Head Injury. *J Neuropathology & Experimental Neurology* 2009, 68(7): 709-735
- 65 NOCSAE ND001-13m14b. Standard test method and equipment used in evaluating the performance characteristics of protective headgear/equipment. National Operative Committee on Standards for Athletic Equipment 2013
- 66 NOCSAE ND002-13m13. Standard performance specification for newly manufactured football helmets. National Operative Committee on Standards for Athletic Equipment 2013
- 67 ASTM F1446-13. Standard test methods for equipment and procedures used in evaluating the performance characteristics of protective headgear. American Society for Testing and Materials International 2013
- 68 Schwarz Al. As Injuries Rise, Scant Oversight of Helmet Safety. *New York Times*. Associated Press, 20 October 2010

- 69 Rowson S and Duma SM. Development of the STAR evaluation system for football helmets: integrating player head impact exposure and risk of concussion. *Ann of Biomed Eng* 2011, 39(8): 2130–2140
- 70 Funk JR, Rowson S, Daniel RW, et al. Validation of concussion risk curves for collegiate football players derived from hits data. *Ann of Biomed Eng* 2012, 40(1): 79–89
- 71 Bollinger A. May 27 – NOCSAE Newsletter. National Operative Committee on Standards for Athletic Equipment, 2014
- 72 NOCSAE ND081-14. Standard pneumatic ram test method and equipment used in evaluating the performance characteristics of protective headgear and face guards. National Operative Committee on Standards for Athletic Equipment 2014
- 73 Rowson S, Duma M, Beckwith JG, et al. Rotational head kinematics in football impacts: an injury risk function for concussion. *Ann of Biomed Eng* 2012, 40(1): 1–13
- 74 Johnston JM, Ning H, Kim JE, et al. Simulation, fabrication and impact testing of a novel football helmet padding system that decreases rotational acceleration. *Sports Engineering* 2015, 18: 11-20
- 75 Lamb L and Hoshizaki TB. Deformation mechanisms and impact attenuation characteristics of thin-walled collapsible air chambers used in head protection. *Proc. IMechE, Part H: J. Engineering in Medicine* 2009, 223: 1021-1031
- 76 Spyrou E, Pearsall DJ and Hoshizaki TB. Effect of local shell geometry and material properties on impact attenuation of ice hockey helmets. *Sports Engineering* 2000, 3: 25-35

- 77 Gale A and Mills NJ. Effect of polystyrene foam liner density on motorcycle helmet shock absorption. *Plastics and Rubber Processing and Applications* 1985, 5: 101-108
- 78 Gilchrist A and Mills NJ. Impact deformation of ABS and GRP motorcycle helmet shells. *Plastics and Rubber Processing and Applications* 1994, 21: 141-150
- 79 Denning A and Mills NJ. The deterioration of thermoplastic motorcycle helmet shells after outdoor exposure. *Plastics Rubber Processing and Applications* 1992, 18: 67-77
- 80 Ragagnin F. Analysis of the structural behavior of ski helmets during impact and penetration tests. 2013. Masters Thesis, University of Padova, Italy
- 81 Vetter L, Vanderby R, and Broutman LJ. Influence of materials and structure on performance of a football helmet. *Polym Eng Sci* 1987, 27(15): 1113-1120
- 82 Tue SA. Helmet reconditioning: How to do it right. USA Football. 27 Nov 2012
- 83 Wypych G. Handbook of Material Weathering, 4th ed.; ChemTec: Toronto, 2008
- 84 NOCSAE ND004-11m14. Standard performance specification for recertified football helmets. National Operative Committee on Standards for Athletic Equipment 2014
- 85 Fisher E. 10-year helmet reconditioning policy – Press Release. National Athletic Equipment Reconditioners Association, 2011
- 86 Legrand, DG and Bendler, JT. Handbook of Polycarbonate Science and Technology. New York : Marcel Dekker, 2000

- 87 Mercier JP, Groeninckx G, and Lesne M. Some aspects of vapor-induced crystallization of polycarbonate of bisphenol A. *J Polymer Science Part C: Polymer Symposia* 1967, 16(4): 2059-2067
- 88 Desai AB and Wilkes GL. Solvent-induced crystallization of polyethylene terephthalate. *J Polymer Science: Polymer Symposia* 1974, 46(1): 291-319
- 89 Robeson, LM. Environmental stress cracking: A review. *Polym Eng Sci* 2013, 53(3): 453-467
- 90 Arnold JC. Environmental stress-crack initiation in glassy polymers. *Trends in Polymer Science* 1996, 4: 403-408
- 91 Wright DC. Environmental stress cracking of plastics. RAPRA Publishing, United Kingdom, 1996.
- 92 Jansen JA. Environmental stress cracking – the plastic killer. *Advances and Material Processes* 2004, 162(6): 50-53
- 93 Pellman EJ, Viano DC, Casson IR, et al. Concussion in Professional Football: Reconstruction of game impacts and injuries – Part 1. *J Neurosurgery* 2003, 53(4): 799-814
- 94 Pellman EJ, Viano DC, Tucker AM, et al. Concussion in Professional Football: Location and Direction of Helmet Impacts – Part 2. *J Neurosurgery* 2003, 53(4): 1328-1341
- 95 Broglio SP, Eckner JT, Martini D, et al. Cumulative Head Impact Burden in High School Football. *J Neurotrauma* 2011, 28: 2069-2078

CHAPTER II

INVESTIGATION OF LINEAR IMPACT ENERGY MANAGEMENT AND
PRODUCT CLAIMS OF A NOVEL AMERICAN FOOTBALL
HELMET LINER COMPONENT

Abstract

The pursuit to abate sport-related concussion necessitates thorough evaluation of protective technologies and product claims. Therefore, the purpose of this investigation was to: (I) define the linear impulse and compression behavior of the Aware-Flow[®] shock absorber (the primary energy managing component of Xenith X1[™] football helmet), (II) characterize resultant force-time curves utilizing compressive loading behavior of foam materials, and (III) verify and define published findings and product claims. Absorbers (N=24) from three adult X1[™] football helmets were impacted at predefined velocities of 1.3, 2.3, 3.0, 4.0, and 4.7 m/sec. Linear impulsive forces were ideally managed up to 3.0 m/sec (25.4 J). The foam-filled pad improved impact energy attenuation and increased velocity-specific durability. The leptokurtic region of the 4.0 and 4.7 m/sec impulse curves substantiated a third phase, defined as densification, as demonstrated by the maximum compression height approaching 90%. The adoption of elastic-plastic foam terminology was recommended based upon examination of the shock absorber design and resultant phased force-time curves. Results validated published findings on the prototype thin-walled collapsible air-filled chamber component and substantiated velocity-specific support for Aware-Flow[®] shock absorber product claims.

Introduction

The high prevalence of the brain injury of concussion to participants across all sports (1, 2) has raised public concerns regarding the prevention strategies, diagnostic

techniques, long-term effects and management of the injury (3). The rate of concussive injuries specific to helmeted sports such as American football has provoked requests at the Federal level for investigations into the safety standards (4) and the performance claims of protective head gear (5). The increase in attention to standards for helmets and the concussion prevention for youth participants is further showcased by extensive legislation at the state (6) and national-level (7-9).

Football helmets were initially developed to prevent catastrophic head injuries (10) and modern helmets that meet current standards have evidence to adequately provide such protection (11). However, as the understanding of the brain injury concussion began to materialize early in the 21st century, it became apparent there is no evidence to indicate that the same helmets effectively reduce or prevent concussion (12-14). As greater proficiency is gained towards the causal mechanisms of the concussive injury, it is imperative to concomitantly gain understanding of the energy dissipation mechanisms provided by protective head gear. For reasons unknown, a culture among helmet manufacturers has been fostered that rarely incorporates fundamental scientific investigation nor the peer review scientific process into the product development cycle. Thus, manufacturers, materials scientists, and sports engineers must employ the rigor of scientific investigation and the peer review process throughout the development of new technologies. In lieu of manufacturers substantiating product performance with a priori scientific evidence, pursuit to abate sport-related concussion necessitates the retrospective evaluation of impact energy management characteristics of protective head gear.

Certified for use in 2007 and released for sale in 2009 (15), the Xenith[®] X1[™] football helmet was developed in collaboration with the Neurotrauma Impact Laboratory

at the University of Ottawa. Unique to marketplace counterparts, the research associated with the initial development and optimization of the X1™ technology was published in the peer reviewed scientific literature (16-19). Multiple patents have also been awarded to the engineered components within the X1™ football helmet and Xenith® has made product catalogs (20, 21) and quality assurance reports (15) openly available. Due to the collective availability of this information, it is feasible to conduct studies to scientifically verify published findings, and further extend investigation into product claims.

Initial published findings (16) described the variation in impact force attenuation of vented and non-vented rigid-walled collapsible air chambers. Further research of vented chambers (17) reported on the improved impact energy management of multi-impact air chamber technology over conventional vinyl nitrile foam used as ice hockey helmet materials. Development continued with the validation of a new methodology (18) that allowed for further investigation of the air venting system and the identification of separate mechanisms that influence impact energy damping. The latest published findings (19) examined the effect of air vent diameter on peak force attenuation across multiple impact trials and increasing impact velocities. The resultant force-time curves were further characterized into regions related to air chamber compression behavior; however, these descriptions were established from original work characterizing permanent deformation of the investigated materials (20).

The Xenith® X1™ football helmet inner liner houses multiple Aware-Flow® shock absorbers (Figure 3) (20, 21). Each shock absorber consists of a resilient foam-filled enclosed pad connected to a thin-walled collapsible air chamber (TWC) (Figure 4) (23). The patent literature (24, 25) claims that impact energy management for the TWC

occurs via a phased resistance approach (claim 1). Initial energy damping is attributed to side wall loading of the TWC (24, 25), primary damping is achieved through a fluid venting mechanism (23-25), and the final damping is provided via the compressibility of the constituent material (26). Collectively, the resistive mechanisms are claimed (24-26) to attenuate impact energy via a flattened, trapezoidal-shaped force-time curve (claim 2). Specifically, the TWC fluid venting mechanism is claimed (24-26) to afford adaptability and thus optimally manage energy over a range of undefined impact energy levels (claim 3). The TWC's compressive ability is claimed (24-26) to allow a maximum "ride-down" to over 90% of its original height (claim 4). Furthermore, patent literature (25) specific to the addition of the foam-filled pad, claims improved impact energy attenuation (claim 5) and increased durability across expected service-life cycling of the system (claim 6).



Figure 3. Xenith® X1™ football helmet with revealed liner system and single Aware-Flow® shock absorber.

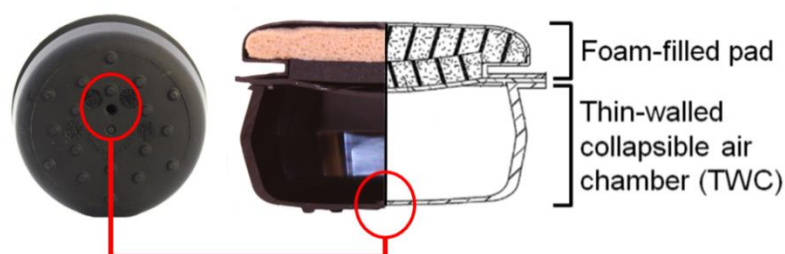


Figure 4. Schematic of Xenith® X1™ Aware-Flow® shock absorber and corresponding air vent location (23).

The study herein investigated the mechanisms of impact energy management provided by the Aware-Flow[®] shock absorber (the primary impact energy management component of the off-the-shelf Xenith[®] X1[™] football helmet). The analysis of the shock absorber was compared to the initial linear impact attenuation research (18, 19) conducted on the prototype TWC component during development (no foam-filled pad) and further evaluated against the well-established viscoelastic compressive behavior of foam materials. Additionally, this study served to verify and define patent literature claims for the Aware-Flow[®] shock absorber. While the published findings (18, 19) provided initial verification of patent claims 1-3 and a preliminary discussion of patent claim 6 for the TWC prototype, this study addressed the gap in the scientific literature regarding the unverified, non-peer reviewed product claims specific to the addition of the foam-filled pad. Therefore, the three-fold purpose of this investigation was to: (I) define the linear impulse and compression behavior of the Aware-Flow[®] shock absorber, (II) characterize resultant force-time curves utilizing compressive loading behavior of foam materials, and (III) verify and define published findings and product claims. In summary, these relationships are between impact velocity and peak force, impulse curve shape (published findings, claims 1-3), and compression height (claim 4); effect of the foam-filled pad on peak force across increasing impact velocities (claim 5); velocity-specific effect of repetitive impacts on peak force (claim 6).

Experimental

Materials

Aware-Flow[®] shock absorbers from three off-the-shelf adult Xenith[®] X1[™] (Xenith, LLC., Boston, MA) football helmets were characterized by location within the

helmet. Each shock absorber contained a thin-walled collapsible air chamber (TWC) outfitted with an enclosed foam-filled pad. Further observation across specific helmet locations indicated that the liner was comprised of two different absorbers. Pilot testing and literature indicated the TWC component was made of thermoplastic polyurethane (TPU) (16-19, 23, 26) with one of two material hardness values (16-19). As a result, absorbers composed of harder TPU material (i.e., the four front boss pads) were not used in the study. Air vent size ($\bar{x} = 2.3 \text{ mm} \pm 0.4$) and absorber height ($\bar{x} = 37.9 \text{ mm} \pm 0.4$) of soft TPU TWC absorbers (N=24) were measured to ensure production batch consistency (Figure 4). The studied absorbers were randomly assigned into two groups: the foam-filled top pad removed from the air chamber (SA_{No Pad}) and kept intact (SA_{Pad}).

Equipment

The drop test system and setup described in published findings (18, 19), a Cadex monorail outfitted with a headform mass of 5.06 kg, was approximated using an instrumented drop tower system (Dynatup 9250HV, Instron, Norwood, MA) (Figure 5). The drop mass assembly of 5.64 kg contained a 88 kN (20 000 lb) load cell tup and a customized 63.5 mm (2.5 in) flat cylindrical steel drop dart to eliminate shear forces during impact. Absorbers were impacted under ambient conditions against a flat, hardened steel anvil and impact velocities were confirmed using an optical velocity flag. First impact trials for each SA_{Pad} were captured with a Phantom v5.1 (Vision Research, Inc., Wayne, NJ) color high speed video camera at 2100 frames per second.

Procedure

Shock absorbers were impacted in accordance with a balanced, post-test only control group experimental design. Of the 24 total off-the-shelf absorbers, 18 were

randomly selected and split into two groups, SA_{No Pad} and SA_{Pad}. Within each group of nine, three groups of absorbers each of which underwent 15 repetitive impacts (28) at an interval of 75 ± 15 seconds (29) at a predefined velocity (19) of either 1.3 m/sec (4.8 J), 3.0 m/sec (25.4 J), or 4.0 m/sec (45.1 J). Thus, a total of nine (3 absorbers per velocity X 3 impact velocities) were repetitively impacted within each of the SA_{No Pad} and SA_{Pad} groups. The six remaining absorbers were placed into the SA_{Pad} group and underwent a single impact trial at a predefined velocity of either 2.3 m/sec (14.9 J) or 4.7 m/sec (62.3 J). Thus, a total of fifteen (3 absorbers per velocity X 5 impact velocities) underwent a single impact within the SA_{Pad} group. All absorbers were randomly assigned and a total of 276 impact trials were conducted. An order effect was not expected and therefore, the order of treatments was not randomized.

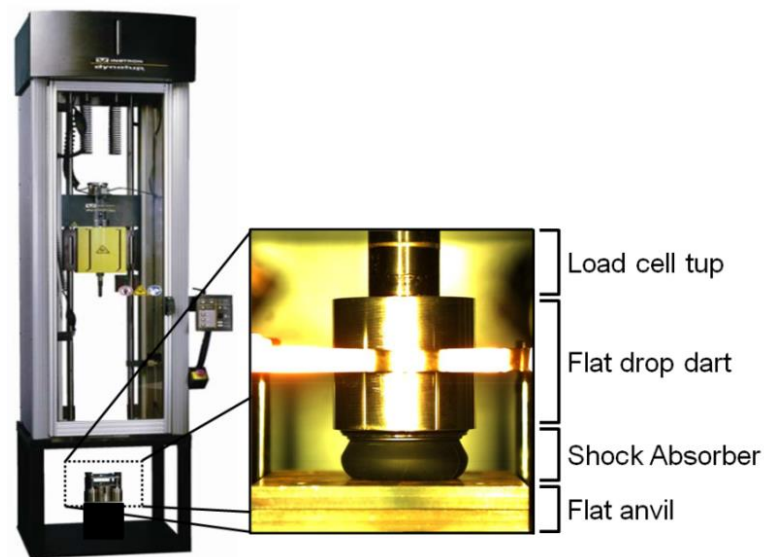


Figure 5. Instron® Dynatup® 9250HV instrumented drop tower system (27).

Data Acquisition and Analysis

Force data were collected via Impulse Data software (v. 3.2.30, Instron, Norwood, MA). Compressed SA_{Pad} heights were determined using Phantom 649 Camera software (v. 9.0.649, Vision Research, Inc., Wayne, NJ) and percent compression (%_{COMP}) was

calculated via: $\%_{COMP} = (H_{INITIAL} - H_{FINAL}) / H_{INITIAL}$, where $H_{INITIAL}$ was the non-impacted, uncompressed SA_{Pad} height ($\bar{x} = 37.9$ mm) and H_{FINAL} was the impacted, compressed SA_{Pad} height.

The voltage signal output from the force sensor produced major oscillations or “signal ringing” during impact testing at lower velocities. As a result, force data at 1.3 m/sec required a Savitzky-Golay (SG) smoothing filter at 1501 points of window under a polynomial order of 2, with no boundary conditions. Selection of a SG filter was utilized because features of the data such as peak height and width are better preserved. Signal ringing was also observed at higher velocities (e.g., $SA_{No Pad}$ at 3.0 m/sec), but minor oscillations were produced and thus smoothing was not performed.

Impulse curve shape was not consistent across escalating impact velocities. At higher velocities, impacts produced a bimodal curve. As a result, the initial maximum was defined as the peak collapse force (F_{COLL}) and the secondary maximum was defined as the peak compression force (F_{COMP}). At lower velocities, a unimodal curve was produced and the singular maximum represented both F_{COLL} and F_{COMP} (Figure 6). The assignment of both F_{COLL} and F_{COMP} at lower velocities was performed to allow for a balanced statistical analysis when examining differences between SA_{Pad} and $SA_{No Pad}$ groups across impact velocities. The F_{COLL} and F_{COMP} values were entered into the Statistical Package for Social Sciences software (SPSS, v. 18, IBM Corporation, Sonoma, NY). For each of the impact velocity intervals of 1.3, 3.0, and 4.0 m/sec, a separate 2 (condition: SA_{Pad} , $SA_{No Pad}$) X 15 (trials: repetitive impacts 1-15) mixed model repeated measure analysis of variance was performed. The alpha level was set a priori at $\alpha = .05$. The effect size was calculated using Cohen’s f .

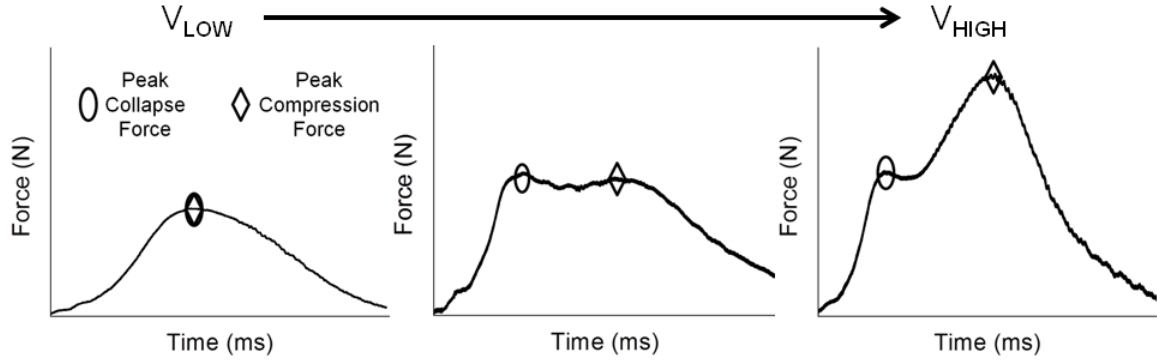


Figure 6. Impulse curve progression for increasing impact velocities.

Results

Published Findings and Claims 1-3

For each impact velocity, the SA_{Pad} mean F_{COMP} were: 1.3 m/sec (735 N \pm 31), 2.3 m/sec (930 N \pm 10), 3.0 m/sec (1638 N \pm 12), 4.0 m/sec (9225 N \pm 298), and 4.7 m/sec (15 849 N \pm 401). The $SA_{No Pad}$ mean F_{COMP} were: 1.3 m/sec (840 N \pm 10), 3.0 m/sec (1908 N \pm 123), and 4.0 m/sec (13 514 N \pm 58). The SA_{Pad} and $SA_{No Pad}$ time-averaged impulse curve shapes across increasing impact velocities are plotted in Figure 7.

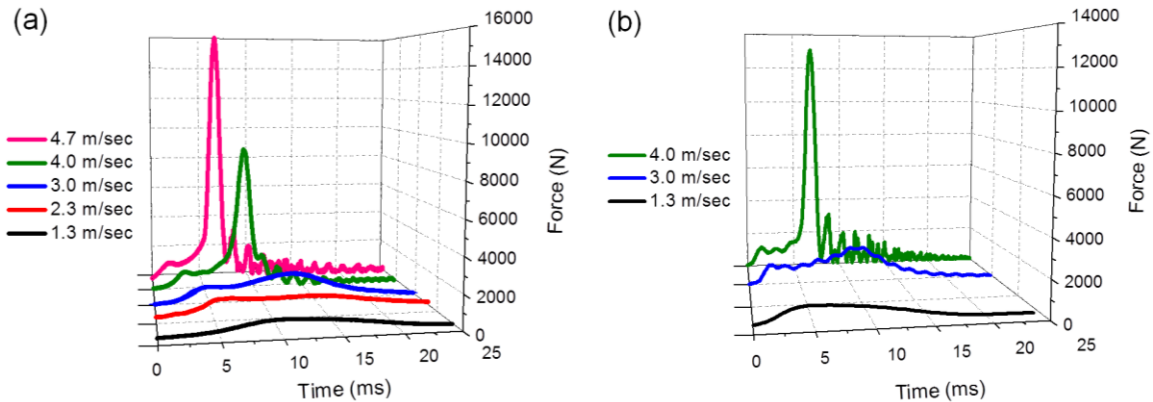


Figure 7. (a) SA_{Pad} and (b) $SA_{No Pad}$ time-averaged impulse curves of first impact trials.

The SA_{Pad} and $SA_{No Pad}$ impact trials at 1.3 m/sec resulted in an approximately ‘bell-shaped’ impulse curve (Figure 8). The SA_{Pad} trials at 2.3 m/sec exhibited a trapezoidal force-time curve behavior. The SA_{Pad} and $SA_{No Pad}$ impact trials at 3.0 m/sec exhibited an approximate trapezoidal impulse curve shape (Note: Change in scale of

force axis in Figures 7 and 8). The 4.0 and 4.7 m/sec SA_{Pad} trials exhibited impulse curves characterized by an initial trapezoidal region followed by a leptokurtic region.

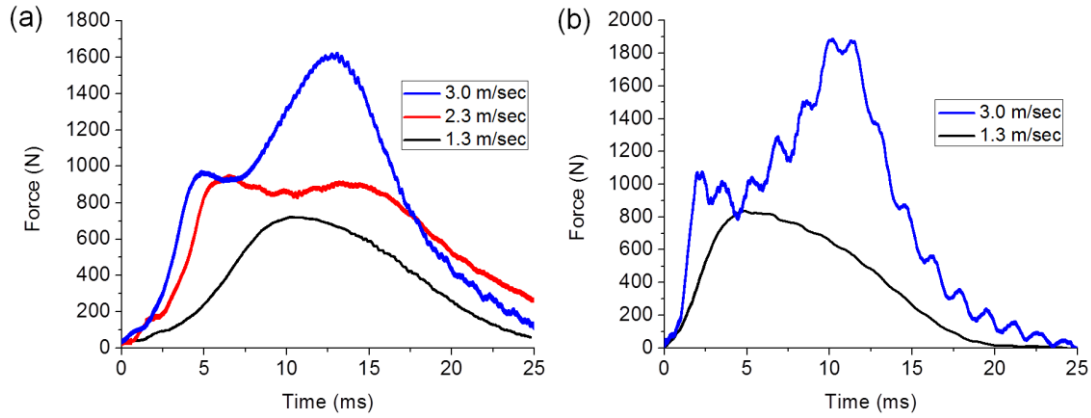


Figure 8. (a) SA_{Pad} and (b) SA_{No Pad} time-averaged impulse curves for 1.3 – 3.0 m/sec.

Claim 4

For each impact velocity (Figure 9), the maximum compression height and percent compression results were: 1.3 m/sec (21.78 mm \pm 0.33; 42.6%), 2.3 m/sec (13.04 mm \pm 0.60; 65.6%), 3.0 m/sec (7.70 mm \pm 0.35; 76.8%), 4.0 m/sec (5.01 mm \pm 0.36; 86.8%), and 4.7 m/sec (4.04 mm \pm 0.05; 89.4%).

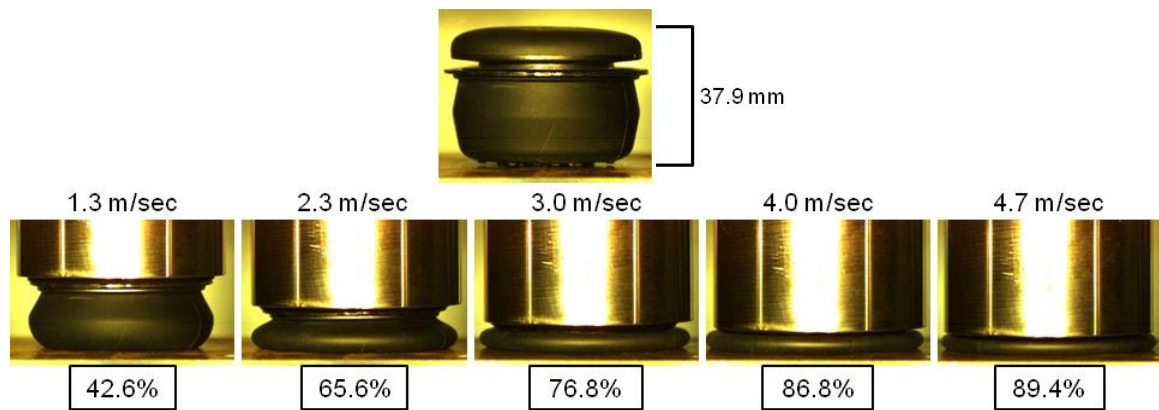


Figure 9. Maximum SA_{Pad} compression behavior and percent compression across increasing impact velocities.

Claims 5 and 6

For mean F_{COLL} , no statistically significant between, within or interaction effects ($P=0.58, 0.222, 0.147$, respectively) were observed at 1.3 m/sec. However, between,

within and interaction effects were present across trials for 3.0 m/sec ($F_{1,4}=8.21$, $P=0.046$, $f=1.42$, $F_{14,56}=41.35$, $P=0.001$, $f=3.18$, and $F_{14,56}=2.76$, $P=0.004$, $f=0.83$, respectively). 4.0 m/sec elicited no between effect ($P=0.478$), but did provide within ($F_{14,56}=87.98$, $P=0.001$, $f=4.90$) and interaction ($F_{14,56}=2.41$, $P=0.010$, $f=0.78$) effects.

For mean F_{COMP} , no statistically significant between, within, or interaction effects ($P=0.062$, 0.059 , 0.058 , respectively) were observed at 1.3 m/sec. Again, between ($F_{1,4}=70.51$, $P=0.001$, $f=4.36$), within ($F_{14,56}=32.13$, $P=0.001$, $f=2.84$) and interaction ($F_{14,56}=17.25$, $P=0.001$, $f=2.06$) effects were found for 3.0 m/sec. 4.0 m/sec elicited both a between ($F_{1,4}=213.43$, $P=0.001$, $f=7.00$) and within ($F_{14,56}=18.01$, $P=0.001$, $f=2.13$) effect, but no interaction ($P=0.612$). Figure 10 shows the progression of mean F_{COLL} and F_{COMP} across 15 repetitive trials for SA_{Pad} and $SA_{No Pad}$ at 3.0 and 4.0 m/sec.

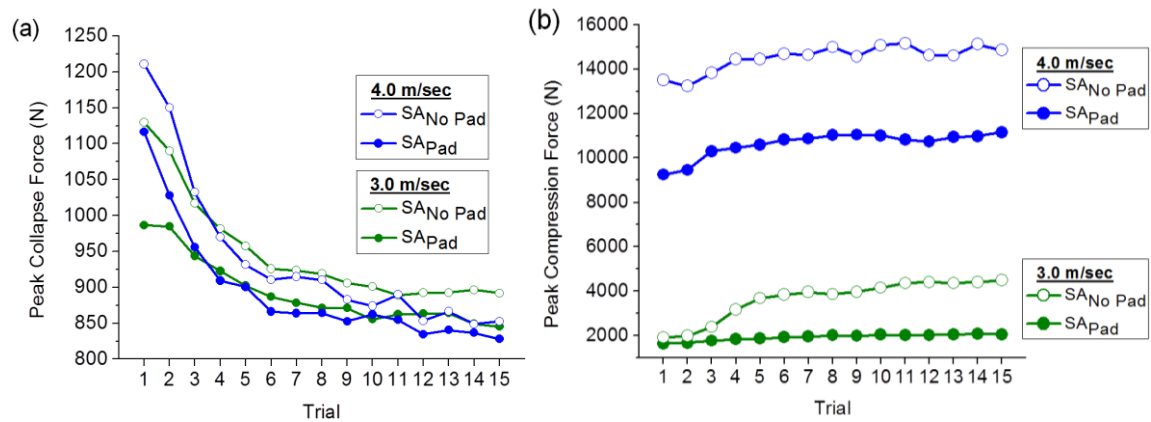


Figure 10. (a) Mean peak collapse forces and (b) mean peak compression forces for repetitive impact testing of SA_{Pad} and $SA_{No Pad}$ at 3.0 and 4.0 m/sec.

Across the 15 repetitive impacts delivered to a single absorber, the progression of the characteristic shape of impulse curves remained consistent. The shape of the peak collapse maximum and trapezoidal plateau was inversely changing in force compared to the peak compression maximum at 3.0 m/sec for SA_{Pad} and $SA_{No Pad}$ absorbers (Figure 11).

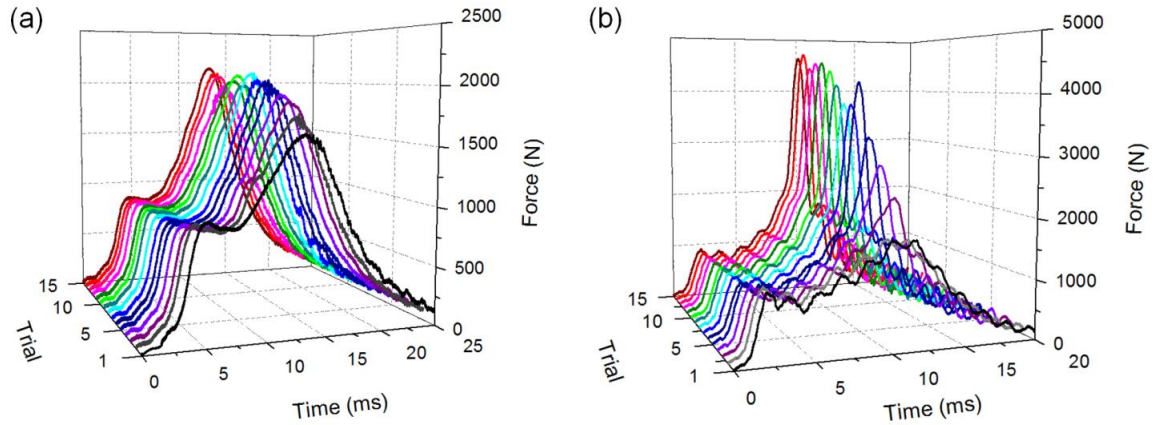


Figure 11. (a) SApad and (b) SANo Pad impulse curve shape progression at 3.0 m/sec for a single absorber across 15 repetitive trials.

Discussion

Published Findings

Published findings (18, 19) examined the peak force attenuation of the prototype TWC component across increasing impact velocities. A direct comparison between reported mean peak forces and our results of mean F_{COLL} and F_{COMP} values are listed in Table 2. While the study herein replicated the selected impact velocities, the peak forces and force-time curves differ because of potential limitations: (1) selection of the manufactured shock absorber compared to the TWC air chamber prototype where air vent size measured ($\bar{x} = 2.3 \text{ mm} \pm 0.4$), (2) use of an instrumented Dynatup drop tower equipped with a flat drop dart compared to a Cadex monorail drop rig outfitted with a curved headform, (3) variation in linear impact energy due to a 0.62 kg difference in our drop dart mass, and (4) the reporting of filtered and unfiltered raw signal output within the same data collection. Examination of both the progression of mean F_{COLL} and F_{COMP} values (Table 2) and impulse curve shapes (Figures 7 and 8) collectively validated and further defined published findings (18, 19). As a result, our instrumented drop tower setup is substantiated to further investigate linear impact attenuation performance.

Table 2

Comparison of the prototype TWC component mean peak force values reported with air vent diameters of 2 and 3 mm (19) to mean F_{COLL} and F_{COMP} results of the off-the-shelf Xenith® XI™ shock absorber (air vent diameter: $\bar{x} = 2.3$ mm)

Impact Velocity (m/sec)	Impact Energy (J)	Vent Diameter (mm)	Pad Condition (SA _{Pad} /SA _{No Pad})	Mean Peak Force (N)
1.3	4.2	2	-	720 ±12 ¹
		3	-	689 ±24 ¹
2.3	13.3	2	-	2078 ±548 ¹
		3	-	3781 ±1105 ¹
3.0	22.6	2	-	11 272 ±741 ¹
		3	-	13 436 ±704 ¹
1.3	4.2	2	-	976 ±57 ²
		3	-	936 ±23 ²
2.3	13.3	2	-	1330 ±37 ²
		3	-	1225 ±62 ²
3.0	22.6	2	-	8453 ±1691 ²
		3	-	8700 ±1398 ²
1.3	4.8	-	SA _{Pad}	735 ±31 ^{3,4}
		-	SA _{No Pad}	840 ±10 ^{3,4}
2.3	14.9	-	SA _{Pad}	930 ±10 ³
		-	SA _{Pad}	987 ±15 ⁴
3.0	25.4	-	SA _{Pad}	1638 ±12 ⁴
		-	SA _{No Pad}	1908 ±123 ⁴
4.0	45.1	-	SA _{Pad}	9225 ±298 ⁴
		-	SA _{No Pad}	13 514 ±58 ⁴
4.7	62.3	-	SA _{Pad}	15 849 ±401 ⁴

1 TPU 90A; 2 TPU 45D; 3 F_{COMP} ; 4 F_{COLL}

Claim 1: Phased Resistance

The claim of a phased resistance approach to impact energy management is described by the patent literature (24, 25) to be represented as an initial steep incline followed by a flat portion in the force-time curve. Published findings (19) provided support by dividing prototype TWC impulse curves into three independent regions. Our results defined a velocity-specific phased resistance to linear impact energy management.

Only impulse curves of 2.3 m/sec (14.9 J) and greater exhibited an initial rise to a maximum (phase I) followed by a flattened, plateau region (phase II). For 3.0 m/sec (25.4 J) and greater, a second incline and maximum emerged (phase III) (Figure 12).

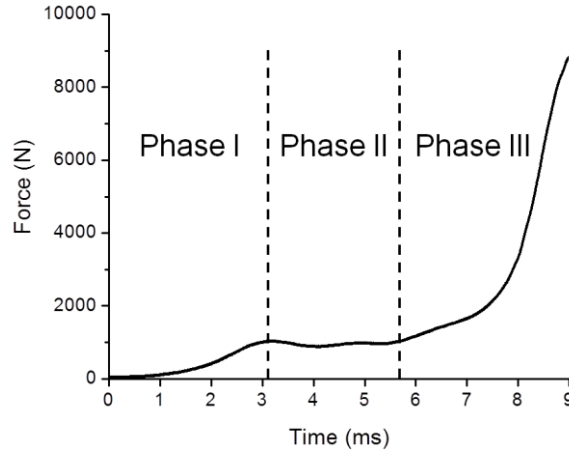


Figure 12. SA_{Pad} characteristic phases of the time-averaged impulse curve at 4.0 m/sec.

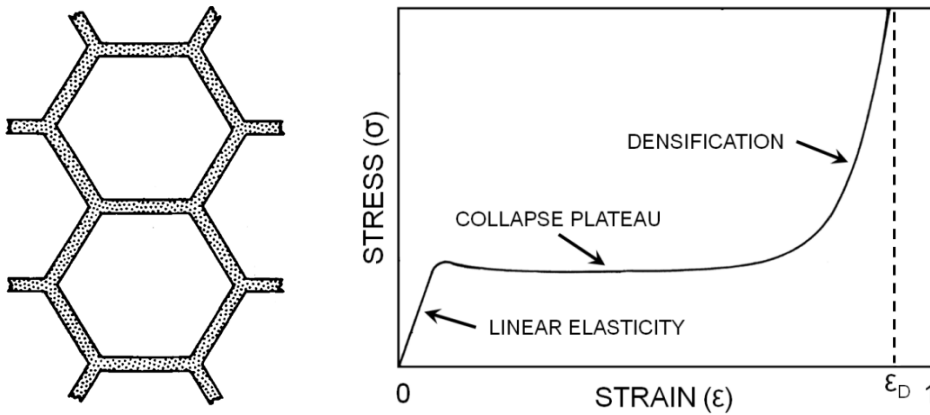


Figure 13. Schematic of (a) hexagonal cells in a cellular solid and (b) a redrawn compressive stress-strain curve of array of identical hexagonal cells or a polymeric elastic-plastic foam (30).

Examination of the shock absorber design revealed the TWC can be approximated by the structure of a single hexagonal cell in a cellular solid (Figure 13a) (30).

Furthermore, the SA_{Pad} and $SA_{No Pad}$ impulse curves exhibited characteristics of schematic stress-strain curves for an array of identical hexagonal cells or a polymeric elastic-plastic foam material under compressive loading. The stress-strain curve is separated into

regimes, or phases, of linear elasticity, collapse plateau, and densification (Figure 13b).

The “phased” compressive behavior of the elastic-plastic foam is managed by the critical yielding force of the hexagonal cell’s side walls, the buckling and complete collapse of the cell, and finally the compressibility of the cell’s constituent material, respectively.

In comparison, published findings (19) characterized prototype TWC force-time curves into regions of elastic deformation, plastic drawing/plateau, and plastic deformation. These descriptions were established from an exploration (22) of the force-time curves and breaking behaviors of thermoplastics subjected to notched Izod testing. The Izod method to measure impact strength applies flexural loading upon the specimen, as opposed to the compressive forces applied during a drop tower impact. In addition, the purpose of the Izod study was to characterize the role that varying post-yield material behaviors have in impact attenuation. Though plastic drawing, plastic deformation, crack propagation, tearing, and delamination were reported for impacted prototypes (19), SA_{Pad} and $SA_{\text{No Pad}}$ post-impact measurement and observation failed to identify non-recoverable dimensional changes, macroscopic cracking/crazing, or visible material separation. As a result, adoption of elastic-plastic foam terminology under compression loading (30) is recommended as it does not necessitate modes of permanent material failure. Therefore, SA_{Pad} and $SA_{\text{No Pad}}$ impulse curves indicate characteristic phases should be: phase I – linear elasticity, phase II – collapse plateau, and phase III – densification.

The phased resistance is claimed to be provided by separate resistive mechanisms (18, 19, 24-26). These impact energy management mechanisms were identified and correlated to the characteristic phases for the SA_{Pad} at 4.0 m/sec (Figure 14). Full compression of the foam-filled pad and the geometric adjustment of the TWC bottom

wall defined phase I. The initial resistive mechanism of side wall stiffness was substantiated via retention of the obtuse side wall angle between image A and image B. Upon overcoming the critical yielding force, the collapse and outward buckle of the TWC side walls occurred throughout phase II. The large reduction in compression height in image C demonstrated the system's fluid venting mechanism. The large spike in force and maximum densification of the SA_{Pad} , as shown in image D, defined phase III.

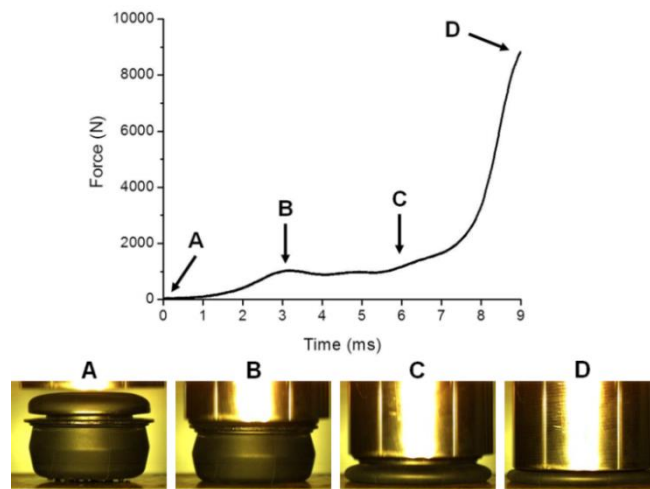


Figure 14. SA_{Pad} impact progression at 4.0 m/sec.

Claim 2: Trapezoidal Force-Time Curve Behavior

The collective behavior of the TWC impact energy management mechanisms is claimed (24-26) to attenuate impact energy via a flattened, trapezoidal force-time curve; however, the range for which this behavior occurs is undefined. Impulse curves defined a trapezoidal curve shape at 2.3 and 3.0 m/sec and substantiated the initial trapezoidal collapse plateau at 4.0 and 4.7 m/sec (Figures 7 and 8). The progression of SA_{Pad} and $SA_{No Pad}$ impulse curve shape (Figure 7) revealed the trapezoidal collapse plateau increased in force, but decreased in duration across escalating impact velocities. The near complete elimination of the trapezoidal collapse plateau is therefore postulated to occur during a high velocity, high rate linear impact above 4.7 m/sec.

Claim 3: Impact Energy Range of Adaptability

The fluid venting mechanism of the TWC is claimed (24-26) to provide adaptability and optimal energy management, i.e., a similar peak force or trapezoidal plateau across varying, yet undefined, impact energy levels. As a result, the range of adaptability of the SA_{Pad} and $SA_{\text{No Pad}}$ was defined to be within 1.3 – 3.0 m/sec. Furthermore, the upper performance parameter of the SA_{Pad} was defined by the full emergence of the leptokurtic region in the 4.0 and 4.7 m/sec impulse curves (Figure 7a). Therefore, the range of linear impact energy management for a single shock absorber was up to a threshold of 3.0 m/sec (25.4 J). Due to the absence of evidence in the literature, it must be assumed that 3.0 m/sec is an acceptable level of function for a liner component within a NOCSAE certified football helmet system where standardized maximum impact velocities to the helmet outer shell are 5.46 m/sec (31). However, on-field impacts to the outer shell, resulting in concussive injury, are reported (32) to exceed 11.0 m/sec. The extent to which these focal, high velocity impacts are diminished prior to inner liner load transfer is also undefined in the literature and thus it is unknown if the 3.0 m/sec threshold would remain acceptable. Therefore, investigation to examine the degree impact energy is attenuated by the outer shell prior to inner load transfer and the degree adjacent absorbers within the inner liner system participate is warranted.

Claim 4: 90% Compressibility

The TWC is claimed to allow for a maximum “ride-down” capacity to approximately 90% of its original height (24-26). Furthermore, the fully densified, “bottomed out” thickness of the air chamber is described (24) to equal twice the thickness of TWC’s cell wall, measured during pilot testing to be 2.0 mm. The SA_{Pad} compression

height at 4.7 m/sec measured approximately double the cell wall thickness and therefore substantiated the 90% “ride-down” capability. Further observation defined that SA_{Pad} densification occurred at the impact velocities that produced a leptokurtic impulse curve. While published findings (16) previously described the spike in force as the system in failure, the patent literature (26) claimed that further energy attenuation is provided via the compressibility of the constituent materials. It is agreed that during phase III the primary impact energy management mechanisms are a function of the SA_{Pad} constituent materials. Thus, further material investigation into the foam-filled pad and thermoplastic TWC is warranted in attempt to reduce F_{COMP} during the densification regime.

Claim 5: Improved Impact Energy Attenuation and Claim 6: Increased Durability

The patent literature specific to the addition of the foam-filled pad component is claimed to improve impact energy attenuation and increase durability across expected service-life cycling (25). Published findings (19) preliminarily discussed a post hoc trial analysis to assess the durability of the prototype TWC component and indicated that there was no significant difference in peak force across ten trials at 1.3 m/sec. However, significant differences existed between the first and second impacts at 2.3 and 3.0 m/sec. As a result, a modified test procedure for SA_{Pad} and $SA_{\text{No Pad}}$ repetitive impact trials was implemented (28) measuring average on-field football impact exposure per game to define the number of trials ($n=15$) and current football helmet testing standards (29) to define the interval (75 ± 15 seconds) between impacts.

The mean F_{COLL} and F_{COMP} values substantiated the impact performance degradation of the shock absorber and provided velocity-specific support for impact energy management claims specific to durability and the addition of the foam-filled pad.

At 1.3 m/sec, $SA_{No\ Pad}$ and SA_{Pad} analysis defined that no appreciable damping or durability benefit was added by the pad. At 3.0 m/sec, the large interaction effect sizes revealed that the addition of the pad slowed the rates of F_{COLL} and F_{COMP} degradation, and therefore substantiated the increase in durability afforded by the SA_{Pad} . At 4.0 m/sec, the medium interaction effect size for F_{COLL} revealed that once again the addition of the pad slowed the rate of degradation. However, the lack of an interaction effect for F_{COMP} suggested that the protective effect of the $SA_{No\ Pad}$ and SA_{Pad} was equivocal. The large between effect size for F_{COMP} substantiated the increase in impact energy attenuation afforded by the pad under full compression, however the large within effect size indicated a general decrease in impact attenuation performance across repetitive impacts. To further improve impact energy attenuation and durability of the shock absorber, further material investigation and engineering of the foam-filled pad component are warranted.

Conclusions

The investigation defined the linear impulse and compression behavior of the Aware-Flow[®] shock absorber. A single shock absorber optimally managed linear impulsive forces up to a 3.0 m/sec (25.4 J) threshold. The addition of the foam-filled pad to the shock absorber improved the attenuation of linear impact energy and increased velocity-specific durability of the SA_{Pad} . The adoption of elastic-plastic foam terminology to re-characterize compression loading behavior was recommended based upon further examination of the absorber design and resultant phased force-time curves. Additionally, the leptokurtic region of the 4.0 and 4.7 m/sec impulse curves substantiated a third phase, defined as densification, as demonstrated by the SA_{Pad} maximum compression height approaching 90%. The progression of SA_{Pad} and $SA_{No\ Pad}$ impulse

curves and peak forces across increasing impact velocities substantiated the instrumented drop tower setup. Collectively, the investigation of impact energy management served to further define and substantiate published findings and product claims. With on-field impacts to the outer shell resulting in concussion reported to exceed 11.0 m/sec, investigation into the degree impact energy is attenuated by the outer shell, prior to inner load transfer and the extent adjacent absorbers participate is warranted. Further investigation into physical, mechanical, and thermal characteristics of the constituent materials of the shock absorber is also warranted.

Collectively, this study determined the performance parameters of off-the-shelf protective head gear components and serves as a suggested model towards the scientific evaluation of product claims. As knowledge surrounding the brain injury of concussion continues to proliferate, a comprehensive understanding of the performance of helmet technology is essential to establish functionality which ultimately serves to abate the injury. The absence of evidence supporting the safety claims of protective head gear and the current culture among manufacturers is showcased by requests for Federal level investigations (4, 5). In contrast, the efforts to make product information openly available and the incorporation of the scientific peer review process during product development are newly exemplified by Xenith[®]. The urgency to mitigate injuries like concussion necessitate that manufacturers, material scientists, and sports engineers continue to partner as a community to engage in fundamental scientific investigations throughout the development and validation of new head gear technology.

References

- 1 Daneshvar DH, Nowinski CJ, McKee AC, et al. The Epidemiology of Sport-Related Concussion. *Clin J Sport Med* 2011 30: 1-17
- 2 Lincoln AE, Caswell SV, Almquist JL, et al. Trends in Concussion Incidence in High School Sports: Prospective 11-year study. *Am J Sport Med* 2011, 39: 958-963
- 3 McCrory P. Future Advances and Areas of Future Focus in the Treatment of Sports-Related Concussion. *Clin J Sport Med* 2011, 30: 201-208
- 4 Udall T. Letter to Consumer Product Safety Commission – Football Helmet Safety Standards. 2010. www.tomudall.senate.gov
- 5 Udall T. Letter to Federal Trade Commission – Misleading Football Helmet Safety Claims. 2011. www.tomudall.senate.gov
- 6 Traumatic Brain Injury Legislation – Updated April 2012. National Conference of State Legislatures, [accessed April 2012]. www.ncsl.org
- 7 Children's Sports Athletic Equipment Safety Act, HR1127, 112th Congress, 1st Session, 2011. www.govtrack.us
- 8 Children's Sports Athletic Equipment Safety Act, S601, 112th Congress, 1st Session, 2011. www.govtrack.us
- 9 Protecting Student Athletes from Concussions Act of 2011, HR469, 112th Congress, 1st Session. 2011. www.govtrack.us
- 10 Hoshizaki TB and Brien SE. (2004). The Science and Design of Head Protection in Sport. *Neurosurgery* 2004, 55(4): 956-967
- 11 Mueller FO. Fatalities from Head and Cervical Spine Injuries Occurring in Tackle Football: 50 Years' Experience. *Clin Sport Med* 1998, 17(1): 169-182

- 12 McCrory P, Meeuwisse W, Johnston K, et al. Consensus Statement on Concussion in Sport 3rd International Conference on Concussion in Sport Held in Zurich, November 2008. *Clin J Sport Med* 2009, 19(3): 185-200
- 13 Benson BW, Hamilton GM, and Meeuwisse WH. Is protective equipment useful in preventing concussion? A systematic review of the literature. *Br J Sport Med* 2009, 43: i56-i67
- 14 Daneshvar DH, Baugh CM, Nowinski CJ, et al. Helmets and Mouth Guards: The Role of Personal Equipment in Preventing Sport-Related Concussions. *Clin J Sport Med* 2011, 30: 145-163
- 15 Xenith Quality Assurance and Quality Control Procedures. 2011. Xenith, LLC.
- 16 Hoshizaki TB and Post A. Impact Attenuation Characteristics of Thin Walled Collapsible Air Chambers in Protective Helmets. *J ASTM Intl* 2009, 6(4): 1-7
- 17 Gimbel G and Hoshizaki TB. A comparison between vinyl nitrile foam and new air chamber technology on attenuating impact energy for ice hockey helmets. *Intl J Sport Sci Eng* 2008, 2(3): 154-161
- 18 Lamb L, Post A, and Hoshizaki TB. Development of a new methodology capable of characterizing the contribution of a controlled venting system to impact attenuation in chamber structures for head protection. *J ASTM Intl* 2009, 6(1): 1-8
- 19 Lamb L and Hoshizaki TB. Deformation mechanisms and impact attenuation characteristics of thin-walled collapsible air chambers used in head protection. *Proc. IMechE, Part H: J. Engineering in Medicine* 2009, 223: 1021-1031
- 20 Xenith X1 Adult Football Helmet Product Catalog. 2009. Xenith, LLC.
- 21 Xenith Football Helmet Product Catalog. 2011. Xenith, LLC.

- 22 Wolstenholme WE. Characterizing Impact Behavior of Thermoplastics. *J Appl Polym Sci* 1962, 6(21): 332-337
- 23 Ferrara VR and Hibchen K. *U.S. Patent Application*. US 2010/0186150 A1. 2010. Washington, DC: U.S. Patent and Trademark Office
- 24 Ferrara VR. *U.S. Patent Application*. US 2011/0047685 A1. 2011. Washington, DC: U.S. Patent and Trademark Office
- 25 Ferrara VR. *U.S. Patent*. US 7,895,681 B2. 2011. Washington, DC: U.S. Patent and Trademark Office
- 26 Ferrara VR. *U.S. Patent Application*. US 2008/0256686 A1. 2008. Washington, DC: U.S. Patent and Trademark Office
- 27 Instron Dynatup 9200 Series Product Brochure. (2009). Instron.
- 28 Crisco JJ, Fiore R, Beckwith JG, et al. Frequency and Location of Head Impact Exposures in Collegiate Football Players. *J Athl Training* 2010, 45(6): 549-550
- 29 NOCSAE 001-11m11. Standard Test Method and Equipment Used In Evaluating The Performance Characteristics Of Protective Headgear/Equipment. National Operative Committee on Standards for Athletic Equipment 2011
- 30 Gibson LJ and Ashby MF. Cellular Solids: Structure and Properties, 2nd Edition. Cambridge University Press: Cambridge UK, 1997
- 31 NOCSAE 002-11m11a. Standard Performance Specification for Newly Manufactured Football Helmets. National Operative Committee Standards for Athletic Equipment 2011
- 32 Pellman EJ, Viano DC, Tucker AM, et al. Concussion in Football: Reconstruction of Game Impacts and Injuries. *Neurosurgery* 2003, 53(4): 799-814

CHAPTER III

QUANTIFYING THE EFFECTS OF ACCELERATED WEATHERING AND LINEAR
DROP IMPACT EXPOSURES OF AN AMERICAN FOOTBALL
HELMET OUTER SHELL MATERIAL

Abstract

American football helmets are subjected seasonally to a myriad of environmental conditions from expected use and storage and yet, are reused without a relational understanding between service life degradation and changes in impact performance. Comprehensive investigations could link rates and degrees of material degradation to scientifically and clinically meaningful changes in helmet performance. Therefore, the purpose of this research was to preliminarily quantify the effects of accelerated weathering on: (i) colorimetric, chemical, fluorescent, and thermal properties, (ii) surface and bulk mechanical properties, and (iii) impact performance of an American football helmet outer shell material. Helmet-grade plaques were exposed to 480 hours of modified ASTM D4587 accelerated weathering. Surface specific shifts ($p < 0.05$) in colorimetric, chemical, fluorescent, thermal, and mechanical properties were observed at the plaque surface. Plaque-derived tensile specimens underwent modified ASTM D638 monotonic tensile testing, and the photo-degraded ~1% of the Weathered plaque surface thickness led to 10%, 12%, and 9% increases ($p < 0.05$) in Young's modulus, yield stress, ultimate tensile stress, respectively. Impact performance was analyzed with a protocol attempting to employ expected on-field impact conditions. Weathered and Non-weathered helmet surrogate systems managed impact energy progressively less effectively across five repetitive trials ($p < 0.05$), yet the absence of significant Weathered

differences demonstrated that the plaque-foam systems performed similarly. Results identified a battery of diagnostic tools to characterize the degradation of outer shell material exposed to accelerated weathering. Thus, the comprehensive approach herein may be used towards the evaluation of additional service life exposures, as well as examine on-field deterioration of full helmet outer shells.

Introduction

Knowledge and data of the brain injury of concussion subsequent to sport participation has grown exponentially over the past 15 years with the majority of efforts focused on etiology, epidemiology, diagnostics, and biomechanics of the injury (1, 2). Although sport-related concussion originates from biomechanical forces imparted directly or indirectly to the head (1, 2), the contemporary football helmet was designed to meet a standard intended to prevent catastrophic injury (e.g., skull fracture) (3-7). The established helmet standards for linear impact performance and sample size determination (3, 4) have effectively decreased catastrophic head injuries (8) and reduced impact forces to the brain (2). However, there is no evidence to support the reduction of the incidence of concussion to athletes (2). While research has demonstrated that the impact energies resulting in concussion can be below the parameters to which helmets are designed to protect against (9), the causal thresholds for a concussive injury are not clearly understood (10). The current gap in protective expectations and design requirements for optimum athlete protection demands greater scientific understanding of how helmet systems serve to manage the impact energies of play.

Modern American football helmet systems are comprised of two main components – the inner liner and the outer shell (Figure 15) (7, 11-13). Helmet shells are

commonly constructed of injection molded engineered polycarbonate (PC) blends (7, 11) which serve to delocalize focal impact energy by effectively distributing and transferring load to the liner system. The liner, commonly consisting of vinyl nitrile (VN) foams (11, 13), continues to compress and deform thereby spreading impact energy over a larger surface area. Thus, impact energy is managed through two mechanisms: extending the time course of the impact event and/or thermo-mechanical dissipation of impact energy (7, 14). The consistent and synergistic function of helmet components is therefore critical for systematic head protection and yet complex to understanding energy management.



Figure 15. Common American football helmet components: (left) vinyl nitrile foam inner liner and (right) injection molded polycarbonate blend outer shell.

Throughout the repetitive on-field collisions at the youth (15-17), high school (18, 19), collegiate (19-21), and professional levels (9, 22), the beginning of impact attenuation is often initiated by contact with the outer shell (22). The cumulative frequency of expected impact events delivered to the helmet shell is extensive, as the total number of impact exposures for an athlete has been reported to reach above 2200 in one season (23). As a result, the shell is required to consistently maintain its protective performance across a broad number of repetitive impacts and throughout its extended life span. A review of the literature reveals a paucity of knowledge toward the degree that the impact performance of a football helmet system is maintained over time compared to its initial certified level of performance (3, 4). Furthermore, primary polymers used in

helmet-grade shell materials are commonly reported to lose critical functional properties over time (24, 25).

The outer shell is subjected to a myriad of environmental conditions under expected use and storage. Such exposures include varying intensities of impact events, temperature ranges, ultraviolet (UV) light, oxygen, moisture, humidity, and chemicals such as adhesives and cleaners. These serve to alter and diminish the constituent materials performance, singularly and in combination, through a series of physical and chemical degradation mechanisms. Specifically, the weathering of PC and polyethylene terephthalate (PET) each consistently result in material property changes (25). On the molecular level, degradation pathways such as photo-degradation, hydrolysis, and thermal-oxidation lead to chain scission events, crosslinking reactions, and formation of small molecule byproducts that disrupt molecular weight, modify morphology and molecular packing, and alter aesthetic properties (25). Microscopically, physical aging from thermal exposure causes structural morphology changes in free volume and crystallinity that macroscopically influence stress-strain behaviors (26). However, the degree and rate that environmental exposures alter material properties of helmet-grade outer shell PC blends is poorly understood. The coalescence of these degradative influences on the impact performance of the contemporary helmet shell was also not found in the open literature.

The impact properties of PC systems are widely reported, but often utilize traditional testing regimes that simplify specimen shapes or inadequately represent protocols as desired for the outer shell (27). These testing approaches commonly impose fracture or irreversible plastic deformation modes typically uncommon during on-field

impacts. Such testing appear to have minimal value towards improving the understanding of impact characteristics of helmet-grade materials under end-use conditions, as helmet shells have not been observed to commonly exhibit catastrophic failure. On the other hand, the testing of full helmet systems exposes helmet-grade materials under the proper geometries and to more accurate on-field conditions. As a brief summary of the literature, helmet systems have undergone repetitive standardized *in situ* linear drop tests (9, 28, 29), pneumatic impact testing protocols (29-31), and end-use collisions during on-field measurements of impact biomechanics (20). An examination of this research emphasis reveals that the comprehensive analysis of helmet performance has not extended beyond biomechanical evaluations and into investigation of potential helmet material property degradation. The analyses are devoid of assessments of material property changes of helmet-grade polymers under on-field environments or replicated end-use conditions. As a result, a bridge of knowledge between helmet materials under traditional polymeric failure testing and full helmet system surrogate testing does not exist (32). Furthermore, outer shells are reused without a publicly available relational understanding between service life degradation and changes in impact performance; potentially decreasing the ability of a helmet system to manage impact energy over its lifecycle. The testing of helmet-grade materials employing expected on-field exposures and accurate impact conditions is therefore warranted.

Scientific study striving to accurately represent weathering-related service life exposures and the subsequent evaluation of functional properties of helmet-grade outer shell materials is required. Such comprehensive investigations could serve to link rates and degrees of material degradation to potentially scientifically and clinically meaningful

changes in helmet performance. The research reported herein will explore a baseline of material characterization tests to quantify chemical, thermal, and mechanical degradation as a result of laboratory weathering. The purpose of this study was to investigate the effects of accelerated weathering on the: (i) colorimetric, chemical, fluorescent, and thermal properties, (ii) surface and bulk (tensile) mechanical properties, and (iii) impact performance of an American football helmet outer shell material.

Experimental

Materials

A helmet grade engineered rubber-toughened, UV-stabilized bisphenol acetone (A) polycarbonate/polyethylene terephthalate (PC/PET) blended material (Figure 16) was procured in pellet form (Makroblend DP UT153, Bayer Corporation, Pittsburgh, PA). The PC/PET blend was dried for 6 hours at 110 °C and then injection molded (VSX 85, Cincinnati Milacron Inc, Cincinnati, OH) using a single cavity mold following the manufacturer's suggested molding parameters into 4" x 6" x 1/8" plaques. The chemical composition of the injection molded plaque was confirmed to match a current helmet manufacturer's off-the-shelf outer shell using infrared spectroscopy and the blend composition of the injection molded plaque was found to be even blend of PC and PET using thermogravimetric analysis (TGA) (see Figure 27 and 28 in Supplemental Information). The plaque thickness was selected to match the measured thickness of an American football helmet outer shell. A non-pigmented resin that resulted in a natural, colored plaque was selected to serve as a baseline to eliminate a potential additional level of complexity, as off-the-shelf outer shells invariably contain additive pigments and colorants that can reportedly alter weathering and degradative properties (25).

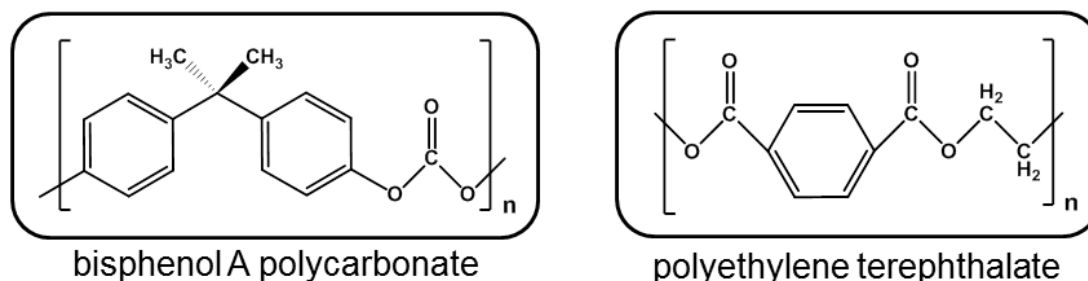


Figure 16. Chemical structures of the primary polymers, (left) bisphenol A polycarbonate and (right) polyethylene terephthalate that comprise the engineered outer shell helmet-grade blend material.

Accelerated Weathering Exposure

Plaques (n=20) were randomly selected from a single manufacturing batch (N=200) to undergo accelerated weathering treatment (AW). Weathered plaques were initially trimmed down to 3" x 5" with a band saw in order to properly fit into the required metal fixturing. The excess sprue and gate material was removed from the top of the plaque, 0.5" of material was removed from each side, and 1" was removed from the bottom (refer to plaque in Figure 19). Non-weathered plaques were also trimmed to 3" x 5". Fixtured plaques were placed into an AW chamber (QUV/Spray, Q-Lab Corporation, Westlake, OH) whereby a 2.5" x 4" window underwent direct UV radiation that reproduced portions of the direct terrestrial sunlight spectrum (Figure 17) (34, 35).

AW was performed following a modified ASTM D4587 procedure for 480 hours (20 days). Weathered plaques underwent a continuous cycle of 4 hours of UV radiation (irradiance: 0.90 W/m²/nm at 340 nm) at 60 °C and 4 hours of condensation at 50 °C (35). Due to the QUV chamber setup, the backsides of fixtured plaques were also exposed to water and elevated heat, albeit to a lesser degree than the exposed side.

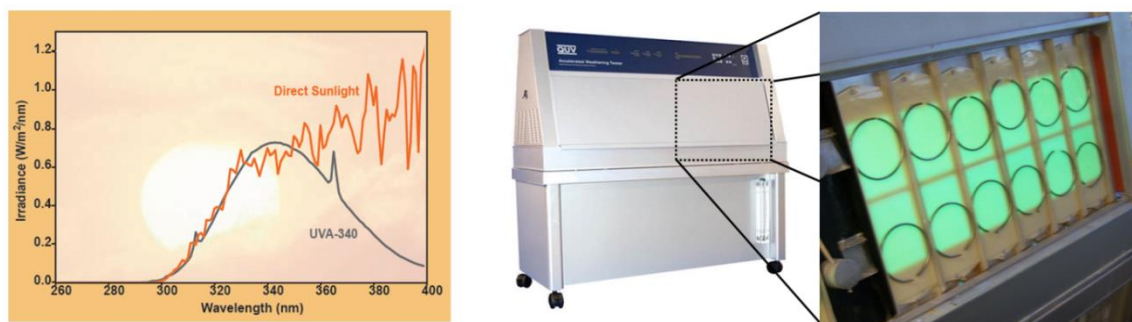


Figure 17. (left) UV spectrum of direct terrestrial sunlight compared to radiation spectrum of UVA-340 nm lamp (33, 34). (right) QUV Accelerated Weathering tester shown with weathered plaques under UV radiation (illuminated 2.5" x 4.0" area).

Colorimetric, Chemical, Fluorescent and Thermal Property Characterization

Surface color change was quantified via yellowing index (YI) per CIELAB scale using a handheld spectrophotometer (Spectro-guide sphere gloss, BYK Gardner, Columbia, MD). A sheet of white paper was placed underneath the sample during testing to eliminate any variable color effects of the substrate under the plaque.

Chemical composition changes at the surface were quantified using benchtop Attenuated Total Reflectance Fourier transform infrared spectroscopy (ATR-FTIR) (Nicolet 6700 ATR-FTIR, Thermo Fisher Scientific Inc., Madison, WI). ATR-FTIR data was collected and analyzed using Omnic software (v8.2, Thermo Fisher Scientific Inc., Madison, WI). The dependent variables examined were the calculated spectral areas of $3000\text{--}2800\text{ cm}^{-1}$ and $1800\text{--}1600\text{ cm}^{-1}$.

The presence of fluorescent molecules was determined via fluorescence microscopy (LSM 710, Zeiss, Thornwood, NY) using a 350 nm laser light source. Depth of fluorescence was quantified using AxioVision software (v 4.9.1, Zeiss, Thornwood, NY). For sample preparation, plaques were cross-sectioned with a band saw.

Thermal property changes were quantified via modulated differential scanning calorimetry (MDSC) (DSC Q2000, TA Instruments, New Castle, DE) in heat-only mode

at a heating rate of 3 °C/min with an amplitude of 0.48 °C every 60 sec. MDSC data was collected and analyzed using Universal Analysis 2000 software (v 4.5A, TA Instruments, New Castle, DE). Samples for analysis were acquired using a microtome (820 Spencer, American Optical Corp, Depew, NY) whereby the slice depth was set to 50 µm and the top 50 µm of the surface was removed. The dependent variables examined were MDSC thermogram peak temperatures, peak areas, and step change temperatures.

Mechanical Property Characterization

Surface mechanical properties were quantified on the nanometer scale using load-controlled quasi-static nanoindentation (TI 900 Triboindenter, Hysitron, Minneapolis, MN) at pre-selected maximum loads of 500, 1000, 1500, 2000, and 2500 µN applied by a Berkovich-type diamond tip. Data was collected and analyzed using TriboScan software (v.7.1, Hysitron, Minneapolis, MN). Specifically, surface properties were measured across the five discrete applied forces and were reported as a function of the depth of surface penetration (graphically corresponding to the five connected points from left-to-right for each surface condition). Samples were harvested directly from plaques using a bandsaw and edges were hand polished using 240 grit sandpaper. Dependent variables examined were depth of surface penetration and reduced modulus. Surface mechanical properties were also quantified on the micrometer scale via surface hardness measurement with a Shore D durometer (502D, PTC Instruments, Los Angeles, CA).

Tensile mechanical properties were measured using a monotonic pull-to-break test (Insight 10, MTS, Eden Prairie, MN) using a 10 kN (2273 lb) load cell at an initial gauge length of 50 mm with a speed of testing of 5 mm/min (corresponding to a strain rate of 0.1 min⁻¹) (36). Stress-strain data was collected using TestWorks 4 software

(v.4.11C, MTS, Eden Prairie, MN). Modified ASTM D638 Type I tensile specimens (strips: 4.0" long x 0.5" wide x 1/8" thick) were harvested directly from plaques using a bandsaw and edges were hand polished using 240 grit sandpaper. The dependent variables examined were initial tensile modulus (referred to in the text as Young's modulus), yield stress, and ultimate tensile stress (UTS).

Linear Drop Impact Testing

Linear drop impact tests were performed upon a football helmet surrogate plaque-foam system (37, 38) comprised of a plaque stacked atop 38 mm thick (two 19 mm blocks) VN600 foam (density: 111 kg/m³) (39) (Figure 18). The plaque was stacked on the VN600 foam such that the surface exposed to direct radiation faced upward. The foam composition and thickness were selected to represent a common inner liner currently used in football helmet systems (11-13). Impact testing was performed using an instrumented drop tower system (Dynatup 9250HV, Instron, Norwood, MA). The drop mass assembly of 5.6 kg contained a 88 kN (20,000 lb) load cell tup and a 63.5 mm diameter (2.5") cylindrical flat steel drop dart (40). Plaque-foam systems were impacted at 5.5 m/sec (4, 5) under ambient conditions (23 °C) against a flat steel anvil and impact velocities were measured using an optical velocity flag. Each plaque-foam system underwent five repetitive impact trials at an interval of 75 ± 15 sec (3, 5). A total of 60 impact trials were conducted. Selected trials were captured with a Phantom v5.1 (Vision Research, INC., Wayne, NJ) color high speed video camera at 2100 frames per second.

Force-time data were collected via Impulse Data Acquisition software (v. 3.2.30, Instron, Norwood, MA). The voltage signal output from the force sensor produced oscillations or 'signal ringing' during impact testing. As a result, force data required a

Savitzky-Golay (SG) smoothing filter at 1501 points of window under a polynomial order of 2 with no boundary conditions (40). The dependent variables examined were peak force and time to peak force.

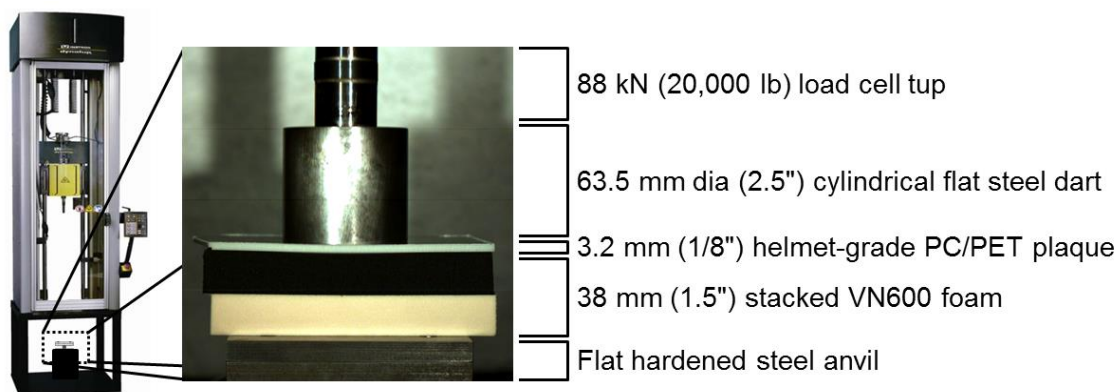


Figure 18. Instron Dynatup 9250HV instrumented drop tower system shown with plaque-foam helmet surrogate system at pre-impact.

Statistical Analysis

Statistical analyses were performed using Statistical Package for Social Sciences software (IBM SPSS, v. 16, IBM Corporation, Sonoma, NY). Alpha level was set a priori at $\alpha = 0.05$. Effect sizes were calculated using Cohen's d for an independent t-test and Cohen's f for an analysis of variance (ANOVA). Post-hoc analyses were performed via Tukey honestly significant difference (HSD) tests. The independent variable for this study was plaque condition with levels that inherently varied across measurement techniques. Tensile and drop impact testing had two plaque condition levels: Non-weathered and Weathered. All other tests had three plaque surface condition levels: Non-weathered (Non-W), the exposed window of a weathered plaque (W_{EXPOSED}), and the backside window of a weathered plaque (W_{BACKSIDE}). A summary of statistical analyses performed, independent and dependent variables, and sample sizes across measurement techniques are described in Table 3.

Table 3

Summary of measurement techniques and statistical analyses performed

Measurement Technique	Independent Variable(s) [#]	Dependent Variable(s)	Sample Size	Statistical Analysis
<u>Colorimetric:</u> CIELAB	(1) Plaque surface condition	(1) yellowing index	n=3	one-way ANOVA with 3 levels (plaque surface condition)
<u>Chemical:</u> ATR-FTIR	(1) Plaque surface condition	spectral areas: (1) 3000-2800 (2) 1800-1600	n=3	two one-way ANOVA with 3 levels (plaque surface condition)
<u>Fluorescence:</u> Microscopy	(1) Plaque surface condition	(1) depth of fluorescence emission	n=3	none
<u>Thermal:</u> MDSC	(1) Plaque surface condition	thermogram bands: (1) six peak areas (2) six peak temp. (3) three step change temp.	n=3	fifteen one-way ANOVA with 3 levels (plaque surface condition)
<u>Mechanical:</u> Nano-indentation	(1) Plaque surface condition (2) Load applied	(1) depth of penetration (2) reduced modulus	n=5	two 3 between (plaque surface condition) x 5 between (load applied: 500-2500 μ N) ANOVA
<u>Mechanical:</u> Hardness	(1) Plaque surface condition	(1) Shore D hardness	n=5	one-way ANOVA with 3 levels (plaque surface condition)
<u>Mechanical:</u> Tensile test	(1) Plaque condition	(1) Young's modulus (2) yield stress (3) ultimate tensile stress (UTS)	n=6	three independent t-tests
<u>Mechanical:</u> Linear drop impact	(1) Plaque condition (2) Impact trial	(1) peak force (2) time to peak force	n=6	two 2 between (plaque condition) x 5 within (trials: 1-5) mixed model repeated measures ANOVA

[#] Plaque surface condition (3 levels): (1) Non-w, (2) W_{EXPOSED}, (3) W_{BACKSIDE}

Plaque condition (2 levels): (1) Non-weathered, (2) Weathered

Table 4

Summary of statistical analyses with statistically significant outcomes

Measurement Technique	Independent Variable	Dependent Variable	Test Statistic	<i>p</i> value	Effect Size	Tukey post-hoc ($p < 0.05$) [#]
CIELAB	Plaque surface condition	yellowing index	$F_{2,6} = 611.02$	$p < 0.001$	$f = 14.11$	1*2, 1*3, 2*3
ATR-FTIR	Plaque surface condition	3000-2800	$F_{2,6} = 61.41$	$p < 0.001$	$f = 4.50$	1*2, 1*3, 2*3
		1800-1600	$F_{2,6} = 117.91$	$p < 0.001$	$f = 6.24$	1*2, 2*3
		band 2 peak area	$F_{2,6} = 6.00$	$p = 0.037$	$f = 0.97$	1*2
MDSC	Plaque surface condition	band 4 peak area	$F_{2,6} = 13.41$	$p = 0.006$	$f = 2.11$	1*2, 2*3
		band 5 peak area	$F_{2,6} = 26.35$	$p = 0.001$	$f = 2.97$	1*2, 1*3, 2*3
		band 5 peak temp	$F_{2,6} = 33.63$	$p = 0.001$	$f = 3.34$	1*2, 1*3, 2*3
		band 6 step temp	$F_{2,6} = 10.32$	$p = 0.011$	$f = 1.85$	1*2, 1*3
		depth of penetration	$F_{2,8} = 57.11$	$p < 0.001$	$f = 3.79$	1*2, 2*3
Nano-indentation	Plaque surface condition	reduced modulus	$F_{2,8} = 453.82$	$p < 0.001$	$f = 10.49$	1*2, 2*3
		Young's modulus	$t = 9.08$	$p < 0.001$	$d = 2.87$	N/A
		yield stress	$t = 27.57$	$p < 0.001$	$d = 8.71$	N/A
Tensile test	Plaque condition	UTS	$t = 14.88$	$p < 0.001$	$d = 4.71$	N/A
		peak force	$F_{4,20} = 578.71$	$p < 0.001$	$f = 5.35$	N/A [%]
Drop impact test	Plaque condition	time to peak force	$F_{4,20} = 611.85$	$p < 0.001$	$f = 7.84$	N/A [%]

[#] 1*2: Non-W*W_{EXPOSED}, 1*3: Non-W*W_{BACKSIDE}, 2*3: W_{EXPOSED}*W_{BACKSIDE}

[%] Post-hoc Tukey HSD was not performed for within main effect

Results

All results (including tables and figures) are reported as mean \pm one standard deviation, unless otherwise noted. A summary of the statistically significant outcomes across measurement techniques is reported in Table 4. Post-hoc analysis that revealed specific sample group combinations that were statistically different from each other were noted as group*group.

Visual Inspection and Colorimetric Characterization

Visual inspection of weathered plaques revealed a darkened, yellowed color change only in the 2.5" x 4" window (Figure 19, left) that was directly exposed to UV radiation (Figure 17). On the backside of the plaque, directly beneath the same 2.5" x 4" window, the material appeared lighter in color. Colorimetric analysis (Figure 19, right) revealed significant differences in YI between plaque surface conditions. Post-hoc analysis revealed significant differences across all three group combinations, with $W_{EXPOSED} * W_{BACKSIDE}$ having the largest difference. YI values were 26.25 ± 0.21 , 30.80 ± 0.38 , and 22.79 ± 0.23 for Non-W, $W_{EXPOSED}$, and $W_{BACKSIDE}$, respectively.

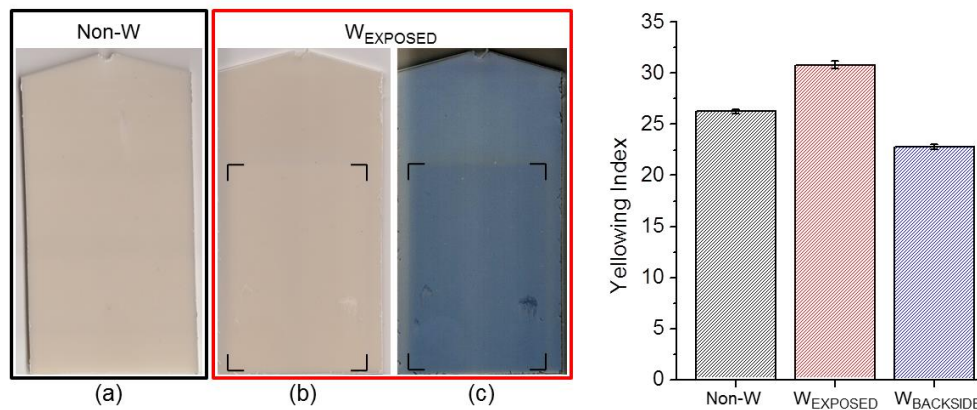


Figure 19. (left) Example of (a) Non-W plaque, (b) $W_{EXPOSED}$ with yellow discoloration of exposed area bracketed, (c) inverted image to highlight the visible area of discoloration. (right) Yellowing Index across plaque surface conditions.

Chemical Property Characterization

ATR-FTIR spectra across plaque surface conditions yielded well-defined, changing bands in the 3000-2800 cm^{-1} and 1800-1600 cm^{-1} regions (Figure 20). Spectral analysis revealed significant differences between plaque surface conditions in 3000-2800 cm^{-1} area and 1800-1600 cm^{-1} area. Post-hoc analysis of 3000-2800 cm^{-1} revealed statistically significant differences across all three group combinations, while 1800-1600 cm^{-1} revealed differences between Non-W*W_{EXPOSED} and W_{EXPOSED}*W_{BACKSIDE}. For both regions, Non-W*W_{EXPOSED} had the largest difference. Spectral areas for 3000-2800 cm^{-1} were 4.33 ± 0.24 , 2.05 ± 0.08 , and 2.52 ± 0.22 for Non-W, W_{EXPOSED}, and W_{BACKSIDE}, respectively. Spectral areas for 1800-1600 cm^{-1} were 1.22 ± 0.47 , 1.49 ± 0.16 , and 1.22 ± 0.32 for Non-W, W_{EXPOSED}, and W_{BACKSIDE}, respectively. Additionally, specific absorption band ranges changed across plaque surface conditions. In the 3000-2800 cm^{-1} region, notable decreases were observed at 2925 cm^{-1} and 2855 cm^{-1} for both W_{EXPOSED} and W_{BACKSIDE}. In the 1800-1600 cm^{-1} region for only W_{EXPOSED}, a broadening of the band at 1720 cm^{-1} was observed with a shoulder formation around 1690 cm^{-1} .

Fluorescence Microscopy

A fluorescence response (Figure 21) was exhibited at the surface of W_{EXPOSED}, yielding a depth of emission of $32.89 \mu\text{m} \pm 1.71$. No fluorescence response was observed across the surface for Non-W and W_{BACKSIDE} plaque surface conditions.

Thermal Property Characterization of Surface Layer

Examination of heat flow MDSC thermograms (Figure 22) across plaque surface conditions revealed several distinctive bands: (1) exothermic peak around 70 °C, (2) endothermic peak around 75 °C, (3) exothermic peak around 125 °C, (4) endothermic

peak around 140 °C, (5) exothermic peak around 200 °C, and (6) endothermic peak around 255 °C. Non-reversible heat flow thermograms exhibited bands 1-5 and an additional step change around band 6. Reversible heat flow thermograms exhibited band 6 and revealed step changes around bands 2 and 4.

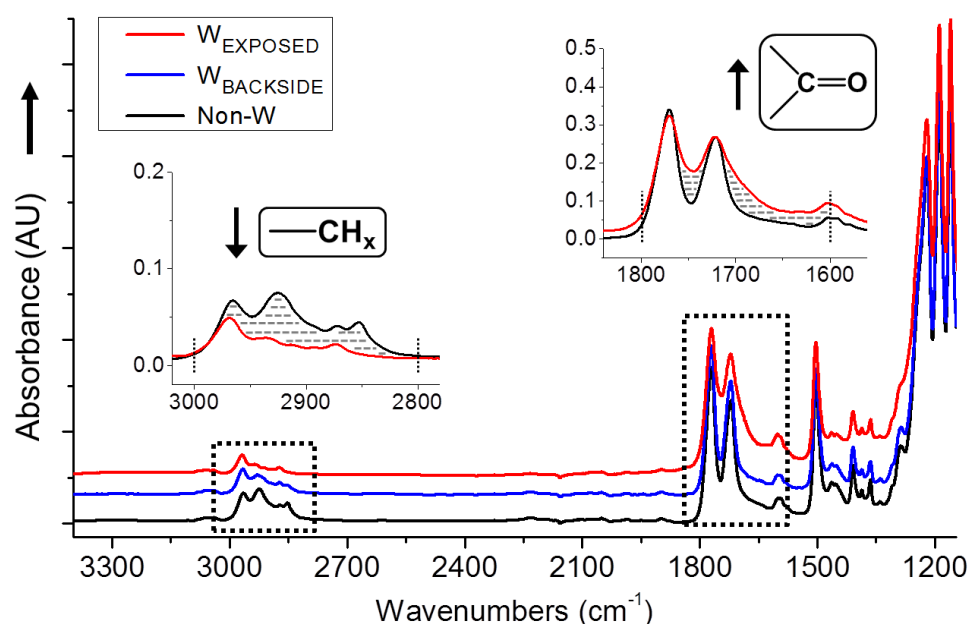


Figure 20. Full ATR-IR spectra across plaque surface conditions. Inset spectra showcase the differential of Non-W and W_{EXPOSED} area specific to alkyl consumption (\downarrow -CH_x) at 3000-2800 cm^{-1} and carbonyl linkage(s) formation (\uparrow -C=O) at 1800-1600 cm^{-1} .

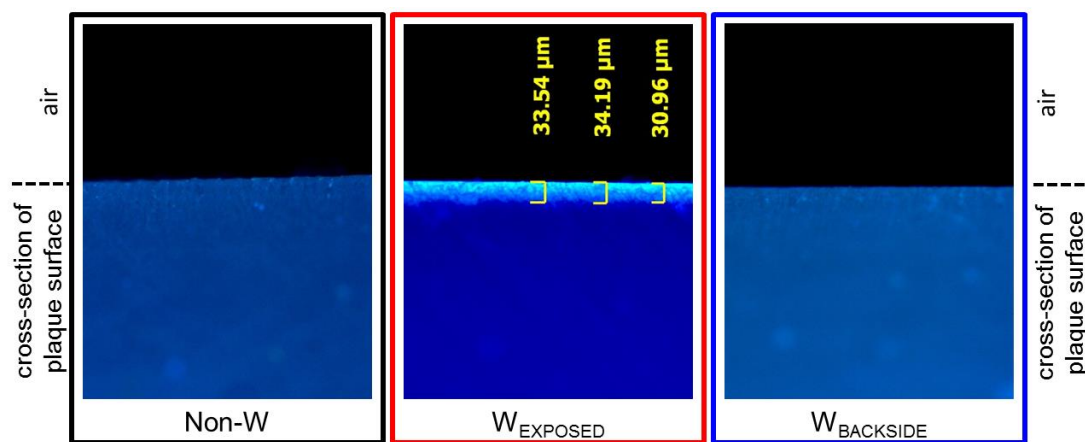


Figure 21. Fluorescence response (350 nm last light source) across plaque surface conditions. Only the W_{EXPOSED} surface exhibited a fluorescence emission (illuminated depth of $\sim 30\text{-}35$ μm).

Analysis of peak areas and temperatures (Table 5, 6 and 7) revealed significant differences between plaque surface conditions in the band 2 and 4 peak area, band 5 peak area, band 5 peak temperature, and band 6 step change temperature. Post-hoc analysis revealed significant differences for: (i) band 2 peak area for Non-W*W_{EXPOSED}, (ii) band 4 and 5 peak area, and band 5 peak temperature across all three group combinations, and (iii) band 6 step change temperature for Non-W*W_{EXPOSED} and Non-W*W_{BACKSIDE}. For all post-hoc differences, Non-W*W_{EXPOSED} had the largest difference, except band 6 step change temperature.

Table 5

MDSC Heat Flow thermogram peak temperatures across plaque surface conditions

Plaque surface condition	Band 1 Peak Temp (°C)	Band 2 Peak Temp (°C)	Band 3 Peak Temp (°C)	Band 4 Peak Temp (°C)	Band 5 Peak Temp (°C)	Band 6 Peak Temp (°C)
Non-W	69.3 ± 0.9	77.2 ± 0.5	127.6 ± 1.3	141.1 ± 0.3	203.6 ± 0.6 ¹	257.9 ± 0.5
W _{EXPOSED}	70.3 ± 0.3	76.7 ± 0.6	124.9 ± 1.4	140.6 ± 0.9	193.6 ± 1.9 ¹	255.8 ± 1.3
W _{BACKSIDE}	70.0 ± 0.3	77.0 ± 0.4	126.5 ± 1.3	140.5 ± 0.5	198.4 ± 1.6 ¹	257.7 ± 0.4

* Matching superscript number denotes Tukey HSD post-hoc combination was statistically different (p<0.05)

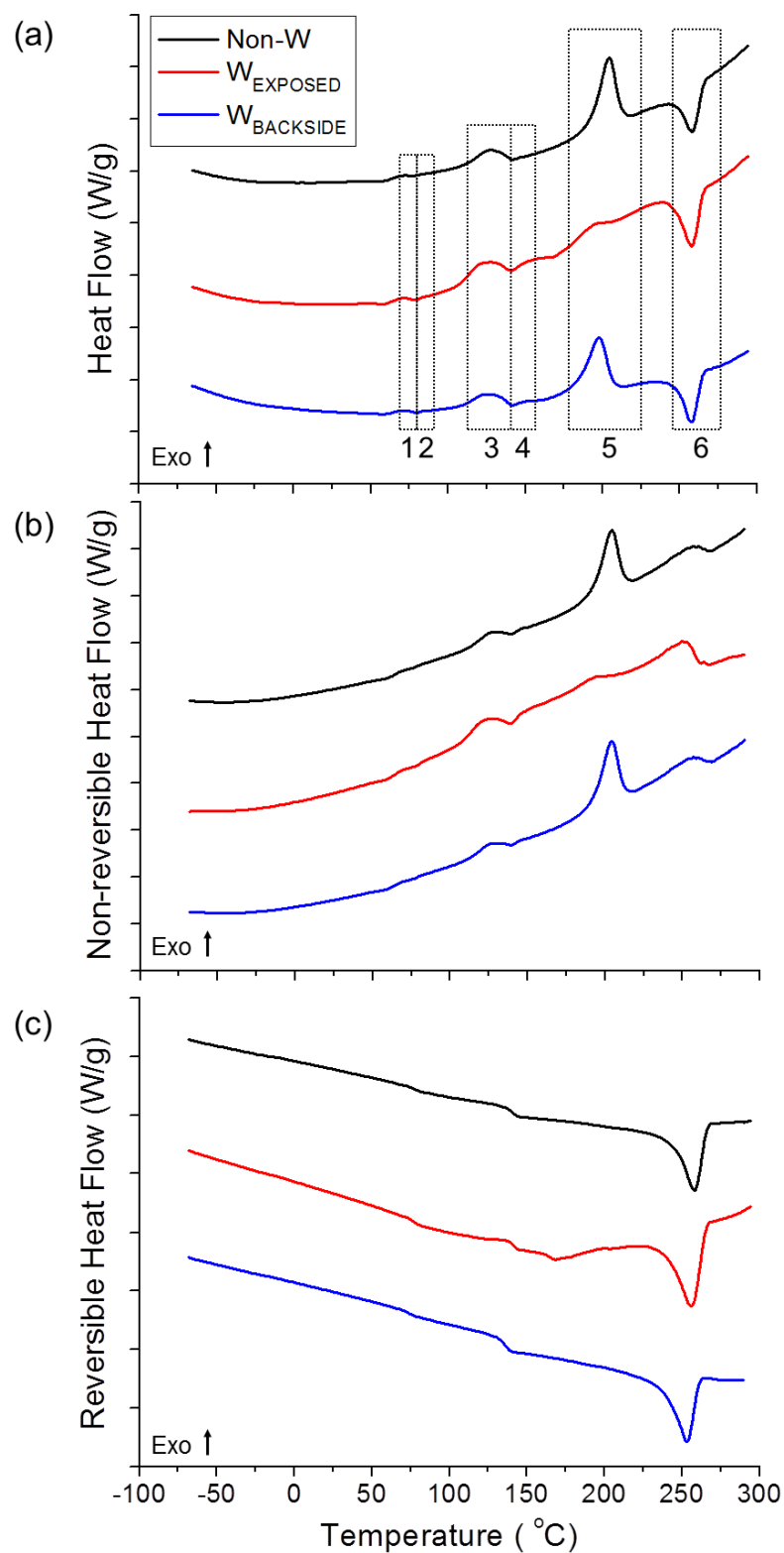


Figure 22. MDSC thermograms across plaque surface conditions for (a) total heat flow, (b) non-reversible heat flow, and (c) reversible heat flow. Note: The general locations of the six distinctive bands are highlighted in the total heat flow plot.

Table 6

MDSC Heat Flow thermogram peak areas across plaque surface conditions

Plaque surface condition	Band 1 Peak Area (J/g)	Band 2 Peak Area (J/g)	Band 3 Peak Area (J/g)	Band 4 Peak Area (J/g)	Band 5 Peak Area (J/g)	Band 6 Peak Area (J/g)
Non-W	0.14 ± 0.04	0.07 ± 0.03 ¹	1.70 ± 0.6	0.61 ± 0.03 ²	19.7 ± 4.4 ⁴	16.4 ± 4.8
W _{EXPOSED}	0.22 ± 0.03	0.15 ± 0.02 ¹	2.54 ± 0.6	0.92 ± 0.11 ^{2, 3}	0.8 ± 0.3 ⁴	11.7 ± 2.0
W _{BACKSIDE}	0.24 ± 0.03	0.10 ± 0.03	1.78 ± 0.2	0.59 ± 0.10 ³	11.7 ± 3.4 ⁴	10.9 ± 5.6

* Matching superscript number denotes Tukey HSD post-hoc combination was statistically different (p<0.05)

Table 7

MDSC Reversible and Non-reversible thermogram step change temperatures across plaque surface conditions

Plaque surface condition	Reversible: Band 2 Step Change Temp (°C)	Reversible: Band 4 Step Change Temp (°C)	Non-reversible: Band 6 Step Change Temp (°C)
Non-W	76.9 ± 0.5	140.7 ± 0.3	262.8 ± 1.0 ^{1, 2}
W _{EXPOSED}	76.6 ± 0.4	140.6 ± 0.7	255.8 ± 1.2 ¹
W _{BACKSIDE}	77.1 ± 0.4	140.5 ± 0.5	257.7 ± 2.8 ²

* Matching superscript number denotes Tukey HSD post-hoc combination was statistically different (p<0.05)

Nanoindentation Surface Mechanical Property Characterization

Quasi static nanoindentation analysis revealed significant effects between plaque surface conditions for depth of surface penetration and reduced modulus. Post-hoc analysis of both depth of penetration and reduced modulus revealed significant differences between Non-W*W_{EXPOSED} and W_{EXPOSED}*W_{BACKSIDE}. Additional analysis

revealed that as the maximum applied load increased ($500\ \mu\text{N} \rightarrow 2500\ \mu\text{N}$) the difference in depth of penetration between W_{EXPOSED} and the other two surface conditions increased ($\sim 70\ \text{nm} \rightarrow \sim 150\ \text{nm}$) for a specific applied load (Figure 23).

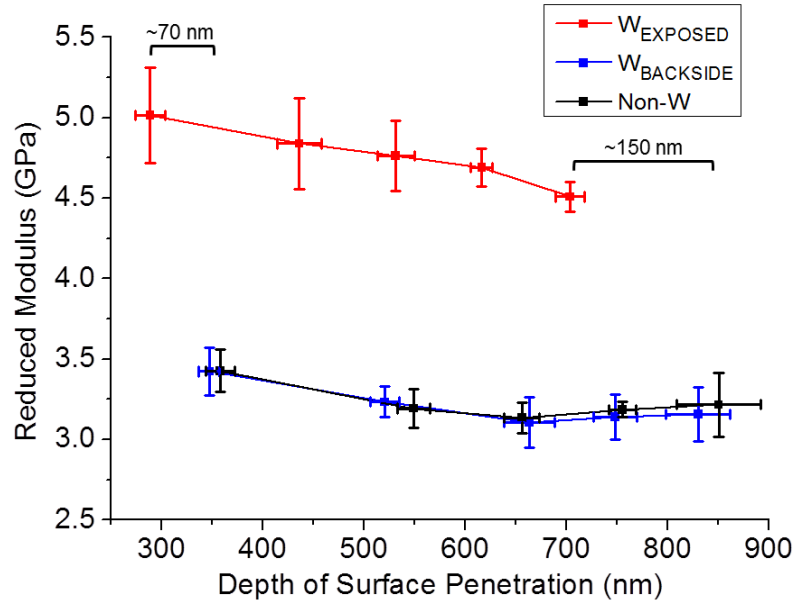


Figure 23. Reduced modulus as a function of depth of surface penetration across plaque surface conditions.

Durometer Surface Mechanical Property Characterization

No significant differences were found for Shore D hardness across plaque surface conditions. Shore D hardness values for Non-W, W_{EXPOSED} , and W_{BACKSIDE} were 85.2 ± 0.8 , 86.2 ± 0.8 and, 85.4 ± 1.2 , respectively.

Tensile Mechanical Property Characterization

Stress-strain tensile analysis revealed significant differences between plaque conditions across Young's modulus, yield stress, and UTS. The characteristic stress-strain curve shapes between plaque conditions were observed to be equivalent (Figure 24); however, Weathered plaques had higher values across measured tensile mechanical properties (Table 8).

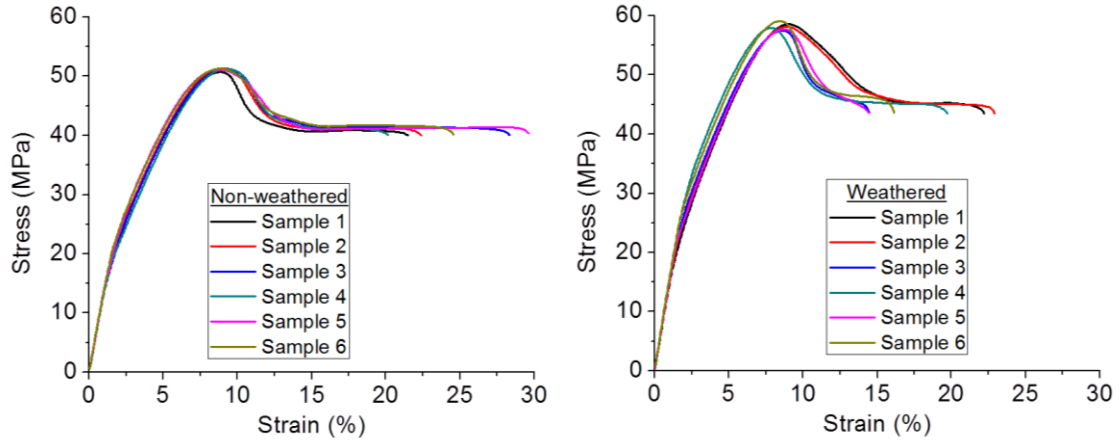


Figure 24. Stress-strain curves for (left) Non-weathered and (right) Weathered plaque conditions.

Table 8

Tensile mechanical properties between plaque conditions

Plaque condition	Young's modulus (MPa)	yield stress (MPa)	ultimate tensile stress (MPa)
Non-weathered	1386.8 ± 16.4^1	51.1 ± 0.2^2	40.9 ± 0.4^3
Weathered	1548.6 ± 40.5^1	58.1 ± 0.6^2	44.9 ± 0.5^3

* Matching superscript number denotes Tukey HSD post-hoc combination was statistically different ($p < 0.05$)

Linear Drop Impact Testing

Equivalent force-time curve shapes were observed for Non-weathered and Weathered plaque-foam systems. However, changes within shape occurred between trials 1 and 2, but remained consistent across trials 2-5 for each plaque (Figure 25, left). Significant main within effects were observed for peak force and time to peak force. Weathered plaque systems produced higher peak forces and time to peak forces for all five trials (Figure 25, right); however, no significant differences were found between plaque conditions.

High speed video revealed severe plaque deformation and VN600 foam compression during impact testing of both Non-weathered and Weathered plaques (Figure 26, left). Visual inspection of plaques post-impact revealed that final curvature was minimal, and each plaque recovered to the original shape after five trials. Additionally, the plaque backside displayed impact-induced rings of whitening that matched the cylindrical drop dart diameter after each impact (Figure 26, right).

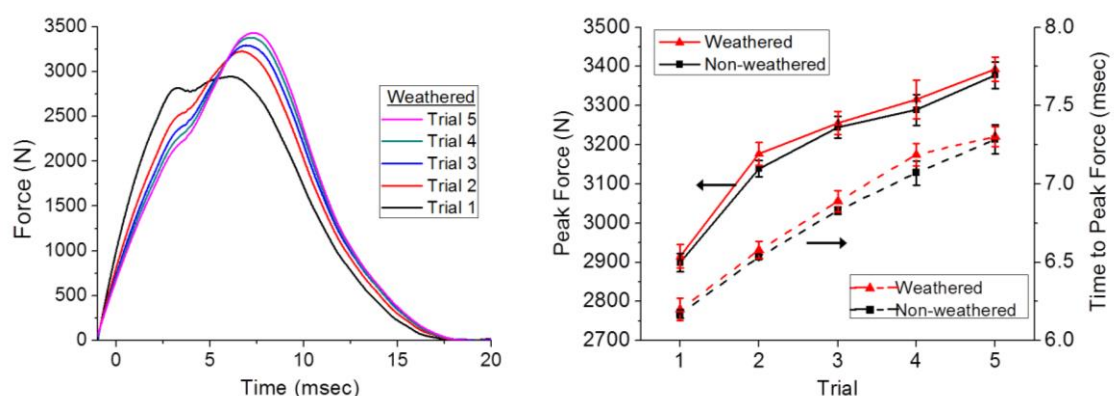


Figure 25. (left) Smoothed force-time curves for a single representative Weathered plaque-foam system across five repetitive impact trials. (right) Peak force and time to peak force across five repetitive trials on Weathered and Non-weathered plaque-foam systems.

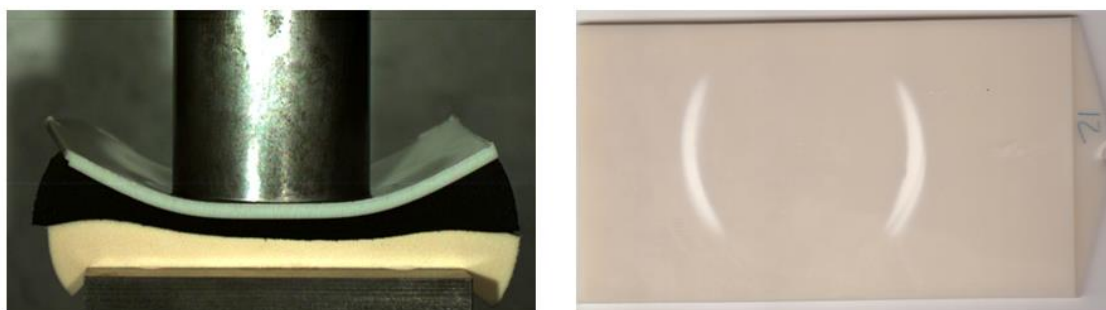


Figure 26. (left) Maximum compression and deformation of plaque-foam system during an impact test. (right) Backside of a Weathered plaque after five impact trials displaying impact-induced rings of whitening.

Discussion

Outdoor weathering is a dynamic environmental condition that can strongly depend on the location and the time of year. Exposures can include direct sunlight,

elevated and sub-ambient temperatures, humidity, moisture, salt water, ozone, and other airborne chemicals (25). The AW used in this study was selected to replicate extended cyclic outdoor exposure of an American football helmet outer shell material in a warm, humid climate. Thus, the discussion and interpretation of the results will focus primarily around the exposures and degradative processes related to UV radiation, oxygen, water, and elevated temperature. Furthermore, the ability to precisely predict the amount of natural outdoor weathering that 480 hours of AW exposure represented is complex, and no universally accepted correlation currently exists (41, 42). However, AW in a laboratory setting is suitable because natural outdoor conditions are highly variable (43). Additionally, the lack of control over exposure conditions and atmospheric pollutants may disrupt valid analysis and confident understanding (25).

Visual Inspection and Colorimetric Characterization

Visual discoloration of the plaque surface was observed (Figure 19) within the 2.5" x 4.0" window produced by the QUV fixturing (Figure 17) following 480 hours of AW exposure. The large effect size for YI (Table 4) revealed a considerable shift in color within the PC/PET helmet-grade material. The significant post-hoc increase for Non-W*W_{EXPOSED} and YI decrease for Non-W*W_{BACKSIDE}, each with similar magnitudes in YI, demonstrated that direct exposure to UV radiation elicited chromophoric change.

Color changes in PC and PET systems have been reported as a result of individual and combined exposures to UV light, elevated temperatures, and oxygen. Exposure to shorter UV wavelengths (less than 350 nm) are reported to initiate photolysis reactions that produce aromatic molecular species (44, 45) which are responsible for yellowing in PC (46-52) and in PET (53-57). With the additional presence of oxygen, photo-oxidation

reactions are reported in PC (44, 58-60) and PET (45, 55) to trigger the generation of additional polyconjugated chromophoric species causing yellowing. Conversely, exposures to longer UV wavelengths are reported to bleach PC (47, 49, 50) whereby existing colored molecular species generated during polymer synthesis and processing are quenched (50, 61). Furthermore, the thermal-oxidation yellowing and bleaching of PC is reported at elevated and sub-ambient temperatures, respectively (44, 48, 50, 62). Similarly in PET, elevated thermal-oxidation reactions are reported to generate yellowing species (63, 64). As a result, we postulate the following: (i) direct exposure of the W_{EXPOSED} surface to shorter UV wavelengths, combined with the presence of oxygen and elevated temperatures, induced yellowing of the helmet-grade material; (ii) exposure to only long UV wavelengths (as shorter UV wavelengths were absorbed by the bulk material) induced the bleaching of W_{BACKSIDE} ; and (iii) the lack of visual color change beyond the 2.5" x 4.0" window on both the front and backside, supports that the effects of thermal-oxidation reactions were minimal.

Chemical Property Characterization

The photo-degradation of PC and PET is a surface specific phenomenon (54, 58). Therefore, helmet-grade plaques were analyzed with ATR-FTIR, a surface-level chemical analysis technique. Well-defined spectral peaks were observed in the 3000-2800 cm^{-1} and 1800-1600 cm^{-1} regions for Non-W that represented strong alkyl composition ($-\text{CH}_x$) and the presence of carbonyl linkages ($-\text{C}=\text{O}$), respectively (Figure 20) (49, 57, 60, 65). The large effect sizes for 3000-2800 cm^{-1} and 1800-1600 cm^{-1} areas (Table 4) revealed a considerable reduction in alkyl groups along with a substantial growth in carbonyl linkages, respectively (Figure 20). For 3000-2800 cm^{-1} , the

significant post-hoc decrease across all combinations, with Non-W*W_{EXPOSED} having the largest difference, demonstrated that direct exposure to UV radiation prompted the drop in alkyl character. For 1800-1600 cm⁻¹, equivalent significant post-hoc increases for Non-W*W_{EXPOSED} and W_{EXPOSED}*W_{BACKSIDE} demonstrated that direct exposure to UV radiation to the exposed surface elicited the growth in carbonyl character.

The spectral peaks at 2925 and 2853 cm⁻¹ represented alkane and alkene functional groups, respectively, and the consumption of these alkyl groups is reported to occur via exposure to short UV wavelengths during photo-degradation for PC (59, 60, 62) and PET (45, 53, 66). The observed broadening of the 1720 cm⁻¹ band is reported to represent the formation of several carbonyl derivatives: aliphatic chain ketones and acids around 1720 cm⁻¹, as well as aromatic chain ketones and acids around 1690 cm⁻¹ (54, 57, 59, 62). The thermal-oxidation of PC and PET is reported to also induce a loss in alkyl character but at very elevated temperatures (48, 62-64). Further, the lack of peak growth around the 3500-3300 cm⁻¹ region suggested minimal water uptake that would serve to initiate hydrolysis reactions (49, 67, 68). However, in general, photo-oxidation reactions are reported to accelerate in the presence of water and higher temperatures (69). Thus we postulate the following: (i) exposure of W_{EXPOSED} to short UV wavelengths and oxygen, along with the presence of elevated temperatures and water, induced the consumption of alkyl groups and generation of carbonyl derivatives; and (ii) for W_{BACKSIDE}, the loss of alkyl character without additional carbonyl peak formation is postulated to be the result of a very low concentration of short UV exposure leading to a substantially slower rate of photo-degradation, but further investigation is required to confirm this hypothesis.

Fluorescence Microscopy

The generation of fluorescent species in PC (60, 70) and PET (56, 66, 71) due to photo-degradation reactions has been reported. Thus, fluorescence microscopy (350 nm laser light source) was used to identify the presence of photo-degraded species at the surface of the helmet-grade plaque following AW. The observed fluorescence response (Figure 21) support colorimetric and ATR-IR findings that suggest the formation of small molecules due to photo-degradation mechanisms. Examination of the $W_{\text{EXPOSED CROSS-}}$ section quantified the depth of fluorescent species at 30-35 μm , which matched previously reported depths of photo-degradation for PC (49, 58, 59, 62, 72) and PET (54). As a result, photo-degradation disrupted the top $\sim 1\%$ layer of the plaque. We posit that aromatic derivatives (56, 60, 66, 70, 71) provided the fluorescence response in the helmet-grade material, but further investigation would be required to determine the precise profile and concentration of fluorescent species created.

Thermal Property Characterization of Surface Layer

In addition to studying the molecular-level chemical changes caused by AW exposure, thermal properties were elucidated to gain concurrent understanding towards micro-level morphology changes at the surface. By determining the depth of photo-degradation using fluorescence microscopy, the deteriorated material was effectively identified into the W_{EXPOSED} surface. A microtome was used to harvest and isolate the top 50 μm ; however, it is to be noted that potentially, all non-degraded material was not fully excluded because it was a manual process. Additionally, MDSC was selected to enable separation of reversible and non-reversible thermal phenomena that would otherwise overlap and potentially convolute a conventional DSC thermogram (73).

The morphological complexity of the helmet-grade PC/PET blend material was exhibited by the MDSC thermograms which contained six distinctive bands and three step changes (Figure 22). The Reversible step changes around 75 °C and 140 °C corresponded to the glass transition temperature (T_g) of PET and PC, respectively (73). The Non-reversible step change around 260 °C represented the onset of complete melting of all crystallites and the subsequent cessation of recrystallization events at the melting temperature (T_m) of PET (74, 75). The endothermic bands 2 and 4 corresponded to the enthalpy recovery that occurred near the T_g of PET (76) and PC (77), respectively. Enthalpy recovery corresponds to the thermal history of the helmet-grade material, which serves to quantify the degree of physical aging. The exothermic bands 1 and 3 that preceded bands 2 and 4, respectively, were representative of pre- T_g artifacts (73, 78). The band 5 exotherm was characteristic of the cold crystallization temperature (T_{CC}) of PET and the band 6 endotherm matched the T_m of PET (74, 79).

The large effect sizes in PET T_{CC} peak area and peak temperature (Table 4) demonstrated a substantial change in the degree of crystallization at the $W_{EXPOSED}$ and $W_{BACKSIDE}$ surfaces. The results support colorimetric, ATR-IR, and fluorescence findings whereby an increase in PET crystallinity is expected to occur as a result of the thermal, UV, and water exposures. For thermally annealed films, a similar trend in PET T_{CC} peak area and peak temperature is reported (80, 81). The photolysis and hydrolysis of PET is reported to induce the scission of polymer chains and entanglements, leading to reductions in molecular weight, and allowing smaller polymer segments to gain the mobility to crystallize (75, 79, 82). This is often called chemi-crystallization, and is more facile in the presence of elevated temperatures. The 60 °C air temperature of the QUV

chamber combined with the absorbance of UV radiation was posited to elevate the W_{EXPOSED} surface temperature near the T_g of PET. The lack of change in PET T_m peak temperature (Table 5) demonstrated a stability of formed crystalline domains; yet the large effect size for T_m step change (Table 4) supports a decrease in crystallinity from AW exposure due to the lower temperature to cease all melting (75).

The large effect sizes for the enthalpy recovery peak areas (bands 2 and 4) near the T_g s of PET and PC (Table 4) revealed effects of physical aging; however, the small values suggest minimal substantial thermal property effects. The observed Non-reversible exothermic pre- T_g artifacts were characteristic of what can sometimes precede an enthalpy recovery peak (78), which is related to physical aging (80). In short, physical aging is the thermally-driven phenomenon of a polymeric system to return to its favorable equilibrium state (83) and the degree to which this has happened is characterized by quantifying the endothermic enthalpy recovery peak area around T_g in a DSC thermogram. For an American football helmet outer shell, the engineered material blend is put into a thermodynamically unfavorable state via rapid quenching during the injection molding process. The introduction of heat, e.g., AW exposure, will facilitate the system to thermally re-equilibrate, or physically age, towards its favorable state.

In summary for W_{EXPOSED} , post-hoc analysis revealed a nearly complete reduction in PET T_{CC} peak area and a substantial shift in PET T_{CC} temperature compared to other plaque surface conditions. As a result, we postulate that exposure to UV light in the presence of water and elevated temperatures facilitated the cold crystallization of PET during AW exposure. For W_{BACKSIDE} , the less severe loss in PET T_{CC} peak area and drop

in peak temperature are postulated to be due to the absence of photolysis with an increase in temperature only from the air chamber.

Surface Mechanical Property Characterization (Nanoindentation)

Recent investigations using nanoindentation has demonstrated its viability to spatially characterize modifications to surface mechanical properties on the nanometer scale of weathered PC systems (72, 84). Thus, surface properties of the helmet-grade material were quantified (Figure 23) using quasi-static nanoindentation at five discrete applied loads. The large between effect sizes (Table 4) for reduced modulus and depth of penetration revealed that AW exposure altered mechanical properties at the surface. The significant post-hoc increase in modulus and decrease in depth of penetration for Non-W*W_{EXPOSED} and W_{EXPOSED}*W_{BACKSIDE} demonstrated that direct exposure to UV radiation induced a substantial increase in resistance to deformation (i.e., stiffness increase). The results also support that the complete PET cold crystallization during AW exposure potentially contributed to the increased surface embrittlement and hardening.

The increase in stiffness matched previously reported nanoindentation analysis of laboratory weathered PC; however, the authors postulated that the increase in nano-T_g was elicited only by cross-linking reactions (72). Cross-linking is reported at the surface of photo-degraded PC (58, 84, 85) to develop a layer between 50 nm (85) - 3 μm (58) thick. In addition to cross-linking reactions, we recommend additional stiffening effects potentially due to physical aging mechanisms (86). The physical aging of PC and PET is reported to reduce available molecular-level volume that provides mobility to polymer chains, thus leading to denser material and stiffer mechanical properties (76, 83, 86, 87).

Durometer Surface Mechanical Property Characterization

The quantification of surface mechanical properties on the micrometer scale was performed by traditional Shore D hardness measurements using a handheld durometer. The lack of Shore D differences between the three plaque surface conditions, compared to the increase in reduced modulus at the nanometer scale, demonstrated a sensitivity difference between the two surface mechanical property measurement techniques. While the precise maximum applied load during Shore D testing was unknown, we postulate that the force was much larger than that for nanoindentation (2500 μN). As a result, the analysis suggested that Shore D durometers are potentially overly forceful to quantify shifts in surface mechanical properties of injection molded American football outer helmet shell materials exposed to AW.

Tensile Mechanical Property Characterization

Analyzing bulk mechanical properties is a first step in order to understand how micro-level scale degradation is affecting macro-level properties of helmet-grade material. Tensile mechanical properties between Non-weathered and Weathered plaque conditions were quantified using a modified ASTM D638 monotonic tensile test protocol. While the speed of testing (5 mm/min), strain rate (0.1 min^{-1}), the use of sand paper for final sample preparation, and width of the specimen narrow section matched D638 setup conditions, modified Type I specimens (strips: 4.0" x 0.5" x 0.125") were harvested directly from plaques using a band saw and the edges were manually sanded to eliminate flash and burrs prior to testing. A limitation of our tensile samples was the inability to precisely obtain a blemish-free finish during harvesting. As a result, strain at break was

highly variable (Figure 24) due to stress-concentrating defects present along the edges of samples, and therefore was not reported.

The large effect sizes for Young's modulus, yield stress, and UTS (Table 4) demonstrated that 480 hours of AW exposure resulted in a significant shift in tensile mechanical properties. The increase in Young's modulus (Table 8) revealed an increased resistance to deformation. The results support the increased degree of ageing and/or crystallization, and the increased reduced modulus for W_{EXPOSED} . The increase in yield stress demonstrated an elevated onset of bulk-level irreversible viscoelastic deformation, and supports the decreased depth of penetration for W_{EXPOSED} at a specific applied load during nanoindentation testing. The increase in UTS demonstrated an increase in the applied stress required during the post-yield drawing phase to maintain a constant testing speed of 5 mm/min. During post-yield drawing, polymer chains align themselves, or flow, in the direction of the applied stress (88). On a molecular-level, drawing is strongly influenced by chain entanglement concentration and intermolecular forces which are directly impacted by morphological changes, e.g., ageing and crystallinity. Overall, the tensile results support that the increase in surface-level stiffness led to a significant bulk-level shift in mechanical properties whereby the top ~1% of the plaque surface postulated to be photo-degraded led to a 10% increase in Young's modulus, a 12% increase in yield stress, and a 9% increase in UTS.

The tensile testing of PC systems exposed to AW is reported to induce increased and decreased shifts in measured properties (46, 89, 90), yet exposure to thermal annealing has induced an increase in yield stress (87). Tensile testing of PET exposed to photo-degradation (56, 57) and AW (65) reported a consistent drop in mechanical

properties, yet exposure to annealing resulted in an increase in mechanical properties (81). In general, two surface processes reportedly affect the results of tensile testing weathered samples – chemical reactions and morphological changes (25). The control of gradual property increase or decrease is governed chemically by the ratio of chains scissions to crosslinks and morphologically by the unpredictable formation location and number of cracks, discontinuities, and defects.

Linear Drop Impact Testing

The impact performance of Non-weathered and Weathered helmet surrogate plaque-foam systems was analyzed using an instrumented drop tower and a protocol attempting to employ expected on-field impact conditions to an outer shell material. The testing utilized validated parameters and peer-reviewed setups from literature to guide the initial selection of input parameters. The impacting mass and velocity, as well as the time interval between the five repetitive trials, matched established helmet testing standards (3-5). The steel anvil and flat cylindrical dart matched a previously substantiated impact setup engineered to analyze American football helmet components (40). The constituent plaque and foam materials of the helmet surrogate, as well as the selected thicknesses and densities, were employed to replicate a common American football helmet design (11-13). Furthermore, the plaque-foam system eliminated anticipated geometrical effects of the shell component (37) that could potentially confound the focused interpretation of the results toward the material response. Overall, our linear drop test protocol served as a first step to bridge the gap between traditional polymeric testing regimes that elicit failure to standard samples and full helmet system

surrogate testing, in order to better understand how representative helmet shell materials and designs are managing impact energy.

The large within effect sizes (Table 4) for peak force and time to peak force for Non-weathered and Weathered plaque-foam systems revealed that helmet surrogates managed impact energy progressively less effectively across each of the five trials (Figure 25). The absence of significant between differences in peak force and time to peak force for Non-weathered and Weathered plaque-foam systems, along with equivalent force-time curve shapes between plaque conditions, revealed that helmet surrogate systems performed similarly. Interestingly, Weathered systems were visually observed to produce both higher mean peak force and mean time to peak force consistently across all five trials (Figure 25, right); however, further investigation is required to confidently elucidate the potential shift in impact properties.

Linear drop impact results suggest that the AW did not alter the impact performance of weathered helmet-grade material. However, potential factors are postulated to cause the lack of a between effect: (i) with only ~1% of the plaque thickness posited to be heavily photo-degraded, the remaining bulk material potentially had sufficient retention of impact performance properties to compensate for the surface-level deterioration, and (ii) the impact protocol produced strain rates that were potentially too aggressive, such that quantifiable differences between plaque conditions may have been precluded. This is supported by the observed rings of whitening on the backside of plaques (Figure 26, right), the severe deformation observed during impact (Figure 26, left), and the major change in force-time curve shape from trials 1 to 2 (Figure 25, left). Furthermore, we posit that lower impact-induced strain rates may reveal quantifiable

differences in AW plaques. Based on the viscoelastic nature of polymeric helmet-grade materials, it is known that the strain response to a stress event is non-linear and rate dependent. Therefore, across a range of testing speeds, or velocities and energies for impact testing, the resulting viscous and/or elastic behavior would vary. This variance in viscoelastic behavior is supported by the significant increases in bulk mechanical performance displayed by Weathered tensile strips under a tensile testing strain rate of 0.1 min^{-1} (testing speed of 5 mm/min). Similarly, the smaller maximum applied forces selected for nanoindentation yielded significant differences in surface mechanical properties, compared to the more aggressive durometer testing that did not reveal significant differences in Shore D hardness. The variation in significant results between impact and tensile testing, along with nanoindentation and durometer testing, serve to exemplify the sensitivity of the helmet-grade material to the rate and degree of deformation during mechanical testing. Thus, future impact testing will aim to reduce impact-induced strain rates by adapting the protocol to elucidate a potential threshold where the altered impact performance of degraded plaques is identified.

Conclusions

The investigation employed 480 hours of AW exposure and quantified the effects upon functional properties of an American football helmet outer shell material. A visual color change was confirmed by significant changes in YI, specifically a yellowing of W_{EXPOSED} and a bleached appearance of W_{BACKSIDE} . A significant change in W_{EXPOSED} and W_{BACKSIDE} areas for alkyl and carbonyl functional groups in ATR-FTIR spectra identified the shift in polymer functional groups and defined chemical property changes. A fluorescence response along the top layer to a depth of approximately 30-35 μm for

W_{EXPOSED} confirmed the creation of AW-induced molecular species, and defined that ~1% of the plaque thickness was degraded. The significant change in PET T_{cc} peak temperature and peak area of MDSC thermograms showcased morphology changes and defined thermal property shifts. For future testing, AW duration will be varied in order to determine the rate and extent of material deterioration, and also to define the profile and concentration of new molecular species created. Further, AW will be compared and correlated to natural outdoor weathering exposure to investigate the effects of on-field degradation.

Mechanical property changes were observed in helmet-grade material at the surface and bulk-level. Nanoindentation quantified significant surface mechanical property changes whereby the decrease in the depth of surface penetration and the increase in the reduced modulus of W_{EXPOSED} suggested an increase in the resistance to deformation. The modified ASTM D638 tensile test protocol quantified significant increases in Young's modulus, yield stress, and UTS of weathered bulk mechanical properties, and showcased that the measured increase in surface-level stiffness led to a significant bulk-level shift in mechanical properties.

The impact performance of an American football helmet outer shell material was analyzed utilizing a novel protocol attempting to employ expected on-field impact conditions. Repetitive linear drop impact testing at 5.5 m/sec significantly degraded the impact performance of the plaque-foam helmet surrogate across each of the five trials. However, a lack of significant differences was found between plaque conditions. Rings of whitening on the backside of impacted plaques and severe plaque deformation during each trial suggested that the impact protocol was potentially too aggressive such that

quantifiable differences between sample groups may have been precluded. We postulate that lower impact-induced strain rates may reveal quantifiable differences in AW plaques based on the viscoelastic nature of polymeric helmet-grade materials as exemplified by the variation in significant results between impact and tensile testing, along with nanoindentation and durometer testing. In order to make confident scientific recommendations towards the effects of AW on impact performance, further protocol development is warranted.

Collectively, this study isolated a material commonly used in American football outer shells and provides a suggested model to further scientific evaluation of protective head gear material. To determine how service life exposures affect impact performance we incorporated a step-wise progression to concurrently quantify and understand changes in material properties at the molecular, microscopic, and bulk levels. Along with AW, measuring effects of additional levels of exposures is necessary to comprehensively understand the cumulative relationship between material aging and degradation, a decrease in impact performance, and the potential increased risk of head injury to the athlete throughout the lifecycle of the outer shell. Ultimately, the ability to identify a battery of diagnostic tools to characterize and evaluate differences in performance versus stages of material degradation throughout the service life of each individual football helmet outer shell could serve to: (i) better educate helmet policies, such as reconditioning procedures (91); (ii) assist to redefine current concepts of shell failure beyond a fracture event or macroscopic flaw, but rather as a decrease in material performance at any size scale and polymeric level, and (iii) to better predict helmet protective capabilities during helmet lifetimes (24).

Supplemental Information

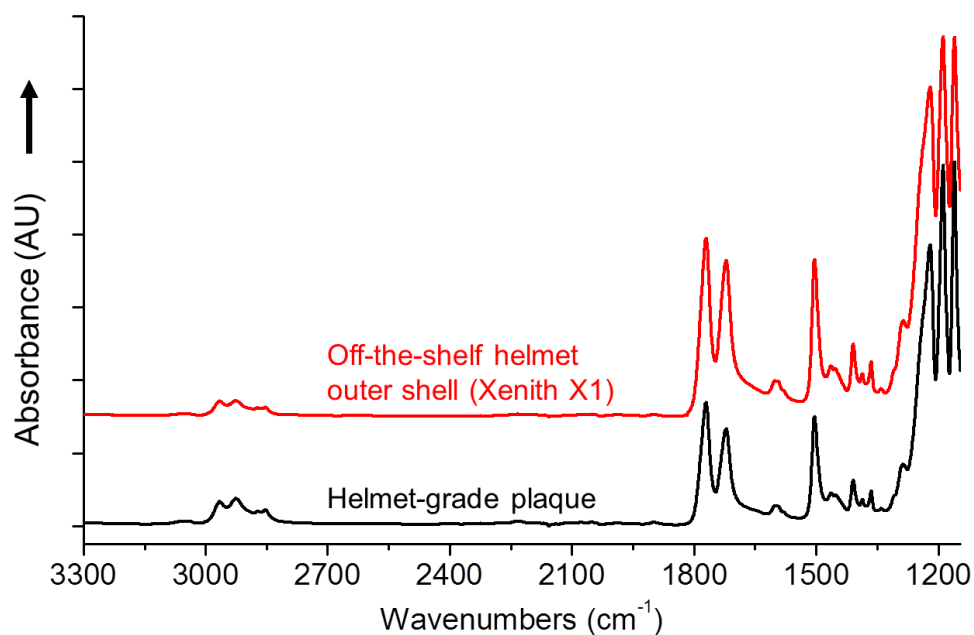


Figure 27. Full ATR-IR spectra between a helmet-grade plaque and an off-the-shelf outer shell (Xenith X1).

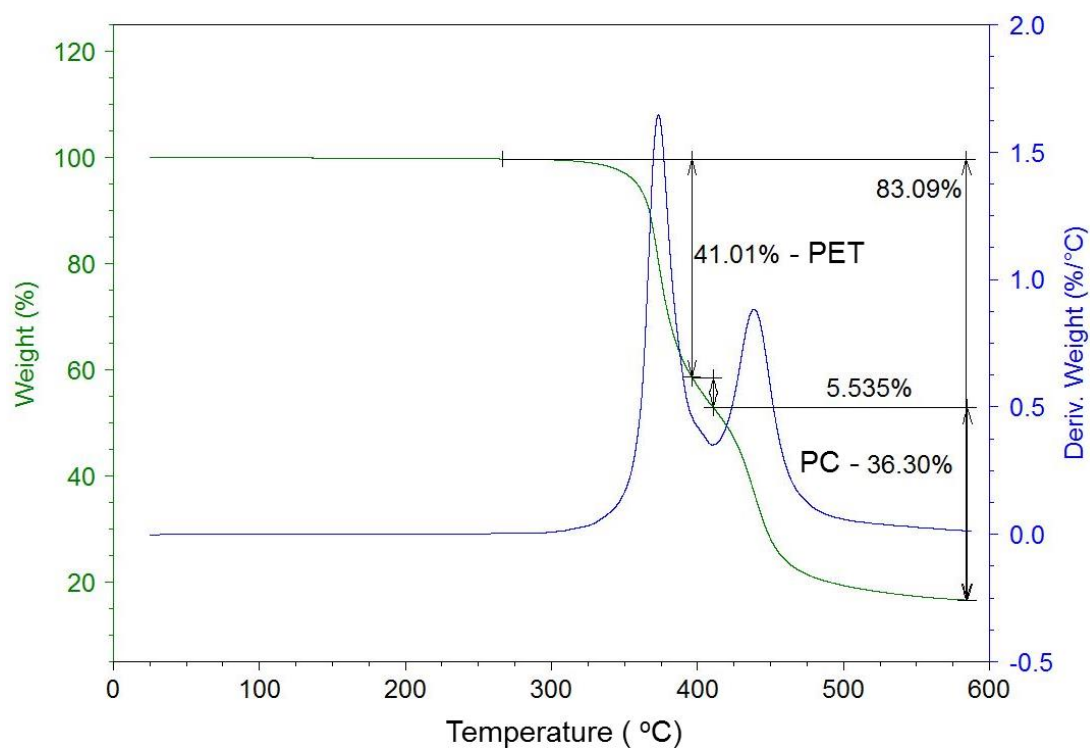


Figure 28. TGA thermogram of a procured pellet at a heating rate of 10 °C/min in air. The blend composition is shown to be approximately equal amounts of PC and PET.

References

- 1 Guskiewicz KM, Bruce SL, Cantu RC, et al. National Athletic Trainers' Association Position Statement: Management of Sport-related Concussion. *J Athl Training* 2004, 39(3): 280-297
- 2 McCrory P, Meeuwisse WH, Aubry M, et al. Consensus statement on concussion in sport: the 4th International Conference on Concussion in Sport held in Zurich, November 2012. *Br J Sports Med* 2013, 47: 250-258
- 3 NOCSAE (ND) 001-11m12. Standard test method and equipment used in evaluating the performance characteristics of protective headgear/equipment. National Operative Committee on Standards for Athletic Equipment 2012
- 4 NOCSAE (ND) 002-11m12. Standard performance specification for newly manufactured football helmets. National Operative Committee on Standards for Athletic Equipment 2012
- 5 ASTM F1446 – 11a. Standard test methods for equipment and procedures used in evaluating the performance characteristics of protective headgear. American Society for Testing and Materials International 2011
- 6 Rowson SR and Duma SM. Brain Injury Prediction: Assessing the combined probability of concussion using linear and rotational head acceleration. *Ann of Biomed Eng* 2013, 41(5): 873-882
- 7 Hoshizaki TB and Brien SE. The science and design of head protection in sports. *J Neurosurgery* 2004, 55(4): 956-967
- 8 Mueller FO. Fatalities from head and cervical spine injuries occurring in tackle football: 50 years' experience. *Clin J Sports Med* 1998, 17(1): 169–182

- 9 Pellman EJ, Viano DC, Casson IR, et al. Concussion in Professional Football: Reconstruction of game impacts and injuries – Part 1. *J Neurosurgery* 2003, 53(4): 799-814
- 10 Guskiewicz KM and Mihalik JP. Biomechanics of sport concussion: Quest for the elusive injury threshold. *Exercise and Sport Sciences Reviews* 2011, 39(1): 4-11
- 11 Caswell SV, Gould TE, and Wiggins JS. Protective Helmets in Sports, Chapter 4 In *Materials in sports equipment*, Vol. 2; Subic A. Ed.; Woodhead: Camdrige, 2007: 87-126
- 12 Viano DC and Halstead D. Change in size and impact performance of football helmets from the 1970s to 2010. *Ann of Biomed Eng* 2012, 40(1): 175-184
- 13 Daneshvar DH, Baugh CM, Nowinski CJ, et al. Helmets and mouth guards: the role of personal equipment in preventing sports-related concussions. *Clin J Sports Med* 2011, 30: 145-163
- 14 Vetter L, Vanderby R, and Broutman LJ. Influence of materials and structure on performance of a football helmet. *Polym Eng Sci* 1987, 27(15): 1113-1120
- 15 Daniel RW, Rowson S, and Duma SM. Head Impact Exposure in Youth Football. *Ann of Biomed Eng* 2012, 40(4): 976-981
- 16 Cobb BR, Urban JE, Davenport EM, et al. Head Impact Exposure in Youth Football: Elementary School ages 9-12 years and the effect of practice structure. *Ann of Biomed Eng* 2013, 41(12): 2464-2473
- 17 Urban JE, Davenport EM, Golman AJ, et al. Head Impact Exposure in youth football: high school ages 14 to 18 years and cumulative impact analysis. *Ann of Biomed Eng* 2013, 41(12): 2474-2487

- 18 Broglio SP, Martini D, Kasper L, et al. Estimation of Head Impact Exposure in High School Football. *Am J Sports Med* 2013, 41(12): 2877-2884
- 19 Schnebel B, Gwin JT, Anderson S, et al. In vivo study of head impacts in football: a comparison of national collegiate athletic association division I versus high school impacts. *J Neurosurgery* 2007, 60(3): 490-496
- 20 Broglio SP, Surma T, and Ashton-Miller JA. High school and collegiate football athlete concussions: biomechanical review. *Ann of Biomed Eng* 2012, 40(1):37-46
- 21 Duma SM, Manoogian SJ, Bussone WR, et al. Analysis of real-time head accelerations in collegiate football players. *Clin J Sport Med* 2005, 15:3–8
- 22 Pellman EJ, Viano DC, Tucker AM, et al. Concussion in Professional Football: Location and Direction of Helmet Impacts. *J Neurosurgery* 2003,53(4):1328-1341
- 23 Broglio SP, Eckner JT, Martini D, et al. Cumulative Head Impact Burden in High School Football. *J Neurotrauma* 2011, 28: 2069-2078
- 24 Fisher E. 10-year helmet reconditioning policy – Press Release. NAERA, 2011
- 25 Wypych G. Handbook of Material Weathering, 4th ed.; ChemTec: Toronto, 2008
- 26 Boyce MC and Haward RN. Chapter 5 In *The Physics of Glassy Polymers*, 2nd ed.; Haward RN, Young RJ, Eds.; Chapman and Hall: London, 1997: 213-293.
- 27 Legrand DG. Mechanical Properties of Polycarbonates, Chapter 6 In *Handbook of Polycarbonate Science and Technology*, 1st ed.; Legrand DG, Bendler JT, Eds.;CRC Press: London, 2000: 213-293.
- 28 Rowson S and Duma SM. Development of the STAR Evaluation System for Football Helmets: Integrating Player Head Impact Exposure and Risk of Concussion. *Ann of Biomed Eng* 2011, 39(8): 2130-40

- 29 Gwin JT, Chu JJ, Diamond SG, et al. An investigation of the NOCSAE linear impactor test method based on in vivo measures of head impact acceleration in American football. *J Biomechanical Eng* 2010, 132(1): 1-8
- 30 Post A, Oeur A, Hoshizaki B, et al. An examination of American football helmets using brain deformation metrics associated with concussion. *Materials & Design* 2013, 45: 653-662
- 31 Jadischke R, Viano DC, Dau N, et al. On the accuracy of the Head Impact Telemetry (HIT) System used in football helmets. *J Biomechanics* 2013, 46: 2310:2315
- 32 Benson BW, McIntosh AS, Maddocks D, et al. What are the most effective risk-reduction strategies in sport concussion? *Br J Sports Med* 2013, 47:321-326
- 33 QUV Lamps. QUV Accelerated Weathering brochure. Q-Lab Corporation 2011.
- 34 ASTM G154 – 04. Standard practice for operating fluorescent light apparatus for UV exposure of nonmetallic materials. American Society for Testing and Materials International 2004.
- 35 ASTM D4587 – 01. Standard practice for Fluorescent UV-Condensation Exposures of Paint and Related Coatings. American Society for Testing and Materials International 2004.
- 36 ASTM D638 – 03. Standard test method for tensile properties of plastics. American Society for Testing and Materials International 2003.
- 37 Spyrou E, Pearsall DJ and Hoshizaki TB. Effect of local shell geometry and material properties on impact attenuation of ice hockey helmets. *Sports Eng* 2000, 3: 25-35

- 38 Krzeminski DE, Rawlins JW, Gould TE, et al. The effect of accelerated outdoor weathering on impact performance of an American football helmet outer shell material. *Procedia Engineering* 2012, 34: 879
- 39 Gimbel G and Hoshizaki TB. A comparison between vinyl nitrile foam and new air chamber technology on attenuating impact energy for ice hockey helmets. *Intl J Sport Sci Eng* 2008, 2(3): 154-161
- 40 Krzeminski DE, Goetz JT, Janisse AP, et al. Investigation of linear impact energy management and product claims of a novel American football helmet liner component. *Sports Technology* 2011, 4(1-2): 65-76
- 41 Gillen KT and Clough RL. Time temperature dose rate superposition: a methodology for extrapolating accelerated radiation aging data to low dose rate conditions. *Polym Degrad Stab* 1989, 24: 137-168
- 42 Diepens M and Gijsman P. Outdoor and accelerated weathering studies of bisphenol A polycarbonate. *Polym Degrad Stab* 2011, 96: 649-652
- 43 Pickett JE and Gardner MM. Reproducibility of Florida weathering data. *Polym Degrad Stab* 2005, 90: 418-430
- 44 Rivaton A, Sallet D, and Lemaire J. The photo-chemistry of bisphenol-a polycarbonate reconsidered: Part 2 – FTIR analysis of the solid-state photo-chemistry in ‘dry’ conditions. *Polym Degrad Stab* 1986, 14: 1-22
- 45 Day M and Wiles DM. Photochemical degradation of poly(ethylene terephthalate). III. Determination of decomposition products and reaction mechanism. *J Appl Polym Sci* 1972, 16: 203-215

- 46 Ram A, Zilber O, and Kenig S. Life expectation of polycarbonate. *Polym Eng Sci* 1985, 25(9): 535-540
- 47 Andradý AL, Searle ND, and Crewdson LFE. Wavelength sensitivity of unstabilized and UV stabilized polycarbonate to solar simulated radiation. *Polym Degrad Stab* 1992, 35: 235-247
- 48 Factor, A. Search for the Sources of Color in Thermally Aged, Weathered and γ -Ray Irradiated Bisphenol A Polycarbonate. *Macromolecular Materials and Engineering* 1995, 232: 27-43
- 49 Tjandraatmadja GF, Burn LS, and Jollands MC. Evaluation of commercial polycarbonate optical properties after QUV-A radiation – the role of humidity in photodegradation. *Polym Degrad Stab* 2002, 78: 435-448
- 50 Pickett JE. Reversible post-exposure yellowing of weathered polymers. *Polym Degrad Stab* 2004, 85: 681-687
- 51 Pickett JE, Gibson DA, and Gardner MM. Effects of irradiation conditions on the weathering of engineering thermoplastics. *Polym Degrad Stab* 2008, 93:1597-606
- 52 Diepens M and Gijsman P. Photodegradation of bisphenol A polycarbonate with different types of stabilizers. *Polym Degrad Stab* 2010, 95: 811-817
- 53 Day M and Wiles DM. Photochemical degradation of poly(ethylene terephthalate). II. Effect of wavelength and environment on the decomposition process. *J Appl Polym Sci* 1972, 16: 191-202
- 54 Grossetete T, Rivaton A, Gardette JL, et al. Photochemical degradation of poly(ethylene terephthalate)-modified copolymer. *Polymer* 2000, 41: 3541-3554

- 55 Fechine GJM, Rabello MS, and Souto-Maior RM. The effect of ultraviolet stabilizers on the photodegradation of poly(ethylene terephthalate). *Polym Degrad Stab* 2002, 75: 153-159
- 56 Fechine GJM, Souto-Maior RM, and Rabello MS. Photodegradation of multilayer films based on PET copolymers. *J Appl Polym Sci* 2007, 104: 51-57
- 57 Lee CO, Chae B, Kim SB, et al. Two-dimensional correlation analysis study of the photo-degradation of poly(ethylene terephthalate) film. *Vibrational Spectroscopy* 2012, 60: 142-145
- 58 Factor A and Chu ML. The role of oxygen in the photo-ageing of bisphenol-a polycarbonate. *Polym Degrad Stab* 1980, 2: 203-223
- 59 Rivaton A. Recent advances in bisphenol-a polycarbonate photodegradation. *Polym Degrad Stab* 1995, 49: 163-179
- 60 Diepens M and Gijsman P. Photodegradation of bisphenol A polycarbonate. *Polym Degrad Stab* 2007, 92: 397-406
- 61 Andrady AL and Searle ND. Photodegradation of rigid PVC formulations. II. Spectral sensitivity to light-induced yellowing by polychromatic light. *J Appl Polym Sci* 1989, 37: 2789-2802
- 62 Rivaton A, Mailhot B, Soulestin J, et al. Comparison of the photochemical and thermal degradation of bisphenol-a polycarbonate and trimethylcyclohexane-polycarbonate. *Polym Degrad Stab* 2002, 75: 17-33
- 63 Edge M, Allen MS, Wiles R, et al. Identification of luminescent species contributing to the yellowing of poly(ethylene terephthalate) on degradation. *Polymer* 1995, 36(2): 227-234

- 64 Edge M, Wiles R, Allen NS, et al. Characterization of the species responsible for yellowing in melt degraded aromatic polyesters – I: yellowing of poly(ethylene terephthalate). *Polym Degrad Stab* 1996, 53: 141-151
- 65 Tarantili PA and Kiose V. Effect of accelerated aging on the structure and properties of monolayer and multilayer packaging films. *J Appl Polym Sci* 2008, 109: 674-682
- 66 Fechine GJM, Rabello MS, Souto Maior RM, et al. Surface characterization of photodegraded poly(ethylene terephthalate). The effect of ultraviolet absorbers. *Polymer* 2004, 45: 230-2308
- 67 Pryde CA and Hellman MY. Solid state hydrolysis of bisphenol-A Polycarbonate. I. Effect of Phenolic End Groups. *J Appl Polym Sci* 1980, 25: 2573-2587
- 68 Sammon C, Yarwood J, and Everall N. An FT-IR study of the effect of hydrolytic degradation on the structure of thin PET films. *Polym Degrad Stab* 2000, 67: 149-158
- 69 Rivaton A, Sallet, and Lemaire J. The photo-chemistry of bisphenol-A polycarbonate reconsidered: Part 3 – influence of water on polycarbonate photo-chemistry. *Polym Degrad Stab* 1986, 14: 23-40
- 70 Hoyle CE, Shah H, and Nelson GL. Photochemistry of bisphenol-A based Polycarbonate: the effect of the matrix and early detection of photo-Fries product formation. *J Polym Sci: Part A* 1992, 30: 1525-1533
- 71 Day M and Wiles DM. Photochemical degradation of poly(ethylene terephthalate). I. Irradiation Experiments with the Xenon and Carbon Arc. *J Appl Polym Sci* 1972, 16: 175-289

- 72 Collin S, Bussiere PO, Therias S, et al. Physiochemical and mechanical impacts of photo-ageing on polycarbonate. *Polym Degrad Stab* 2012, 97: 2284-2293
- 73 Reading M, Elliot D, and Hill VL. New approach to the calorimetric investigations of physical and chemical transitions. *J Thermal Analysis* 1993, 40: 949-955
- 74 Gill PS, Sauerbrunn SR, and Reading M. Modulated Differential Scanning Calorimetry. *J Thermal Analysis* 1993, 40: 931-939
- 75 Wang ZG, Hsiao BS, Sauer BB, et al. The nature of secondary crystallization in poly(ethylene terephthalate). *Polymer* 1999, 40: 4615-4627
- 76 Tant MR and Wilkes GL. Physical Aging studies of poly(ethylene terephthalate). *J Appl Polym Sci* 1981, 26: 2813-2825
- 77 Hutchinson JM, Tong AB, and Jiang Z. Aging of polycarbonate studied by temperature modulated differential scanning calorimetry. *Thermochimica acta* 1999, 335: 27-42
- 78 Schawe J, Riesen R, Widmann J, et al. Information for users of Mettler Toledo thermal analysis systems. TA Instruments. January 2000.
- 79 Fecine GJM, Souto-Maior RM, and Rabello MS. Structural changes during photodegradation of poly(ethylene terephthalate). *J Material Science* 2002, 37: 4979-4984
- 80 Lu X and Hay JN. The effect of physical aging on the rates of cold crystallization of poly(ethylene terephthalate). *Polymer* 2000, 41: 7427-7436
- 81 Wellen RMR and Rabello MS. The kinetics of isothermal cold crystallization and tensile properties of polyethylene terephthalate. *J Material Science* 2005, 40: 6099-6104

- 82 Allen NS, Edge M, Mohammadian M, et al. Hydrolytic degradation of poly(ethylene terephthalate): importance of chain scission versus crystallinity. *Eur Polym J* 1991, 27(12): 1373-1378
- 83 Hutchinson J M. Chapter 3 In *The Physics of Glassy Polymers*, 2nd ed.; Haward RN, Young RJ, Eds.; Chapman and Hall: London, 1997: 85-153.
- 84 Claude B, Gonon L, Duchet J, et al. Surface cross-linking of polycarbonate under irradiation at long wavelengths. *Polym Degrad Stab* 2004, 83:237-240
- 85 Adams MR and Garton A. Surface modification of bisphenol-A-polycarbonate by fav-UV radiation. Part I: In vacuum. *Polym Degrad Stab* 1993, 41:265-273
- 86 Soloukhin VA, Brokken-Zijp JCM, van Asslen OLJ, et al. Physical aging of polycarbonate: Elastic modulus, hardness, creep, endothermic peak, molecular weight distribution, and infrared data. *Macromolecules* 2003, 36: 7587-7597
- 87 Hutchinson JM, Smith S, Horne B, et al. Physical Aging of Polycarbonate: Enthalpy Relaxation, Creep Response, and Yielding Behavior. *Macromolecules* 1999, 32 (15): 5046-5061
- 88 Haward RN and Young RJ. Chapter 1 In *The Physics of Glassy Polymers*, 2nd ed.; Haward RN, Young RJ, Eds.; Chapman and Hall: London, 1997: 85-153
- 89 Ram A, Zilber O, and Kenig S. Residual stresses and toughness of polycarbonate exposed to environmental conditions. *Polym Eng Sci* 1985, 25(9): 577-581
- 90 Sherman ES, Ram A, and Kenig S. Tensile failure of weathered polycarbonate. *Polym Eng Sci* 1982, 22(8): 457-465
- 91 NAERA. www.naera.net. National Athletic Equipment Reconditioning Association

CHAPTER IV

EFFECTS OF SOLVENT EXPOSURE ON MATERIAL PROPERTIES AND IMPACT
PERFORMANCE OF AN AMERICAN FOOTBALL
HELMET OUTER SHELL MATERIAL

Abstract

The pursuit to maintain the initial performance standard of American football helmets has prompted the implementation of a certified reconditioning and recertification process. Thus, the purpose of this study is to (i) develop a method to replicate solvent exposure during the helmet reconditioning painting process, (ii) compare across selected solvent exposure intensities, and (iii) quantify shifts in colorimetric, physical, thermal, mechanical, and impact properties of an American football helmet outer shell material. The Spray (3 coats) condition yielded uniformly exposed plaques and was substantiated for the investigation of solvent effects. Exposures of n-Butyl acetate to the helmet-grade material surface led to shifts in colorimetric, dimensional, thermal, and tensile properties that collectively suggested the occurrence of solvent-induced crystallization (SIC) and environmental stress cracking (ESC). The impact performance of helmet surrogate systems was found perform equivalently using a protocol attempting to employ expected on-field impact conditions. Overall, the results substantiated the spraying method as representative of the reconditioning process and demonstrated shifts in material properties via solvent-induced degradation of helmet-grade outer shell materials.

Introduction

Efforts to mitigate the high prevalence of sports-related concussion in American football (1, 2) include recommended cyclical evaluation of protective head gear and

restorative treatment. The pursuit to maintain the initial performance standard (3, 4) of American football helmets has prompted the implementation of a certified reconditioning and recertification (RR) process (5, 6). Repetitive RR is recommended for athletes (7) and even required to retain the helmet shell warranty (8-11) throughout the lifespan of a helmet to purportedly maintain its service life. However, discontinuity exists between helmet manufacturers (8-12), athletic equipment organizations (13), and state governments (14), regarding the recommended frequency of RR, RR processes, and the maximum allowable lifespan of a helmet outer shell. Scientific research is necessary to establish proper RR guidelines and facilitate improved policy changes.

The RR of American football helmets is overseen by the National Athletic Equipment Reconditioners' Association (NAERA) which is an association of athletic equipment reconditioners and helmet manufacturers licensed by the National Operative Committee on Standards for Athletic Equipment (NOCSAE) to recertify football helmets. Per NAERA, reconditioning is defined as “the inspection, cleaning, repair/restoration of athletic equipment to the original performance standard” (5). Review of publicly available literature describing RR procedures (15-17) combined with anecdotal observations has elucidated that comprehensive standards directing consistent, mandatory RR practices across certified facilities do not currently exist. Furthermore, current reconditioning exposures to helmet outer shells lack peer-reviewed, publicly available scientific data that serve to validate their safe implementation or efficacy.

Helmet reconditioning steps for an outer shell requiring repainting can include: (i) removal of inner liner, facemask, chin strap, hardware, and all stickers and decals (ii) washing with pressurized hot water to perform initial cleaning, (iii) sanding and/or sand

blasting to remove prior paint, as well as smooth out scratches and gouges, (iv) sanitizing with ozone to eliminate the potential for mold and bacteria, and (v) solvent exposure via spray painting, chemical cleaners, and/or application of decals and stickers (5, 15, 16). Upon helmet reassembly, a sample size of the reconditioned full helmet systems must pass the NOCSAE recertification standards before being approved for play (3, 6). A review of the scientific literature for polycarbonate (PC) and polyethylene terephthalate (PET), the primary components in engineered PC blends, reveals that processes mirroring reconditioning steps may serve to accelerate polymer aging and degradation (18).

Exposure of PC and PET to soluble organic solvents is reported to induce crystallinity (19, 20) and crack formation (21) at the microscopic and macroscopic levels, respectively. Known as solvent-induced crystallization (SIC), solvent will diffuse into the material, plasticize and provide mobility to polymer chains, and elicit thermodynamically-favorable rearrangements that alter morphology and molecular packing (19, 20). Expansion of the physical structure due to solvent ingress will serve to reduce the localized glass transition temperature, facilitate conformational chain rearrangements, and promote the growth of crystalline domains. The stresses that arise from SIC and swelling of the polymer system will lead to voids, crazes, and cracks at the material surface, known as environmental stress cracking (ESC) (21). As a result, the solvent-induced nucleation of crazes and propagation of cracks can shift bulk-level mechanical properties and even lead to catastrophic failure. In fact, it has been estimated that failures of plastic materials in commercial use related to ESC is reported between 15-40% (22-24). However, the degradative effects of expected solvent exposures on the functional properties of helmet-grade materials are unknown.

The open scientific literature is devoid of study striving to accurately represent solvent exposures during helmet reconditioning. The subsequent evaluation of functional properties of helmet-grade outer shell materials is further required to establish a relational understanding between varying solvent exposure intensity and changes in impact performance. Such comprehensive investigations could serve to link rates and degrees of material degradation to potentially scientifically and clinically meaningful changes in helmet performance. The research reported herein will explore a baseline of material characterization tests to quantify physical, thermal, and mechanical degradation as a result of laboratory solvent exposure. Therefore, the purpose of this study is to: (i) develop a method to accurately replicate solvent exposure during the reconditioning painting process, (ii) compare selected solvent exposure intensities, and (iii) quantify shifts in colorimetric, physical, thermal, and mechanical, and impact properties of an American football helmet outer shell material.

Experimental

Materials

Helmet-grade PC/PET blended material was procured in pellet form (Makroblend DP UT153, Bayer Corporation) and injection molded following the manufacturer's suggested parameters into 4" x 6" x 1/8" plaques. The chemical composition and thickness of the plaque confirmed to match a current helmet manufacturer's off-the-shelf outer shell (see Chapter III). The solvent utilized in this study was n-Butyl acetate (Reagent Grade, Fisher Scientific). This was selected to match the primary solvent component in coatings formulations currently used to spray paint reconditioned American football helmet outer shells (25).

Solvent (n-Butyl acetate) Exposures

n-Butyl acetate was exposed to plaques via three separate methods - spray coating, surface pooling, and full immersion - to represent an increasing degree of exposure intensity. Plaques (N=25) were randomly assigned into five groups (n=5): (1) Pristine (no solvent exposure), (2) Spray (3 coats), (3) 5 mL Pool, (4) Immerse - 1 hr, and (5) Immerse - 2 hr. The Spray coating of plaques was performed in a ventilated booth using a standard spray gun in an attempt to match expected spray painting conditions during helmet reconditioning practices. The gun nozzle produced a full cone shape and the air pressure was dialed down to produce a solvent mist that evenly covered each plaque surface. The sprayed solvent was observed to evaporate off in ~30 seconds. A total of 3 coats were applied at an interval of one minute. For 5 mL Pool samples, plaques were laid flat in a chemical fume hood and a 5 mL pool of n-Butyl acetate was applied to the entire plaque surface. The solvent was observed to evaporate in ~20 minutes. For Immerse 1 and 2 hr samples, plaques were placed upright in a container of n-Butyl acetate. After immersion, plaques were removed and placed upright in a drying rack in a chemical hood. The solvent evaporated in ~10 minutes. All samples were air dried following exposure for one week to minimize the degree of residual solvent remaining in the helmet-grade plaque material.

Colorimetric, Dimensional, Thermal, and Tensile Property Characterization

Surface color change was quantified via L* whiteness per CIELAB scale using a handheld spectrophotometer (Spectro-guide sphere gloss, BYK Gardner, Columbia, MD). A sheet of white paper was placed underneath the sample during testing to eliminate any variable color effects of the substrate under the plaque.

Dimensional surface changes were observed using an optical microscope (LSM 710, Zeiss, Thornwood, NY) and quantified using AxioVision software (v 4.9.1, Zeiss). For sample preparation, plaques were cross-sectioned with a band saw.

Changes in morphological surface features at the nanoscale were examined using scanning electron microscopy (SEM) (Sigma VP FEG, Zeiss) and analyzed via SmartSEM software (v 5.05 SP 6, Zeiss). The top surface of the plaque was examined and so secondary sample preparation was not required.

Thermal property changes were quantified via modulated differential scanning calorimetry (MDSC) (DSC Q2000, TA Instruments, New Castle, DE) using a 'heat only' modulation protocol with a heating ramp from -50 °C to 300 °C at a rate of 3 °C/min with an amplitude of 0.48 °C every 60 sec. MDSC data was collected and analyzed using Universal Analysis 2000 software (v 4.5A, TA Instruments, New Castle, DE). Samples were acquired using a microtome whereby the slice depth was set and the surface was removed (see MDSC discussion section). The dependent variables examined were MDSC thermogram peak temperatures, peak areas, and step change temperatures.

Tensile mechanical properties were measured via a monotonic pull-to-break test (Insight 10, MTS, Eden Prairie, MN) using a 10 kN (2273 lb) load cell at an initial gauge length of 50 mm with a speed of testing of 5 mm/min (corresponding to a strain rate of 0.1 min⁻¹) (26). Stress-strain data was collected using TestWorks 4 software (v.4.11C, MTS). Modified ASTM D638 Type I tensile specimens (strips: 4" long x 0.5" wide x 0.125" thick) were harvested directly from plaques using a bandsaw (see Figure 34) and edges were hand polished using 240 grit sandpaper. The dependent variables examined were Young's modulus, yield stress, and ultimate tensile stress (UTS).

Linear Drop Impact Testing

Impacts were performed upon a football helmet surrogate plaque-foam system (27) comprised of a plaque stacked atop 25.4 mm thick vinyl nitrile (VN600) foam (Figure 29), using an instrumented drop tower (Dynatup 9250HV, Instron, Norwood, MA) (28). The drop mass assembly of 5.0 kg contained a 44 kN (10,000 lb) load cell tup and a 63.5 mm (2.5") diameter cylindrical rounded nylon dart (Nylon Face, Thor Hammer Company) (29, 30, 50) with a measured Shore 62 D hardness comparable to the helmet-grade plaque (84 D) (27). Plaque-foam systems were impacted at 5.5 m/sec (4, 31) under ambient conditions against a 12.7 mm thick modular elastomer programmer (MEP) pad anvil (3, 31). Impact velocities were measured using an optical velocity flag. Selected trials were captured with a Phantom v5.1 high speed camera at 2100 fps.

Force-time data were collected via Impulse Data Acquisition software (v. 3.2.30, Instron). The voltage signal output produced minor oscillations or “signal ringing” during impact testing. As a result, force data required a Savitzky–Golay (SG) smoothing filter at 101 points of window under a polynomial order of 2, with no boundary conditions. The dependent variable examined was peak force.

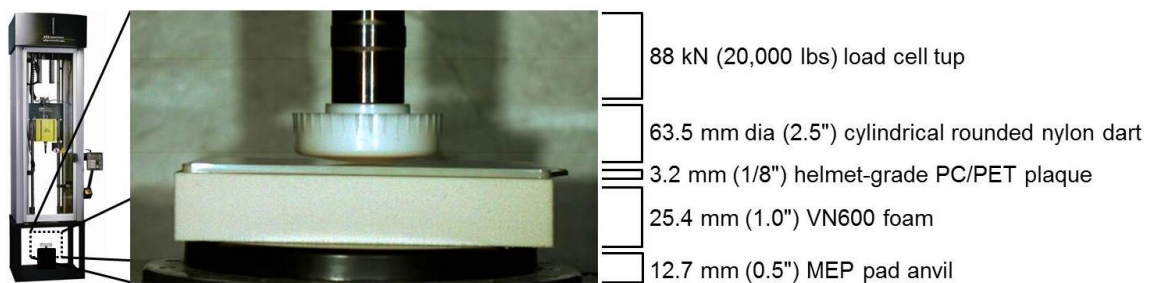


Figure 29. Instron Dynatup 9250 HV instrumented drop tower system shown with a Pristine plaque-foam helmet surrogate system at pre-impact.

Statistical Analysis

Statistical analyses were performed using Statistical Package for Social Sciences software (IBM SPSS, v. 16, IBM Corporation, Sonoma, NY). Several one-way analysis of variance (ANOVA) were performed across solvent exposures (Table 9). Alpha level was set a priori at $\alpha = 0.05$ and effect sizes were calculated using Cohen's f . Post-hoc analyses were performed via Tukey honestly significant difference (HSD) tests.

The independent variables for this study were solvent exposures with five levels: (1) Pristine, (2) Spray (3 coats), (3) 5 mL Pool, (4) Immerse - 1 hr, and (5) Immerse - 2 hr. A summary of statistical analyses performed, independent and dependent variables, and sample sizes across measurement techniques are described in Table 9.

Table 9

Summary of measurement techniques, independent and dependent variables, sample sizes, and statistical analysis performed

Measurement Technique	Independent Variable(s)	Dependent Variable(s)	Sample Size	Statistical Analysis
<u>Colorimetric:</u> CIELAB		(1) L* Value (whiteness)	n=5	one-way ANOVA
<u>Dimensional:</u> Microscopy: Optical, SEM	Solvent (n-Butyl acetate) exposures (5 levels):	(1) thickness of swelling	n=5	none
<u>Thermal:</u> MDSC	(1) Pristine (no solvent) (2) Spray coat (3) 5mL Pool	(1) band peak area (2) band peak temperature	n=3	two one-way ANOVAs
<u>Mechanical:</u> Tensile test	(4) Immerse - 1 hr (5) Immerse - 2 hr	(1) Young's modulus (2) yield stress (3) UTS	n=5	three one-way ANOVAs
<u>Impact:</u> Linear drop impact		(1) peak force	n=5	one-way ANOVA

Results

Results are reported as mean \pm one standard deviation, unless otherwise noted.

Visual Inspection and Colorimetric Characterization

Visual inspection of solvent-exposed plaques (Figure 30) revealed a trend of increased whiteness with increased solvent intensity exposure. The surfaces of Spray and 5 mL Pool appeared hazy with a substantial loss in gloss, while the immersed samples contained a solid, chalky white layer. Colorimetric analysis quantified and confirmed the trend of an increased degree of whiteness, and revealed significant changes in L^* value ($F_{4,20}=672.43$, $p<0.05$, $f=11.91$). Post-hoc analysis revealed L^* differences ($p<0.05$) between all ten combinations (Table 10).

Table 10

L^ whiteness values across solvent exposures*

Solvent Exposure	L^* Value
Pristine	78.8 ± 0.1^1
Spray (3 coats)	80.6 ± 0.6^1
5 mL Pool	82.5 ± 0.5^1
Immerse - 1 hr	88.6 ± 0.7^1
Immerse - 2 hr	91.9 ± 0.4^1

* Matching superscript number denotes the Tukey HSD post-hoc combination was statistically different ($p<0.05$)

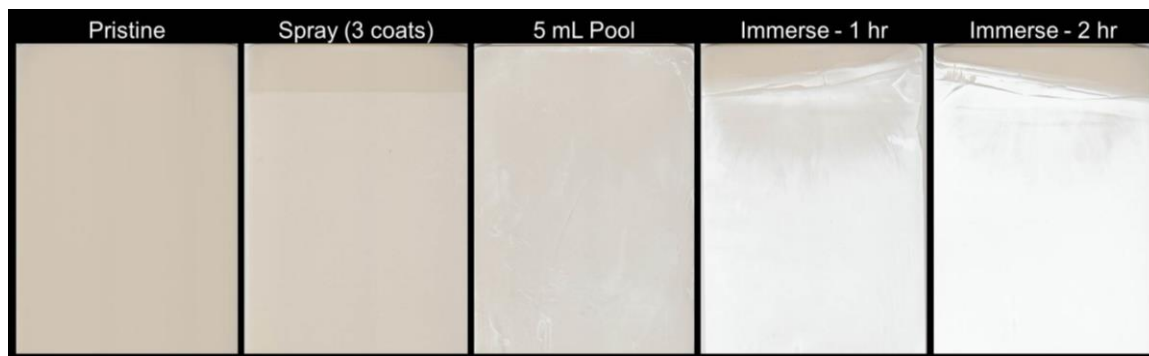


Figure 30. Solvent-exposed plaque surfaces (left-to-right): Pristine, Spray (3 coats), 5 mL Pool, Immerse - 1 hr, and Immerse - 2 hr

Dimensional Surface Characterization – Optical Microscopy

Optical microscopy revealed a well-defined non-solvent/solvent boundary on the helmet-grade plaques exposed to n-Butyl acetate (Figure 31). Swelling of the exposed surface material was observed to increase with increasing solvent exposure intensity and extended to over 40 μm for Immerse - 2 hr (Table 11). The exposed, swelled material was white and appeared to penetrate into the plaque surface beyond the original surface.

Table 11

Thickness of surface swelling across solvent exposures

Solvent Exposure	Thickness of swelling (μm)
Pristine	-
Spray (3 coats)	3.9 ± 0.8
5 mL Pool	22.5 ± 4.3
Immerse - 1 hr	35.4 ± 3.1
Immerse - 2 hr	41.0 ± 2.5

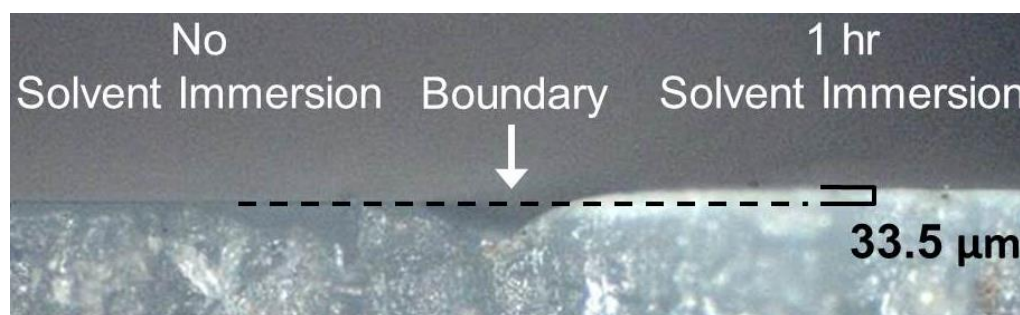


Figure 31. Cross-section of Immerse - 1 hr plaque surface showcasing the non-solvent/solvent boundary and thickness of surface swelling.

Morphological Surface Characterization - SEM

The top surface of Pristine and solvent-exposed samples examined under SEM (Figure 32) exposed nanoscopic differences in the surface morphology. In comparison to Pristine material, the solvent-exposed surfaces were more porous and disordered. The

degree and concentration of surface cavities and voids were observed to increase with increasing solvent exposure intensity.

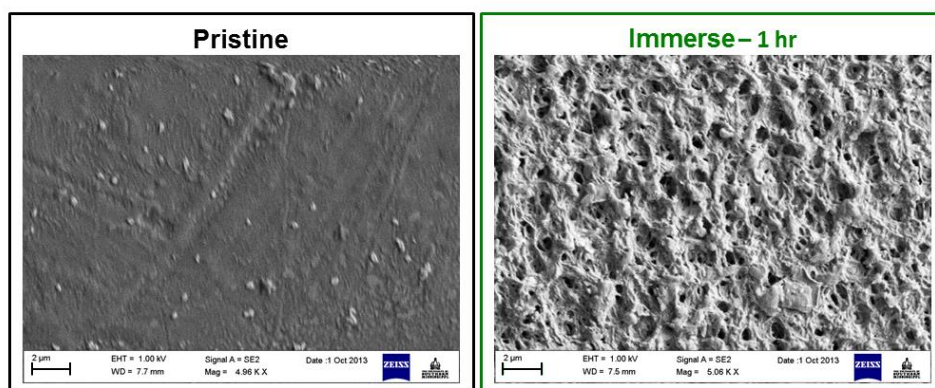


Figure 32. SEM surface images for (left) Pristine and (right) Immerse - 1 hr.

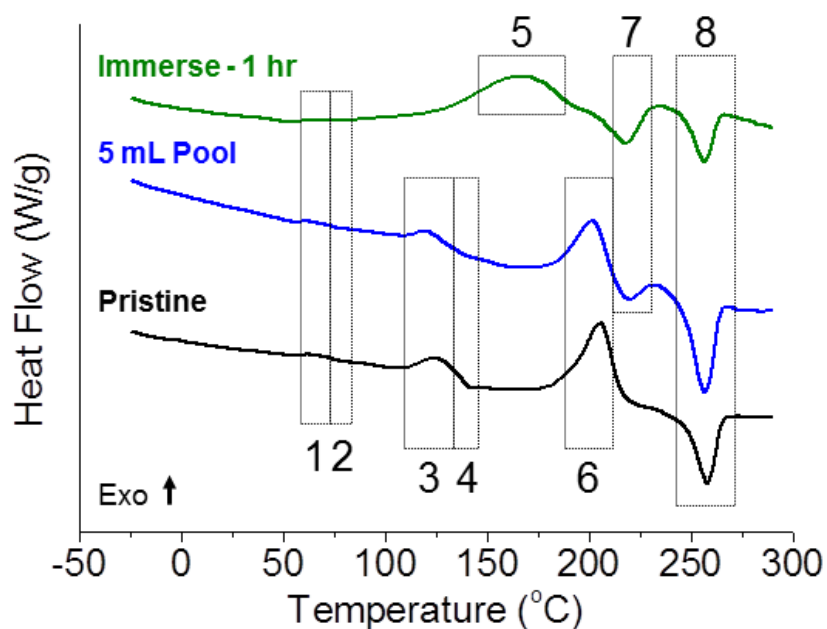


Figure 33. MDSC total heat flow thermograms across the solvent exposures of Pristine, 5mL Pool, and Immerse – 1 hr. Note: General locations of the eight notable bands are highlighted.

Thermal Property Characterization - MDSC

Examination of MDSC total heat flow thermograms across solvent exposure levels revealed several notable bands (Figure 33): (1) exothermic peak around 70 °C, (2) endothermic peak around 80 °C, (3) exothermic peak around 125 °C, (4) endothermic

peak around 140 °C, (5) broad exothermic peak around 170 °C, (6) exothermic peak around 200 °C, (7) endothermic peak around 215 °C, and (8) endothermic peak around 255 °C (Table 12). Analysis revealed (i) a systematic decrease and disappearance in peak temperature and area for band 3 and band 6, (ii) the emergence of a broad band 5, (iii) a systematic emergence and increase in band 7 peak temperature and area, and (iii) no significant differences across solvent exposures for band 8 peak temperature and area

Table 12

MDSC thermogram peak areas and temperatures across solvent exposures

Solvent Exposure	Band 6 Peak Temp (°C)	Band 6 Peak Area (J/g)	Band 7 Peak Temp (°C)	Band 7 Peak Area (J/g)	Band 8 Peak Temp (°C)	Band 8 Peak Area (J/g)
Pristine	206.1 ± 0.5	8.0 ± 1.5	-	-	258.2 ± 0.3	8.3 ± 4.3
Spray (3 coats)	200.9 ± 3.7	4.0 ± 1.4	215.0 ± 1.7	0.9 ± 0.4	258.3 ± 0.7	7.4 ± 2.4
5 mL Pool	195.8 ± 5.1	0.9 ± 0.2	217.2 ± 0.5	6.8 ± 3.3	256.5 ± 1.1	5.8 ± 2.1
Immerse - 1hr	-	-	217.8 ± 0.5	11.4 ± 0.9	257.5 ± 0.7	5.7 ± 3.3
Immerse - 2hr	-	-	218.2 ± 1.0	11.7 ± 4.3	258.5 ± 0.9	7.8 ± 2.6

Tensile Mechanical Property Characterization

The characteristic stress-strain curve shapes across solvent exposures were observed to be equivalent (Figure 34). Analysis revealed yield stress and UTS decreased as solvent intensity increased. Significant differences were observed for yield stress ($F_{4,20}=24.77$, $p<0.05$, $f=2.22$), and UTS ($F_{4,20}=18.96$, $p<0.05$, $f=1.92$). Post-hoc analysis for yield stress and UTS revealed that Pristine, Spray, and 5mL Pool conditions were not different from each other; however, each of the Immerse - 1hr and Immerse 2 - hr conditions were significantly different from all other exposure levels (Table 13).

Table 13

Tensile properties across solvent exposures

Solvent Exposure	Young's modulus (MPa)	yield stress (MPa)	ultimate tensile stress (MPa)
Pristine	1396.1 \pm 24.6	51.0 \pm 0.4 ¹	40.9 \pm 0.4 ⁵
Spray (3 coats)	1383.7 \pm 38.1	50.7 \pm 0.5 ²	40.5 \pm 0.4 ⁶
5 mL Pool	1402.7 \pm 19.1	50.2 \pm 0.6 ³	40.2 \pm 0.7 ⁷
Immerse – 1 hr	1402.5 \pm 29.3	49.2 \pm 0.4 ^{1, 2, 3, 4}	39.0 \pm 0.6 ^{5, 6, 7, 8}
Immerse – 2 hr	1392.2 \pm 24.5	48.3 \pm 0.4 ^{1, 2, 3, 4}	38.1 \pm 0.5 ^{5, 6, 7, 8}

* Matching superscript number denotes the Tukey HSD post-hoc combination was statistically different ($p < 0.05$)

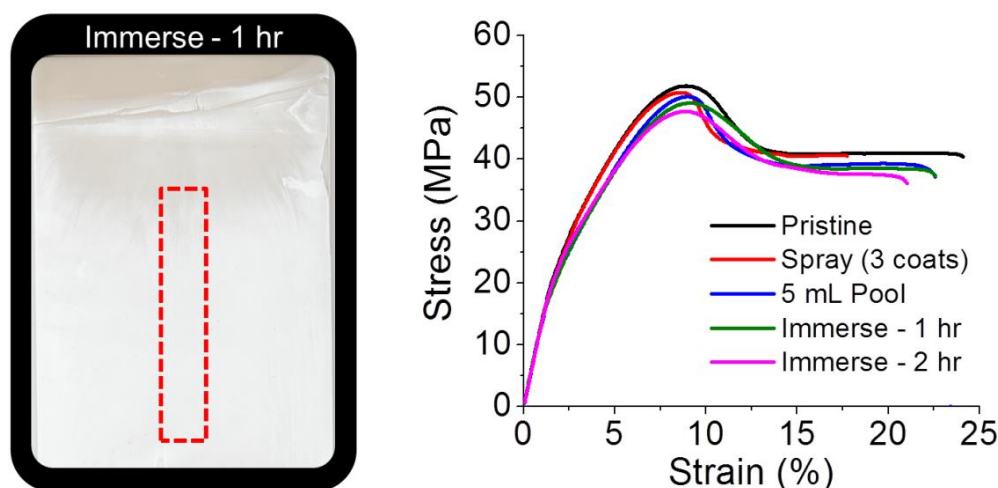


Figure 34. (left) Immerse – 1hr plaque showcasing the location and shape of the harvested tensile specimen. (right) Stress-strain curves across solvent exposures.

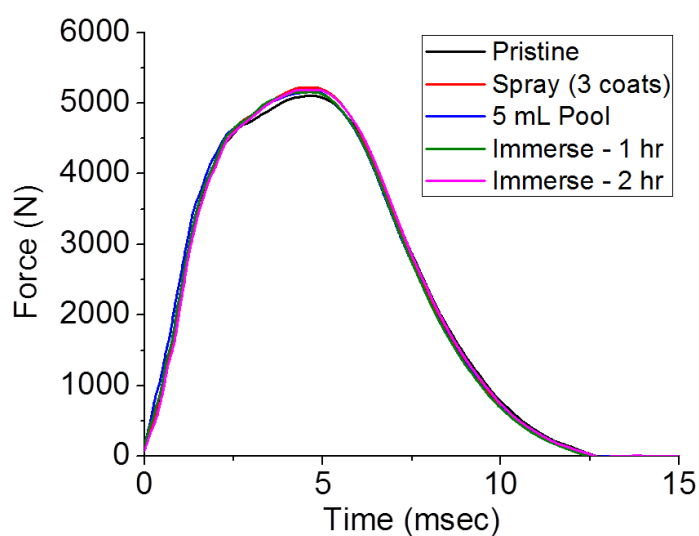
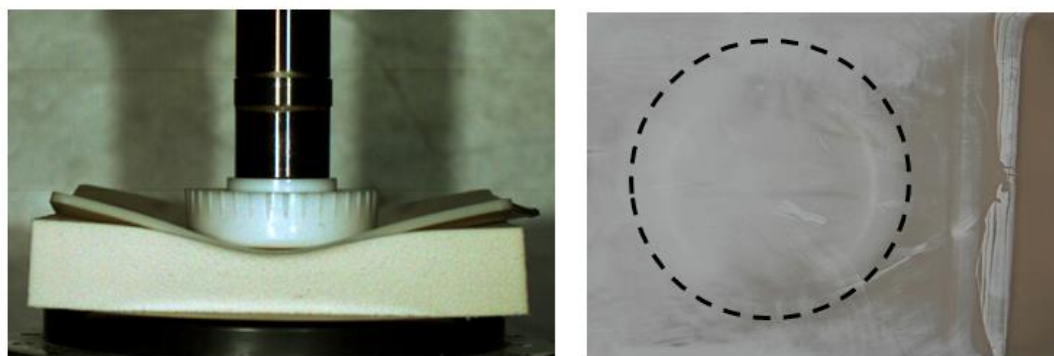
Linear Impact Performance

Equivalent force-time curve shapes were observed for plaque-foam systems (Figure 35) and no significant differences in peak force were found (Table 14). High speed video revealed plaque deformation and VN600 foam compression during impact testing (Figure 36, left), yet each plaque recovered to the original shape. Additionally, the backside of impacted plaques displayed impact-induced rings of whitening that matched the diameter of the nylon drop dart (Figure 36, right).

Table 14

Linear drop test peak force across solvent exposures

Solvent Exposure	Peak Force (N)
Pristine	5221 \pm 68
Spray (3 coats)	5185 \pm 47
5 mL Pool	5147 \pm 38
Immerse – 1 hr	5155 \pm 54
Immerse – 2 hr	5165 \pm 66

*Figure 35. Smoothed force-time curves of plaque-foam systems across solvent exposures.**Figure 36. (left) Maximum deformation of a Pristine plaque-foam system during impact; (right) Backside of Immerse – 1 hr post-impact, highlighting the impact-induced rings of whitening.*

Discussion

The ability to properly assess the effects of solvent exposure on a helmet-grade polymer substrate required the isolated study of a single solvent. The application of a complete off-the-shelf helmet-grade coating formulation to the plaque surface and subsequent non-invasive, non-destructive evaluation of the surface-coating interface is still to be desired. Therefore, n-Butyl acetate was selected because it is the primary solvent component of a commercial coating formulation and it constrained the treatment to a single variable with five levels (Table 9). The parameters for spraying were selected in an attempt to replicate the helmet reconditioning spray painting process. The observed uniform solvent application to the surface substrate, the rapid dry time of 30 seconds, and a uniformly degraded plaque surface (Figure 30) substantiated the spray coating process to properly investigate solvent effects.

Visual and Colorimetric Characterization

Visual whitening and the development of a chalky layer at plaque surfaces was observed with increased solvent exposure intensity (Figure 30). The large effect size for L^* and the significant post-hoc differences observed across all combinations (Table 10) demonstrated that increases in the intensity and duration of solvent exposure induced a considerable shift in whiteness and a substantial change in topographic texture of the helmet-grade material surface.

Investigations of PC (32-34), PET (35), and PC-PET blend (36) systems exposed to soluble organic solvents have been reported to whiten as a result of surface phenomena that serve to scatter light. The creation of cracks, crazes, or voids is reported whereby solvent ingress will cause swelling and plasticization and disrupt the localized

morphology (37). Additionally, the increase in opacity is purported to be due to the initiation or growth of crystal domains (20). Therefore, we postulate that the alterations in morphological surface features served to alter the refractive index of the material and scatter the transmitted light.

Dimensional Surface Characterization - Optical Microscopy

The solvent-induced swelling of PC and PET is reported to initiate at the material surface (32, 33, 38, 39). Thus, optical microscopy of cross-sectioned plaques was used to identify and quantify surface swelling of the helmet-grade plaques. The white layer observed along the surface of solvent exposed plaques supported colorimetric findings and further suggested the disruption of surface morphological features. Microscopy revealed a distinct non-solvent/solvent exposure boundary and facilitated the thickness of surface swelling measurement (Figure 31). Dimensional analysis determined that a systematic increase in the thickness of whitened material developed with increasing n-Butyl acetate exposure intensity (Table 11). Interestingly, the whitened material extended into the bulk material beyond the non-exposed surface, which suggested that the layer of solvent-degraded material is potentially greater than the swelled top surface. As a result, for Immerse - 2hr samples we postulate that the greater than 40 μm thickness of swelling on each of the topside and backside surfaces resulted in solvent-induced degradation of ~3% of the total plaque thickness.

Morphological Surface Characterization - SEM

Changes in surface morphology of solvent exposed systems of PC (34) and PET (20, 40, 41) have been reported using microscopic and nanoscale-level microscopy. The top surface of Immerse – 1 hr under SEM (Figure 32) substantiated the disruption in

surface morphology and provided support for colorimetric and swelling thickness results. The images showcased that solvent exposure induced a high degree of surface cavities and voids. As a result, we postulate that n-Butyl acetate ingress induced plasticization and swelling of the plaque surface, and that the post-exposure drying facilitated solvent evaporation which resulted in (1) a well-developed change in surface porosity and morphology that served to scatter light and increase L^* whiteness, and (2) a distinct layer of white material that quantified the depth of solvent penetration. In other words, if the top surface was examined with excess solvent liquid still present then the surface features would not been observed.

Thermal Property Characterization

Increases in crystallinity using heat capacity measurements are well reported for PC and PET systems exposed to soluble organic solvents (32, 34, 36, 38, 39, 41, 42, 43). Thus, MDSC was selected to examine the presence solvent-induced crystallization in the helmet-grade material. By determining the thickness of swelling using optical microscopy, the whitened material was effectively identified into the solvent-exposed surface. A microtome was used to harvest and isolate the top 5-50 μm (specific to the measured thickness listed in Table 11); however, it is to be noted that potentially all non-degraded material was not fully excluded because it was a manual process.

The morphological complexity of the helmet-grade material was manifested via each of the distinctive bands in the MDSC thermograms (Figure 33), and several heat flow transitions corresponded to transitions previously reported in Chapter III. The band 2 and 4 endotherms that occurred at the glass transition temperature (T_g) of PET and PC, respectively, corresponded to the enthalpy recovery related to effects of physical aging

(27). The band 1 and 3 exotherms that preceded bands 2 and 4, respectively, were representative of pre- T_g artifacts (27). The broad band 5 exotherm observed for each of the Immersion conditions is unreported in the literature. The band 6 exotherm was characteristic of the cold crystallization temperature (T_{cc}) of PET (27, 39, 41, 42). The band 7 endotherm was characteristic to the melting temperature of newly formed solvent-induced PC crystallites (T_{SICm}) (32, 34, 36, 38, 43), which was potentially facilitated by the release of residual solvent bound in T_{SICm} crystallites (44, 45). The band 8 endotherm matched the melting temperature (T_m) of PET crystallites (27, 39, 41).

The concomitant disappearance of the T_{cc} exotherm and emergence of the T_{SICm} endotherm demonstrated a systematic and substantial increase in the degree of PET and PC crystallization, respectively, in the whitened area of the plaque surface. The results supported colorimetric and microscopy findings whereby an increase in crystallization is expected to alter the morphology of solvent-exposed material. Conversely, the lack of significant change in PET T_m peak temperature and area demonstrated that the degree of PET crystallinity was equivalent between plaque conditions upon reaching the ~ 250 °C transition during the heating ramp. We postulate that a change in PET T_m area would require a change in crystallinity potential via an alteration in the degree of polymerization (e.g., chain scission, crosslinking, etc.).

For PET films exposed to acetone, a similar trend in the downward shift and disappearance of the PET T_{cc} exotherm is reported (39, 42). Solvent diffusion into semicrystalline PET is reported to enhance the mobility of chains via the disruption of intermolecular forces, which will facilitate thermodynamically favorable conformational changes that promote crystallization and the ejection of solvent from forming crystallites.

For PC films exposed to acetone, the growth of an endothermic T_{SICm} peak is reported with increased exposure time (43, 38, 44, 45). Solvent uptake by amorphous PC is reported to similarly induce the dissolution of chain segments and promote energetically favorable rearrangements that facilitate crystallization. Interestingly, an exothermic peak representative of secondary crystallization is commonly reported for PET and solvent-exposed PET. However, an associated pre-melting crystallization exotherm is not observed for PC nor solvent-exposed PC; therefore, we postulate that the band 5 is an artifact of the highly disrupted solvent exposed material (46). As a result, we posit that PC SIC does not minimize the energy barrier for thermally-induced PC crystallization. The secondary crystalline rearrangement process is purported to be slower for PC due to the enhanced rigidity afforded by the aromatic rings in the backbone (43). The kinetic difference is showcased by the mismatch in the degree of peak area T_{cc} reduction and T_{SICm} emergence (Table 12) with the minimal exposure condition of Spray (3 coats).

In summary, analysis revealed the emergence of a PC T_{SICm} endotherm without a pre-melting exotherm, along with the disappearance of a PET T_{cc} exotherm with a steady PET T_m endotherm. We postulate that solvent uptake facilitated the initiation and progression of PET cold crystallization and PC SIC of the surface material, but further investigation would be required with additional techniques, such as thermogravimetric analysis, to determine the residual solvent content post-drying and the degree of solvent released during PC and PET crystallization.

Tensile Mechanical Property Characterization

Tensile mechanical properties between solvent exposure conditions were quantified using a modified ASTM-D638 monotonic tensile test protocol. The speed of

testing (5 mm/min), strain rate (0.1 min^{-1}), the use of sand paper for final sample preparation, and width of the specimen narrow section matched D638 setup conditions (26). Modified Type I specimens were harvested directly from plaques using a band saw (Figure 34, left). The edges were manually sanded to eliminate flash and burrs prior to testing; however, it is noted that the inability to precisely obtain a blemish-free finish resulted in stress-concentrating defects present along the sample surface. As a result, strain at break was highly variable (Figure 34, right) and was not reported.

The large effect sizes and for yield stress and UTS (Table 13) demonstrated that n-Butyl acetate induced significant shifts in mechanical properties. The systematic tensile property decreases corresponded to the systematic increases in L^* whiteness and swelling thickness, as well as the concomitant T_{cc} and T_{SICm} behavior. The significant post-hoc decreases for immersed sample conditions supported previous studies that demonstrated solvent exposure reduced the stress to initiate the onset of bulk-level plastic deformation (37, 47) and reduced the stress required during the post-yield drawing phase (48). The molecular-level disruption of intermolecular forces due to solvent uptake is reported to extract low molecular weight polymer which decreases the density of molecular packing and chain entanglement concentration (37). The coalescence of these morphological changes at the microscopic level can further induce the formation of surface cracks, known as environmental stress cracking (ESC). The reduction in macroscopic mechanical performance due to ESC is well reported in the scientific literature for PC and PET systems (21). Overall, the Immerse - 2hr results suggest that the ~3% thickness postulated to be solvent-degraded led to a 5% decrease in yield stress and a 7% decrease in UTS. In summary, we postulate that the systematic reductions in

yield stress and UTS were induced by reductions in the density of chain packing and entanglements. Further investigation would be required with chromatographic and rheological techniques to determine the profile of low molecular weight mass loss and the degree of changes in network entanglement, respectively.

Linear Impact Performance

The impact performance of solvent-exposed helmet surrogate plaque-foam systems was analyzed using a protocol attempting to employ expected on-field impact conditions (Figure 29). Selected input parameters were adjusted from previous setups with the goal towards the reduction of impact-induced strain rates (27; 48). The impact mass was reduced due to the drop dart iteration, but still remained within established helmet testing standards (3). The drop dart geometry and material (29, 30, 50) as well as the MEP Pad anvil (3, 31) progressed to better match peer-reviewed setups and testing standards. Yet, the impact velocity remained constant to match established helmet testing standards (4, 31).

Equivalent force-time curve shapes (Figure 35) and the absence of significant differences in peak force (Table 14) revealed that helmet surrogate systems across solvent exposure levels responded similarly. Interestingly, solvent-exposed systems were visually observed to produce lower mean peak forces; however, further investigation including the effect of repetitive drop impacts is required to confidently elucidate the potential shift in impact properties.

Linear drop impact results suggest that the solvent exposure did not alter the impact performance. However, potential factors are postulated to cause the lack of significant differences: (i) with only ~3% of the plaque thickness posited to be solvent-

degraded, the remaining bulk material potentially had sufficient retention of impact performance properties to compensate for the surface-level deterioration, (ii) the adjusted impact protocol produced strain rates that remained potentially too aggressive, such that quantifiable differences between solvent exposure conditions may have been precluded. This is supported by the observed level of deformation during impact (Figure 36, left) and the rings of whitening on the backside of impacted plaques (Figure 36, right). As discussed previously in Chapter III, lower impact-induced strain rates will potentially reveal quantifiable differences of solvent-exposed material, as reductions in bulk mechanical performance were elucidated herein via modified ASTM D638 tensile testing at 0.1 min^{-1} . Therefore, future testing will aim to (1) perform repetitive drop impacts and (2) further reduce impact-induced strain rates by further adapting the impact protocol to elucidate a potential threshold where the altered impact performance of solvent-degraded plaques is identified.

Conclusions

The investigation increased exposure levels of n-Butyl acetate and quantified the effects upon functional properties of an American outer shell material. n-Butyl acetate is the primary solvent component of a commercial coating used to repaint American football helmets during certified reconditioning. The uniform solvent application and observed dry time substantiated the Spray (3 coats) method as representative of the reconditioning spray painting process.

Overall, increased exposure intensities of n-Butyl acetate led to increased effects to functional properties. The systematic increase in L^* whiteness confirmed the visual color change, and correlated with higher degrees of surface porosity that were postulated

to scatter light and induce the observed whitening. The systematic increase in thickness of surface swelling corresponded to the increased disruption in surface morphology observed under SEM and defined that up to ~3% of the plaque thickness was solvent-degraded. The concomitant disappearance of the T_{cc} exotherm and emergence of the T_{SICm} endotherm suggested a systematic and substantial increase in the degree of PET cold crystallization and PC SIC, respectively, in the whitened area of the plaque surface. The modified ASTM-D638 tensile test protocol quantified significant decreases in yield stress and UTS, and suggested a decrease in the density of molecular packing and chain entanglement concentration, respectively. Significant changes in impact performance were not observed; however, future work will continue to adapt the impact protocol and employ repetitive impacts to elucidate potential threshold where the altered impact performance of degraded plaques is identified

Overall, this study served as a first step to determine the changes in helmet-grade materials induced by expected exposures as a result of helmet reconditioning. We incorporated a step-wise progression to concurrently quantify and understand solvent-induced changes in material properties at the nanoscopic, microscopic, and bulk levels. The execution of additional techniques is recommended to fully discern changes in thermal and physical properties to ultimately provide a comprehensive battery of diagnostic tools to characterize and evaluate (i) differences in performance versus stages of material degradation throughout the lifespan of outer shell materials, (ii) exposures to equivalent off-the-shelf solvent cocktails, and (iii) full helmet outer shells under end-use conditions.

References

- 1 Baugh CM, Kiernan PT, Kroshus E, et al. Frequency of head impact related outcomes by position in NCAA Division I collegiate football players. *J Neurotrauma* 2015, 32(5): 314-326
- 2 Rosenthal JA, Foraker RE, Collins CL, et al. National high school concussion rates from 2005-2006 to 2011-2012. *Am J SportsMed* 2014, 42(7): 1710-1715
- 3 NOCSAE 001-13m14b. Standard test method and equipment used in evaluating the performance characteristics of protective headgear/equipment. National Operative Committee on Standards for Athletic Equipment 2013
- 4 NOCSAE 002-13m13. Standard performance specification for newly manufactured football helmets. National Operative Committee on Standards for Athletic Equipment 2013
- 5 NAERA Reconditioning and Recertification. www.naera.org. National Athletic Equipment Reconditioners' Association 2014
- 6 NOCSAE 004-11m14. Standard performance specification for recertified football helmets. National Operative Committee Standards for Athletic Equipment 2014
- 7 Rausch, R., Fields, K., 2011. February 4 – Newsletter. NOCSAE Organization.
- 8 Riddell 360 Fitting Instructions and Helmet Care – Helmet Warranties, 2011.
- 9 Schutt Helmet Fitting Instructions. 2011. Schutt Sports, Inc.
- 10 Xenith X2E Helmet Fitting Instructions. 2013. Xenith, LLC.
- 11 Xenith EPIC Helmet Fitting Instructions. 2013. Xenith, LLC
- 12 Rawlings Warranty Information. 2013. Rawlings Sports Goods, Inc.
- 13 Fisher E. 10-year helmet reconditioning policy. NAERA, 2011

- 14 Texas Education Code-Sect: 33.094, 2011. Football Helmet Safety Requirements
- 15 Schutt Reconditioning Quick Hits brochure, 2012. Schutt Sports, Inc.
- 16 Riddell Football Catalogue - Reconditioning, 2014. Riddell, Inc.
- 17 Xenith Reconditioning. www.xenith.com [visited October 2014]. Xenith, LLC.
- 18 Wypych G. Handbook of Material Weathering, 4th ed.; ChemTec: Toronto, 2008
- 19 Mercier JP, Groeninckx G, and Lesne M. Some aspects of vapor-induced crystallization of polycarbonate of bisphenol A. *J Polymer Science Part C: Polymer Symposia* 1967, 16(4): 2059-2067
- 20 Desai AB and Wilkes GL. Solvent-induced crystallization of polyethylene terephthalate. *J Polymer Science: Polymer Symposia* 1974, 46(1):291-319
- 21 Robeson, LM. Environmental stress cracking: A review. *Polym Eng Sci* 2013, 53(3): 453-467
- 22 Arnold JC. Environmental stress-crack initiation in glassy polymers. *Trends in Polymer Science* 1996, 4: 403-408
- 23 Wright DC. Environmental stress cracking of plastics. RAPRA Publish:UK, 1996.
- 24 Jansen JA. Environmental stress cracking – the plastic killer. *Advances and Material Processes* 2004, 162(6): 50-53
- 25 Akzo Nobel C3.8 High Solids Poly Blender – Material Safety Data Sheet, 2011. Akzo Nobel Coatings, Inc.
- 26 ASTM D638 – 03. Standard test method for tensile properties of plastics. American Society for Testing and Materials International 2003.
- 27 Krzeminski DE, Fernando BMD, Rawlins JW, et al. Quantifying the effects of accelerated weathering and linear drop impact exposures of an American football

- helmet outer shell material. *Proc IMechE Part P: J Sports Engineering and Technology* 2014, 228(3): 171-187
- 28 Krzeminski DE, Goetz JT, Janisse AP, et al. Investigation of linear impact energy management and product claims of a novel American football helmet liner component. *Sports Technology* 2011, 4(1-2): 65-76
 - 29 NOCSAE ND081-14. Standard pneumatic ram test method and equipment used in evaluating the performance characteristics of protective headgear and face guards. National Operative Committee on Standards for Athletic Equipment 2014
 - 30 Post A, Oeur A, Hoshizaki TB, et al. An examination of American football helmets using brain deformation metrics associated with concussion. *Materials & Design* 2013, 45: 653-662
 - 31 ASTM F1446 – 13. Standard test methods for equipment and procedures used in evaluating the performance characteristics of protective headgear. American Society for Testing and Materials International 2013
 - 32 Kambour RP, Karasz FE, and Daane, JH. Kinetic and equilibrium phenomena in the system: acetone vapor and polycarbonate film. *J Polymer Science Part A-2: Polymer Physics* 1966, 4(3): 327--347
 - 33 Kambour RP, Gruner CL, and Romagosa EE. Biphenol-A polycarbonate immersed in organic media. Swelling and response to stress. *Macromolecules* 1974 7(2): 248-253
 - 34 Sung NH, Gahan RE, and Haven RE. Studies on whitening phenomena induced by some non-solvents on highly oriented glassy polymers. *Polym Eng Sci* 1983 23(6): 328-336

- 35 Yeh GSY and Giel PH. Crystallization of polyethylene terephthalate from the glassy amorphous state. *J Macromolecular Science, Part B: Physics* 1967, 1(2): 235-249
- 36 Kambour RP, Chu C, and Avakian RW. Crystallizing crazes: The probable source of solvent stress cracking resistance in a polyester/polycarbonate blend. *J Polymer Science Part B: Polymer Physics* 1986 24(9): 2135-2144.
- 37 Miller GW, Visser SAD, and Morecroft AS. On the solvent stress-cracking of polycarbonate. *Polym Eng Sci* 1971, 11:73-81
- 38 Ouyang H, Wu MT, and Ouyang W. The study of mass transport of acetone in polycarbonate. *J Applied Physics* 2004, 96(12), 7066-7070
- 39 Ouyang H, Lee WH, Ouyang W, et al. Solvent-Induced Crystallization in Poly(ethylene terephthalate) during Mass Transport: Mechanism and Boundary Conditions. *Macromolecules* 2004, 37, 7719-7723
- 40 Makarewicz PJ and Wilkes GL. Diffusion studies of Poly(ethylene terephthalate) crystallized by nonreactive liquids and vapors. *J Polymer Science: Polymer Physics* 1978, 16: 1529-1544
- 41 Jameel H, Noether HD, and Rebenfield L. The effects of orientation and crystallinity on the solvent-induced crystallization of Poly(ethylene terephthalate). II. Physical Structure and Morphology. *J Applied Polymer Science* 1982, 27:773
- 42 Ouyang H, Chen CC, Lee S, et al. Acetone transport in Poly(ethylene terephthalate) and related phenomena. *J Macromolecular Science, Part B: Physics* 1998, 36: 163-169

- 43 Mendez G and Muller AJ. Evidences of the crystalline memory and recrystallisation capacity of bisphenol-A polycarbonate. *J Thermal Analysis and Calorimetry* 1997 50(4): 593-602.
- 44 Fan Z, Shu C, Yu Y, et al. Vapor-induced crystallization behavior of bisphenol-a polycarbonate. *Polym Eng Sci* 2006, 26(6): 729-734
- 45 de Oliveira FLBO, Leite MCAM, Couto LO, et al. Study on bisphenol-A polycarbonates samples crystallized by acetone vapor induction. *Polymer bulletin* 2011 67(6): 1045-1057
- 46 Schawe J, Riesen R, Widmann J, et al. Information for users of Mettler Toledo thermal analysis systems. TA Instruments. January 2000
- 47 Ivanova NI and Pertsov NV. Effect of strain rate on the nature of the change in mechanical properties of polyethylene terephthalate in active liquid media. *Materials Science* 1978 14(2): 168-170
- 48 Al-Saidi LF, Mortensen K, and Almdal K. Environmental stress cracking resistance. Behavior of polycarbonate in chemicals by determination of the time-dependence of stress at constant strains. *Polym Deg Stab* 2003, 82: 451-461
- 49 Krzeminski DE, Lippa NM, Rawlins JW, et al. Evaluation of supplemental football helmet protection. *J Athl Training* 2013, 48(3): S-190
- 50 Post A, Oeur A, Hoshizaki TB, et al. Differences in region-specific brain tissue stress due to impact velocity for simulated American football impacts. *Proc IMechE Part P: J Sports Engineering and Technology* 2014, 228(4): 276-286

CHAPTER V

CHARACTERIZATION OF REPETITIVE LINEAR IMPACT EXPOSURE AND
IMPACT-INDUCED STRESS-WHITENING OF AN AMERICAN FOOTBALL
HELMET OUTER SHELL MATERIAL

Abstract

Mechanical stress exerted upon impact-modified thermoplastic blends will generate microscopic voids via rubber-toughener (RT) particle cavitation which will macroscopically manifest to visibly whiten the material. Pilot work has elucidated whitening in collegiate American football helmet outer shells after a single season and linear impact testing of helmet surrogates has elicited rings of stress-whitening in helmet-grade plaques. The purpose of this study was to investigate the effects of repetitive linear drop exposures and impact-induced stress-whitening on the (i) impact performance; (ii) colorimetric, physical, and thermal properties; and (iii) surface and tensile mechanical properties of an American football helmet outer shell material. Statistically significant changes in plaque impact performance corresponded to substantial stress-whitening that penetrated up to 40-45% into the thickness and elicited significant shifts in surface and tensile mechanical properties. Nanoscale microscopy suggested elongation of the matrix and delamination at the matrix-RT interface. Thermal property analysis suggested the concomitant occurrence of RT cavitation and strain-induced crystallization. To our knowledge, this is the first time surface and tensile mechanical properties of a non-fractured, stress-whitened rubber-toughened material have been reported. We postulate voids generated via rubber particle cavitation led to delamination at the RT-matrix interface and visible stress-whitening. Results identified a battery of diagnostic tools to

characterize material property changes for impact-induced degradation of rubber-toughened outer shell materials.

Introduction

Protective head gear comprise two main protective components, the outer shell and the inner liner, whereby the shell is reported to absorb between 10 to 40% of the total impact energy delivered (1-4). The outer shell component of modern American football helmet systems are commonly constructed of injection-molded engineered polycarbonate (PC) blends impact-modified with rubber particles to promote enhanced toughness properties (5). The ability of helmet-grade PC to maintain the required protective performance towards the prevention of sports-related head injury is affected by expected end-use conditions (6). Throughout each season and across the lifespan of the helmet, exposure to cyclic environmental exposures and repetitive impact events serve to degrade material properties. In fact, the known reduction in protective capacity of the American football helmet system has led to age limits for the outer shell established independently by athletic equipment association policies (7), helmet manufacturer warranties (8-12), and state government laws (13). However, variations in outer shell lifetimes exist across organizations and a review of the open literature does not substantiate each prescribed age limit. The current disparity in guidelines demands scientific understanding towards the degree and rate of impact performance changes of American football helmet components and materials throughout service lifetimes.

The myriad of on-field impact scenarios is extensive with attenuation often initiated by the outer shell (14). Factors reported to influence the magnitude of impact events include the position on the field (15, 16), the level of play (16-20) and the type of

impact (21), such as helmet-to-helmet or helmet-to-ground. The cumulative effect of such exposures will serve to fatigue the outer shell material and incrementally modify the localized loading rates and strain rates exhibited during subsequent events. The number of impacts to a single shell has been reported to reach above 2200 in one season (22); however, the total number of on-field impacts throughout the lifespan was not found in the open literature. Furthermore, the comprehensive history of all mechanical stress placed on the shell both on and off the field is unknown. As a result, each helmet outer shell has endured a distribution of impact events across varying severity levels with an unknown threshold towards the potential for reduced impact performance.

Mechanical stress exerted upon thermoplastic rubber-toughener (RT) blends will generate microscopic voids via rubber particle cavitation which will macroscopically manifest to visibly whiten the material (5). The cavitation event can result in a void in the rubber particle or delamination at the RT-matrix interface, thereby relieving the local hydrostatic stress state in the matrix material (23-26). Commonly known as stress-whitening, the scattering of visible light is caused by a localized change in the material refractive index due to the development of internal void arrays or clusters on the size scale equivalent to the wavelength of light (27, 28). Pilot work has elucidated whitening in collegiate American football helmet outer shells after a single season of normal use (29) (Figure 37) and rings of stress-whitening have been reported for helmet-grade plaques following linear impact testing of helmet surrogates (30-32).

Stress-whitening is widely reported for rubber-toughened blends that undergo fracture or irreversible plastic deformation modes. However, as previously described (30), such testing appears to have minimal value toward improving the understanding of

impact characteristics of helmet-grade materials under end-use conditions. Further, helmet outer shells are reused without a publicly available technical understanding between repetitive impact exposure inducing aesthetically unfavorable whitening and subsequent changes in impact performance. As a result, a bridge of knowledge detailing property changes between pristine and stress-whitened material prior to catastrophic failure does not exist.

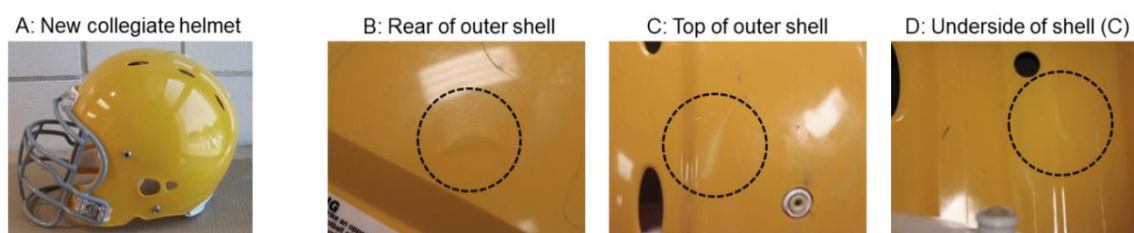


Figure 37. (A) Example of new collegiate American football helmet. (B and C) Areas of whitening were visually observed (circled) across the outside of helmet shells after one season of use. (D) Whitening was observed to transfer through to inside of the outer shell.

The scientific literature is replete with the characterization of RT blends with PC and polyethylene terephthalate (PET). Yet the same material systems lack comprehensive analysis that defines changes in material properties following mechanically-induced stress-whitening. Rather, the majority of experimental investigations on mechanically deformed, stress-whitened RT-PC and RT-PET blends report structural changes using microscopy techniques (28, 33-38). Only a single study of stress-whitened RT-PET was found whereby material properties changes were explored with dynamic mechanical analysis (37). Surprisingly, the majority of analyses are devoid of assessments of chemical, physical, thermal, and mechanical property changes. Scientific study striving to accurately represent on-field impact exposures and the subsequent evaluation of functional properties of helmet-grade outer shell materials is therefore warranted. Furthermore, a validated set of diagnostic tests could provide a

toolbox of analytical techniques to link rates and degrees of material degradation to scientifically meaningful changes in helmet performance. As a result, the research reported herein will explore a baseline of material characterization tests to quantify physical, thermal, and mechanical degradation as a result laboratory impact exposure. The purpose of this study was to investigate the effects of repetitive linear drop impact exposures on the (i) impact performance; (ii) colorimetric, physical, and thermal properties; and (iii) surface and bulk (tensile) mechanical properties of an American football helmet outer shell material.

Experimental

Materials

Helmet-grade PC/PET blend material, impact-modified with acrylonitrile-butadiene-styrene terpolymer rubber-toughener (ABS-RT), was procured in pellet form (loading level of ABS-RT not provided) and injection molded into 4" x 6" x 1/8" plaques. The bulk density of the injection-molded plaque was confirmed to match a current off-the-shelf outer shell (1.201 ± 0.006). The plaque thickness and chemical composition was selected to match a football helmet outer shell (see Chapter III). Additional material and molding process details have been previously described (see Chapter III).

Linear Drop Impact Testing

Plaques (n=20) were randomly selected and split into two groups: Non-impacted and Impacted. Each Impacted plaque (n=10) underwent an impact treatment of 12 repetitive impact trials at an interval of 75 ± 15 sec (39, 40). Linear drop impact tests were performed upon a football helmet surrogate plaque-foam system (30) (Figure 38) comprised of a plaque stacked atop 25.4 mm thick VN600 foam (31, 32). After an initial

impact to quantify the performance of a Non-impacted plaque (trial 1), an impact treatment of ten repetitive trials was performed (trials 2-11) followed by a final impact (trial 12). A new piece of VN600 foam was used for impact trial 12. A total of 120 impact trials were conducted.

Impact testing was performed using an instrumented drop tower system (Dynatup 9250HV, Instron, Norwood, MA). The drop mass assembly of 5.0 kg contained a 44 kN (10,000 lb) load cell tup and a 63.5 mm (2.5") cylindrical rounded polyurethane drop dart (250H, Lixie Hammers, Central Falls, RI) (41) with a measured Shore 72 D hardness (see section 2.5) comparable to the helmet-grade plaque (84 D). Plaque-foam systems were impacted at 5.5 m/sec (39, 42) under ambient conditions against a 25.4 mm modular elastomer programmer (MEP) pad anvil (42) (Cadex Inc., St-Jean-sur-Richelieu, Quebec). Impact velocities were measured using an optical velocity flag. Selected trials were captured with a Phantom v5.1 (Vision Research, INC., Wayne, NJ) color high speed video camera at 2100 frames per second. Force-time data were collected via Impulse Data software (v. 3.2.30, Instron). Force data required a Savitzky–Golay (SG) smoothing filter at 501 points of window under polynomial order of 2 with no boundary conditions. Dependent variables examined were peak force and time to peak force.

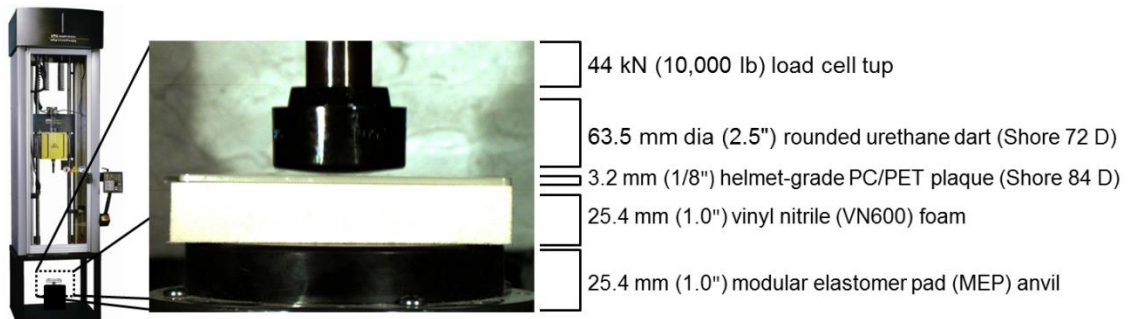


Figure 38. Instron Dynatup 9250 HV instrumented drop tower system shown with a football helmet surrogate plaque-foam system at pre-impact.

Physical Property Characterization

Surface color change was quantified via L* whiteness per CIELAB scale using a handheld spectrophotometer (Spectro-guide sphere gloss, BYK Gardner, Columbia, MD). A sheet of white paper was placed underneath the sample during testing to eliminate any variable color effects of the substrate under the plaque.

Cross-sectional changes in the plaque were examined using optical microscopy (VHX-600, Keyence Corporation, Elmwood Park, NJ) and the depth of whitening was measured using XY software (VHX-H1MK, Keyence Corporation). Rectangular strips (30 mm long x 3 mm wide x 3.2 mm thick) were harvested from plaques (see Figure 41) using a bandsaw and the specimen edges were hand polished using 240 grit sandpaper.

Changes in morphological features at the nanoscale were examined using scanning electron microscopy (SEM) (Sigma VP FEG, Zeiss, Thornwood, NY) and analyzed via SmartSEM software (v 5.05 SP 6, Zeiss). Samples for analysis were submersed in liquid nitrogen for 15 minutes and fractured manually with a hammer. Exposed fracture surfaces were sputter-coated with ~5 nm layer of silver.

Bulk density was measured via hydrostatic weighing using an analytical balance (XS104, Mettler-Toledo International Inc., Columbus, OH) equipped with a density determination kit using deionized water as the immersion fluid (43). Cylindrical shaped specimens (5.9 mm dia x 3.2 mm thick) were harvested from plaques (see Figure 48) using a drill press with a customized core drill (6 mm inner diameter). For Impacted samples, whitened material was isolated by manually removing the top ~1.4 mm of non-whitened material with a grinding wheel (EcoMet 3, Buehler, Lake Bluff, IL) using 120 grit sand paper. Non-impacted specimens also had the top ~1.4 mm of material removed.

Thermal Property Characterization

Heat capacity changes were quantified via modulated differential scanning calorimetry (MDSC) (DSC Q2000, TA Instruments, New Castle, DE) using a ‘heat only’ modulation protocol starting with a cooling ramp from -55 °C to -85 °C followed by a heating ramp from -85 °C to 300 °C, each at a rate of 3 °C/min with an amplitude of 0.48 °C every 60 s. Data was collected and analyzed using Universal Analysis 2000 software (v 4.5A, TA Instruments). Plaques were cross-sectioned with a bandsaw and a razor blade was used to acquire individual milligram-level specimens. Dependent variables examined were MDSC thermogram step change and peak temperatures, and peak areas.

Thermal viscoelastic property changes were quantified via dynamic mechanical analysis (DMA) (DMA Q800, TA Instruments) in tension mode held at a strain of 0.1, under an oscillation frequency of 1 Hz across a temperature range of -115 °C to 180 °C at a heating rate of 2 °C/min. DMA data was collected and analyzed using Universal Analysis 2000 software (v 4.5A, TA Instruments). Specifically, storage modulus (E'), derivative of storage modulus (dE') loss modulus (E''), and tan delta ($\tan \delta$) were analyzed. Samples for DMA analysis were rectangular specimens identical to optical microscopy specimens. For Impacted samples, the whitened material was isolated by manually removing the top ~1.4 mm of non-whitened material with a grinding-polishing wheel using 120 grit sand paper. Non-impacted specimens also had the top ~1.4 mm of material removed. The dependent variables examined were: (1) E' step change temperatures; (2) dE' peak for the inflection point of the step change temperature around -80 °C to -70 °C; (3) E'' and $\tan \delta$ peak temperatures; and (4) the E'' peak height, area, and width at half height of the step change temperature around -80 °C to -70 °C.

Linear thermal expansion changes were quantified via thermo-mechanical analysis (TMA) (TMA Q400, TA Instruments) in expansion probe mode across a temperature range of -115 °C to 235 °C at a heating rate of 5 °C/min under a probe force of 0.01 N. TMA data was collected and analyzed using Universal Analysis 2000 software (v 4.5A, TA Instruments). Samples for analysis were identical to bulk density cylindrical specimens; however, material was not removed post-drilling. The dependent variables examined were TMA thermogram transitions, slopes between transitions (i.e., coefficient of thermal expansion (CTE)), as well as peak and trough temperatures.

Mechanical Property Characterization

Surface mechanical properties were examined on the nanometer scale using load-controlled quasi-static nanoindentation (TI 900 Triboindenter, Hysitron, Minneapolis, MN) at the backside surface of the plaque and along a cross-sectional thickness profile. Loads were applied using a Berkovich-type diamond tip and data was collected and analyzed per Oliver-Pharr method (44) using TriboScan software (v.7.1, Hysitron). The backside surface was quantified using pre-selected maximum applied loads of 1000, 2000, 3000, 4000, and 5000 μN , and reported as a function of the depth of surface penetration (graphically corresponding to the five connected points from left-to-right for each surface condition). The cross-sectional thickness profile was quantified every 100 μm at 5000 μN via traversing from the backside (whitened) surface to the topside (non-whitened) surface. Samples for backside surface and cross-sectional profiling analysis were harvested directly from plaques using a bandsaw. Additional sample preparation for cross-sectional profiling included fine polishing of the sample face using a target surfacing system (Leica EM TXP, Leica Microsystems Inc., Buffalo Grove, IL) at a 2200

rpm speed using incrementally 9 μm , 2 μm , and a 0.5 μm diamond polishing paper until a smooth surface was seen from the instrument mounted optical microscope. Dependent variables examined were depth of surface penetration and reduced modulus. Surface mechanical properties were quantified on the micrometer scale via surface hardness measurement with a Shore D durometer (502D, PTC Instruments, Los Angeles, CA).

Tensile properties were measured via a monotonic pull-to-break test (Insight 10, MTS, Eden Prairie, MN) at an initial gauge length of 25 mm with a speed of testing of 25 mm/min (corresponding to a strain rate of 1.0 min^{-1}) (45). Stress-strain data was collected using TestWorks 4 software (v.4.11C, MTS). Modified ASTM-D638 Type I tensile specimens (3.5" long x 0.5" wide x 0.125" thick) were harvested directly from plaques using a bandsaw (see Figure 47) and edges were hand polished using 240 grit sandpaper. The dependent variables examined were Young's modulus, yield stress, and ultimate tensile stress (UTS).

Statistical Analysis

Statistical analyses were performed using Statistical Package for Social Sciences software (IBM SPSS, v.16, IBM Corporation, Sonoma, NY). Alpha level was set a priori at $\alpha = 0.05$. Effect sizes were calculated using Cohen's d for independent t-test and Cohen's f for analysis of variance (ANOVA). Post-hoc analyses were performed via Tukey HSD tests. The independent variables were (1) impact trial with two levels: Trial 1 (history of zero impact trials) and Trial 12 (history of 11 impact trials); and (2) plaque condition with two levels: Non-impacted (history of zero impact trials) and Impacted (history of 12 impact trials). A summary of analyses performed, independent and dependent variables, and sample sizes across techniques are described in Table 15.

Table 15

Summary of measurement techniques and statistical analyses performed

Measurement Technique	Independent Variable(s) [#]	Dependent Variable(s)	Sample Size	Statistical Analysis(s)
<u>Impact:</u> Linear drop impact	(1) Impact Trial	(1) peak force (2) time to peak force	n=10	two paired samples t-tests
<u>Physical:</u> CIELAB	(1) Plaque condition	(1) L* whiteness	n=5	one independent t-test
<u>Physical:</u> Microscopy: Optical, SEM	(1) Plaque condition	(1) depth of whitening	n=5	none
<u>Physical:</u> Hydrostatic weighing	(1) Plaque condition	(1) bulk density	n=5	one independent t-test
<u>Thermal:</u> MDSC	(1) Plaque condition	MDSC bands	n=5	twelve independent t-tests
<u>Thermal:</u> DMA	(1) Plaque condition	DMA regions	n=5	thirteen independent t-tests
<u>Thermal:</u> TMA	(1) Plaque condition	TMA regions	n=5	fifteen independent t-tests
<u>Mechanical:</u> Nanoindentation: Surface, Cross-section	(1) Plaque condition (2) Applied load	(1) depth of penetration (2) reduced modulus	n=5	two 2 between (plaque condition) x 5 between (load) ANOVAs five independent t-tests
<u>Mechanical:</u> Hardness	(1) Plaque condition	(1) Shore D hardness	n=5	one independent t-test
<u>Mechanical:</u> Tensile test	(1) Plaque condition	(1) Young's modulus (2) yield stress (3) UTS	n=5	three independent t-tests

[#] Impact Trial (2 levels): (1) Trial 1 (History of 0 impact trials), (2) Trial 12 (History of 11 impact trials)

Plaque condition (2 levels): (1) Non-impacted (History of 0 impact trials), (2) Impacted (History of 12 impact trials)

Table 16

Summary of statistical analyses with statistically significant outcomes

Measurement Technique	Dependent Variable	Test Statistic	p value	Effect Size
Linear drop impact	peak force	t = 4.85	p=0.008	d = 2.43
	time to peak force	t = 13.06	p<0.001	d = 6.52
CIELAB	L* whiteness	t = 45.07	p<0.001	d = 15.78
MDSC	Band 4 peak temp	t = 5.15	p=0.001	d = 1.82
	Band 4 peak area	t = 5.05	p=0.001	d = 1.78
	Band 5 step temp	t = 5.68	p<0.001	d = 2.01
DMA	<u>Region 1:</u>			
	Tan δ peak temp	t = 29.75	p<0.001	d = 10.49
	E' onset temp	t = 8.19	p<0.001	d = 2.89
	dE' peak temp	t = 10.15	p<0.001	d = 3.59
	E" peak temp	t = 16.85	p<0.001	d = 6.00
	E" peak area	t = 8.82	p<0.001	d = 3.12
	E" peak height	t = 10.48	p<0.001	d = 3.70
	E" Width half height	t = 9.26	p<0.001	d = 3.28
TMA	T1 onset temp	t = 5.49	p=0.001	d = 1.94
	T6 trough temp	t = 12.63	p<0.001	d = 4.45
	T7 peak temp	t = 9.96	p<0.001	d = 12.33
	Delta Height	t = 17.88	p<0.001	d = 6.38
	T4*T5 CTE	t = 3.52	p=0.008	d = 1.24
	T5*T6 CTE	t = 15.34	p<0.001	d = 5.41
	T6*T7 CTE	t = 14.24	p<0.001	d = 5.03
Nano indentation	<u>depth penetration:</u>			
	interaction	F _{1,9} = 3.62	p=0.009	f = 0.40
	between (plaque)	F _{1,9} = 4.52	p=0.036	f = 0.22
	<u>reduced modulus:</u>			
	interaction	F _{1,9} = 5.59	p<0.001	f = 0.25
	between (plaque)	F _{1,9} = 166.7	p<0.001	f = 1.36
	1000 μ N	t = 2.53	p=0.021	d = 0.60
	2000 μ N	t = 2.75	p=0.013	d = 0.65
	3000 μ N	t = 7.93	p<0.001	d = 1.87
	4000 μ N	t = 10.57	p<0.001	d = 2.49
Tensile test	5000 μ N	t = 10.70	p<0.001	d = 2.52
	yield stress	t = 3.91	p=0.008	d = 1.60
	UTS	t = 12.03	p<0.001	d = 4.90

Results

Numerical results (including tables and figures) are reported as mean \pm one standard deviation, unless otherwise noted. A summary of the statistically significant outcomes across measurement techniques are reported in Table 16.

Linear Drop Impact Testing

Trial 1 was observed to produce a bell-shaped force-time curve (Figure 39). In comparison, the force-time curve of the Trial 12 system shifted up in time (to the right), decreased in force starting around 1.5 msec, and return near the curve peak around 5 msec. Significant differences were observed between plaque conditions for peak force and time to peak force. Peak force values were $5972 \text{ N} \pm 51$ and $5821 \text{ N} \pm 94$ for Trial 1 and Trial 12, respectively. Time to peak force values were $3.65 \text{ msec} \pm 0.13$ and $4.78 \text{ msec} \pm 0.26$ for Trial 1 and Trial 12, respectively.

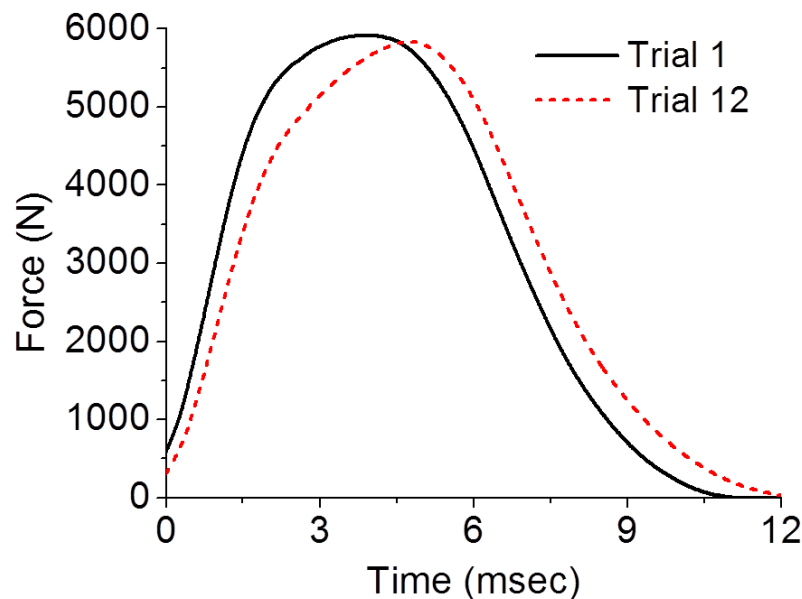


Figure 39. Smoothed force-time curves for Trial 1 (history of zero impact trials) and Trial 12 (history of 11 impact trials) plaque-foam helmet surrogate systems.

Visual Plaque Inspection and Colorimetric Characterization

High speed video revealed substantial plaque deflection and VN600 foam compression during impact testing (Figure 40, left). Visual inspection of plaques after each of the 12 impact trials revealed that final curvature was minimal and each plaque recovered to the original shape. Additionally, the plaque backside displayed new impact-induced rings of whitening after each impact that matched the diameter of the cylindrical drop dart (Figure 40, right). Colorimetric analysis revealed significant differences in L^* between plaque conditions. L^* values were 78.4 ± 0.1 and 87.4 ± 0.4 for Non-impacted and Impacted, respectively.



Figure 40. (left) Maximum compression and deformation of plaque-foam helmet surrogate system during a first impact trial. (middle) The backside of a Trial 1 plaque displaying impact-induced rings of whitening. (right) The backside of a Trial 12 plaque (i.e., Impacted plaque) displaying the increase in rings of whitening.

Optical Microscopy

Optical microscopy between harvested Non-impacted and Impacted specimens revealed that impact-induced whitening penetrated uniformly deep into the backside of plaque material (Figure 41). The Impacted specimen exhibited a defined non-whitened/whitened boundary and yielded a maximum depth of whitening of $1.4 \text{ mm} \pm 0.1$.

Scanning Electron Microscopy (SEM)

Fracture surfaces of Non-impacted and Impacted samples (Figure 42) revealed nanoscale differences in the blended outer shell material composition and morphology.

For Non-impacted, spherical particles of ~25-50 nm in diameter were observed trapped in the matrix material which contained rounded nodules and a distribution of pore sizes ~25-100 nm in diameter. In comparison to Impacted, few spherical particles were observed yet the matrix material appeared more porous with pointed nodules, elongated fibrils, and an estimated pore size of ~1-3 μm .

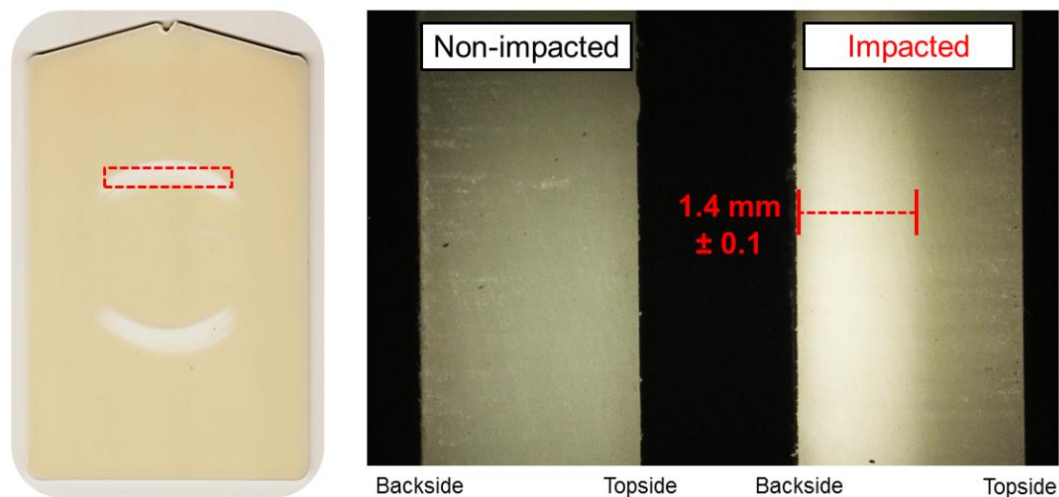


Figure 41. (left) Backside of an Impacted plaque showcasing the location and shape of the harvested specimen used for optical microscopy. (right) Comparison of Non-impacted and Impacted specimens highlighting the uniform depth of whitening into the material, measured at $1.4 \text{ mm} \pm 0.1$. (Note: DMA specimens were produced by removing top ~1.5 mm of material via sanding).

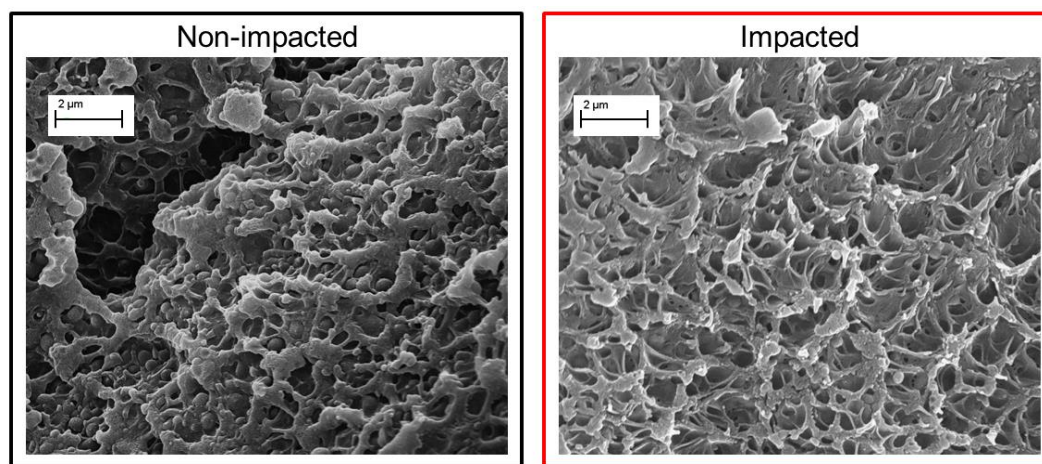


Figure 42. Scanning electron microscopy images of cryo-fracture surfaces of (left) Non-impacted and (right) Impacted outer shell plaque material.

Hydrostatic Bulk Density

No significant differences in bulk density were observed between plaque conditions. Density values for Non-impacted and Impacted were 1.184 ± 0.003 and 1.181 ± 0.004 , respectively.

Thermal Property Characterization - MDSC

Examination of cooling ramp non-reversible and reversible MDSC thermograms (Figure 43, top) revealed a distinct transition in heat flow around -75°C . Examination of heating ramp non-reversible and reversible MDSC thermograms (Figure 43, bottom) revealed several distinctive bands: (1) step change around 75°C , (2) exothermic peak around 120°C , (3) step change and endothermic peak around 140°C , (4) exothermic peak around 200°C , and (5) step change and endothermic peak around 255°C . Analysis of temperatures and areas between plaque conditions (Table 17) revealed statistically significant differences in band 4 peak temperature and peak area, and band 5 step change temperature (Table 18).

Table 17

Heating ramp reversible and non-reversible MDSC thermogram peak temperatures and areas between plaque conditions

Plaque condition	Band 1 Peak Temp ($^{\circ}\text{C}$)	Band 2 Peak Temp ($^{\circ}\text{C}$)	Band 3 Peak Temp ($^{\circ}\text{C}$)	Band 3 Peak Area (J/g)	Band 4 Peak Temp ($^{\circ}\text{C}$)	Band 4 Peak Area (J/g)	Band 5 Peak Temp ($^{\circ}\text{C}$)	Band 5 Peak Area (J/g)
Non-impacted	75.9 ± 0.3	119.7 ± 1.4	140.4 ± 1.1	0.61 ± 0.11	209.1 $\pm 0.9^1$	10.6 $\pm 2.8^2$	257.2 ± 0.5	13.6 ± 3.8
Impacted	75.1 ± 0.8	119.0 ± 1.1	139.4 ± 0.8	0.53 ± 0.07	206.4 $\pm 0.6^1$	3.7 $\pm 0.9^2$	257.5 ± 0.4	9.7 ± 2.1

* Matching superscript number denotes statistical difference ($p < 0.05$)

Table 18

Cooling and heating ramp reversible and non-reversible MDSC thermogram

step change temperatures between plaque conditions

Plaque condition	Cool Ramp Reversible Step Change Temp (°C)	Band 1 Reversible Step Change Temp (°C)	Band 3 Reversible Step Change Temp (°C)	Band 5 Non-reversible Step Change Temp (°C)
Non-impacted	-77.9 ± 0.6	76.2 ± 0.6	140.1 ± 0.7	262.9 ± 1.0 ¹
Impacted	-78.2 ± 0.4	75.5 ± 0.5	139.6 ± 0.8	258.3 ± 1.6 ¹

* Matching superscript number denotes statistical difference ($p < 0.05$)

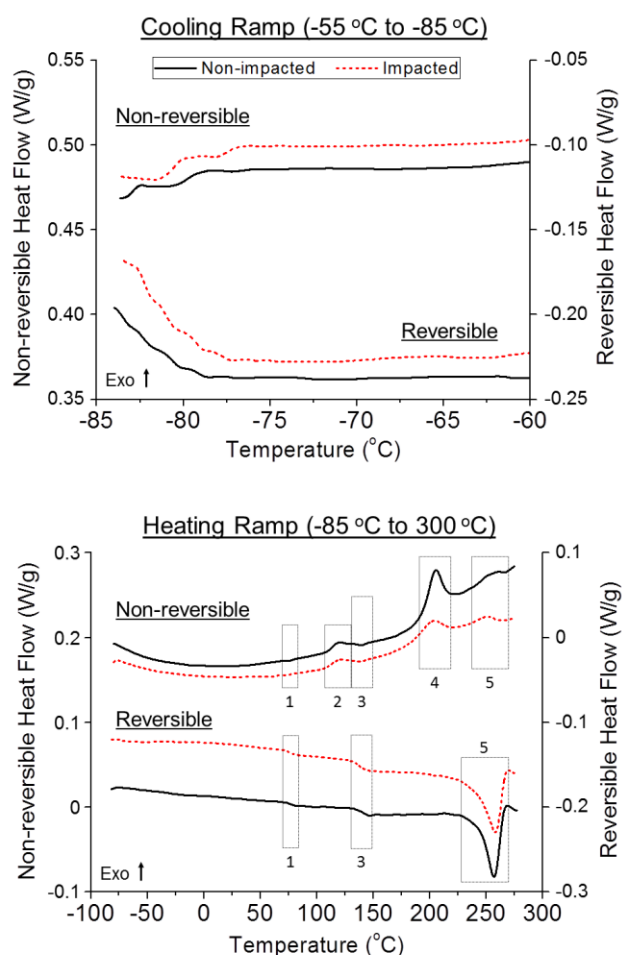


Figure 43. Non-reversible and reversible heat flow MDSC thermograms between Non-impacted and Impacted plaque conditions for (top) cooling ramp and (bottom) heating ramp. (Note: Difference in scale across y-axes).

Thermal Property Characterization - Dynamic Mechanical Analysis (DMA)

Examination of Non-impacted and Impacted DMA thermograms between plaque conditions across Tan δ , E', dE', and E'' signals (Figure 44) revealed distinctive regions in the temperature ranges of: (1) -85 to -65 °C, (2) 70 to 85 °C, and (3) 135 to 155 °C. Tan δ and E'' thermograms exhibited peaks in Regions 1-3, while E' and dE' thermograms exhibited step changes and troughs in Regions 1-3. Analysis of temperatures, areas, heights, and widths (Table 19) revealed significant differences in Region 1 values.

Table 19

DMA thermogram temperatures, areas, heights, and widths for Region 1 (-85 to -65 °C)

Plaque Condition	Tan δ Peak Temp (°C)	E' Onset Temp (°C)	dE' Peak Temp (°C)	E'' Peak Temp (°C)	E'' Peak Area (MPa·°C)	E'' Peak Height (MPa)	E'' Width at half height (°C)
Non-impacted	-73.6 ± 0.3 ¹	-80.9 ± 1.2 ²	-75.3 ± 0.8 ³	-75.0 ± 0.2 ⁴	77.4 ± 9.9 ⁵	19.3 ± 0.2 ⁶	7.9 ± 0.2 ⁷
Impacted	-67.3 ± 0.4 ¹	-76.3 ± 0.3 ²	-69.3 ± 1.1 ³	-70.3 ± 0.6 ⁴	35.5 ± 2.3 ⁵	7.3 ± 0.5 ⁶	10.0 ± 0.4 ⁷

* Matching superscript number denotes statistical difference (p<0.05)

Table 20

DMA thermogram temperatures between plaque conditions for Region 2 (70 to 85 °C) and Region 3 (135 to 155 °C)

Plaque condition	Tan δ Peak Temp (°C)	E' Onset Temp (°C)	E'' Peak Temp (°C)	Tan δ Peak Temp (°C)	E' Onset Temp (°C)	E'' Peak Temp (°C)
Non-impacted	80.2 ± 0.2	73.7 ± 0.3	79.3 ± 0.3	149.2 ± 0.4	139.0 ± 0.3	143.2 ± 0.3
Impacted	80.6 ± 0.2	73.0 ± 0.2	79.7 ± 0.2	149.0 ± 0.2	138.8 ± 0.4	142.7 ± 0.3

* Matching superscript number denotes statistical difference (p<0.05)

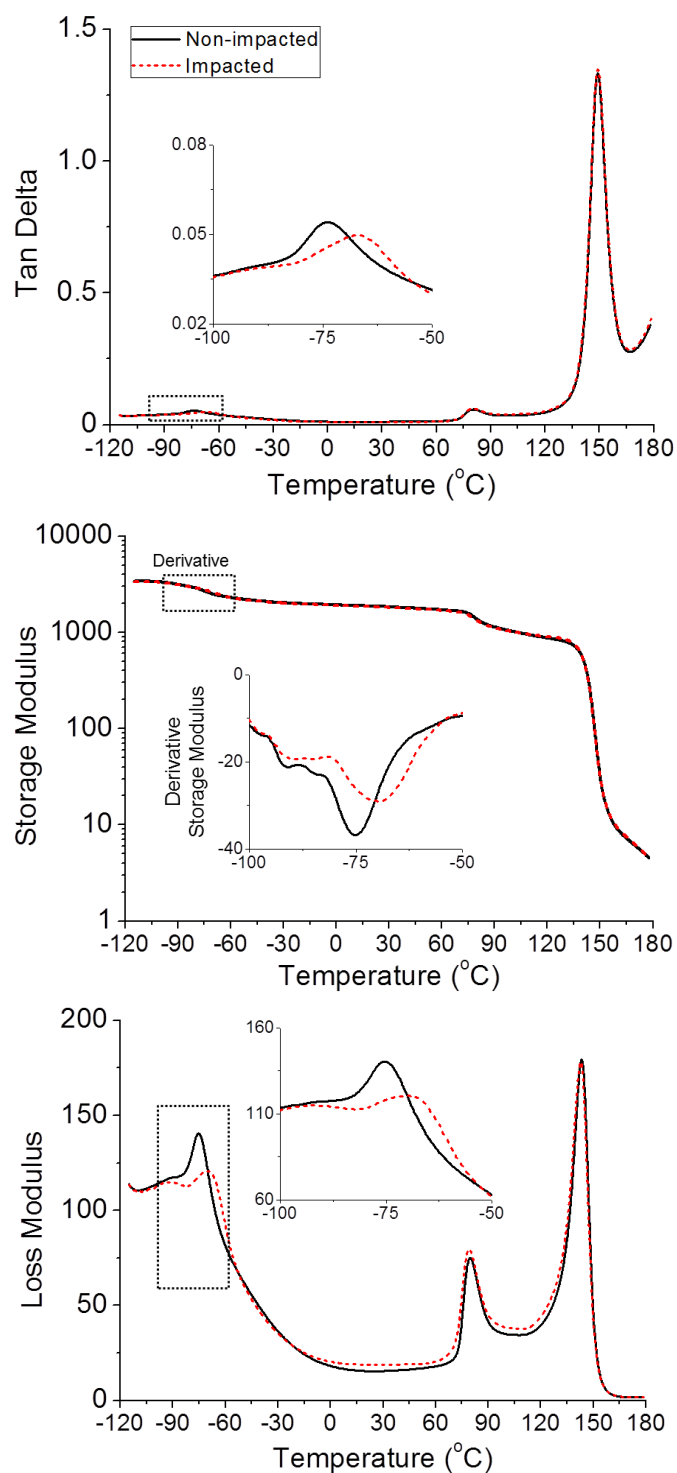


Figure 44. DMA thermograms of (top) tan delta ($\tan \delta$), (middle) storage modulus (E'), and (bottom) loss modulus (E'') between Non-impacted and Impacted plaque conditions. Inset thermograms showcase the -100 °C to -50 °C temperature range for (top) $\tan \delta$, (middle) derivative of E' (dE'), and (bottom) E'' to highlight the consistent ~5 °C shift upwards in Impacted peak temperatures for the selected signals.

Thermal Property Characterization - Thermo-mechanical Analysis (TMA)

Examination of TMA thermograms (Figure 45) between plaque conditions revealed seven distinctive transitions: (T1) onset around -75 °C, (T2) onset around 75 °C, (T3) onset around 140 °C, (T4) onset around 145°C, (T5) peak around 170 °C, (T6) trough around 180-195°C, and (T7) peak around 200-225°C. Additionally, changes in thermogram slopes were observed for pre-T1 and in between T1-T7. Analysis of temperatures, heights, and slopes (Table 21 and 22) revealed significant differences between plaque conditions for T1 onset temperature, T6 trough temperature, T7 peak temperature, T6-T7 Height, T4*T5 slope, T5*T6 slope, and T6*T7 slope.

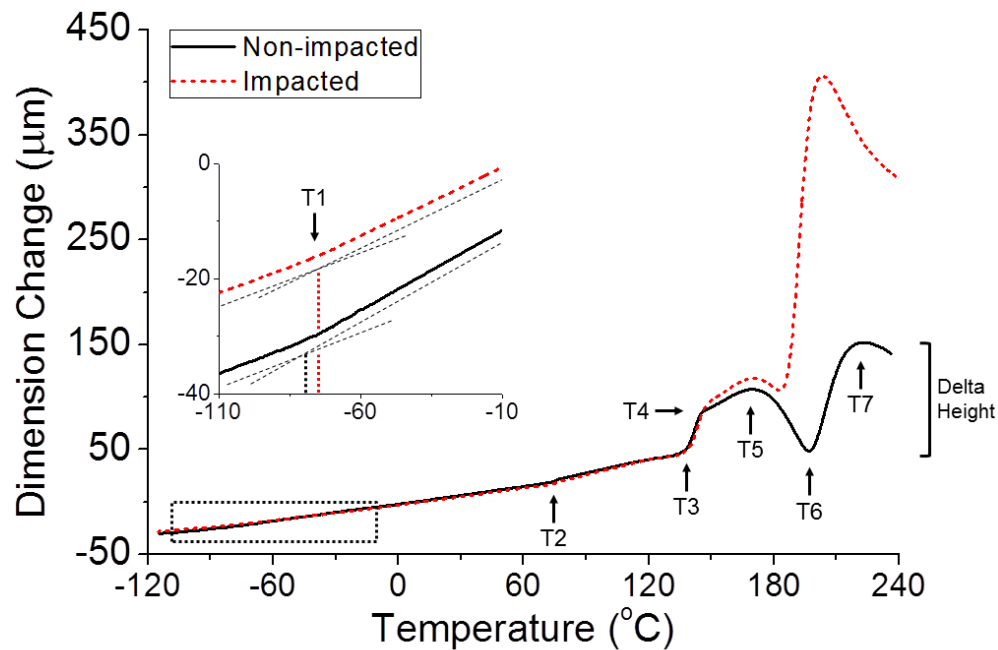


Figure 45. TMA thermograms between Non-impacted and Impacted plaque conditions. Inset thermograms showcase the -110 to -10 °C temperature range to highlight the ~5 °C shift upwards in Impacted onset temperature via the intersection point of traced slope lines.

Table 21

TMA thermogram temperatures and heights between plaque conditions

	T1	T2	T3	T4	T5	T6	T7	T6-T7
Plaque condition	Onset Temp (°C)	Onset Temp (°C)	Onset Temp (°C)	Onset Temp (°C)	Peak Temp (°C)	Trough Temp (°C)	Peak Temp (°C)	Height (µm)
Non-impacted	-79.5 ± 1.8 ¹	73.4 ± 0.9	137.9 ± 0.7	144.1 ± 0.7	168.4 ± 1.2	194.3 ± 1.9 ²	219.6 ± 3.5 ³	90.6 ± 18.1 ⁴
Impacted	-74.4 ± 1.9 ¹	75.0 ± 5.1	137.7 ± 0.7	144.4 ± 0.6	169.4 ± 1.0	178.3 ± 1.6 ²	199.8 ± 2.3 ³	346.7 ± 25.5 ⁴

* Matching superscript number denotes statistical difference (p<0.05)

Table 22

TMA thermogram slopes between plaque conditions

	Pre-T1	T1*T2	T2*T3	T3*T4	T4*T5	T5*T6	T6*T7
Plaque condition	Slope (µm/°C)	Slope (µm/°C)	Slope (µm/°C)	Slope (µm/°C)	Slope (µm/°C)	Slope (µm/°C)	Slope (µm/°C)
Non-impacted	52.2 ± 3.6	80.2 ± 3.5	121.5 ± 9.1	1699.0 ± 143.5	315.2 ± 30.3 ¹	-902.0 ± 53.5 ²	1933.8 ± 614.6 ³
Impacted	55.3 ± 5.3	73.1 ± 6.8	125.9 ± 10.4	1837.0 ± 101.9	384.8 ± 30.1 ¹	-234.1 ± 65.8 ²	9658.2 ± 777.4 ³

* Matching superscript number denotes statistical difference (p<0.05)

Nanoindentation Surface Mechanical Property Characterization

For the backside surface, Impacted reduced modulus was greater than Non-impacted across each of the five applied loads (Figure 46). Analysis of depth of penetration and reduced modulus (Table 16) each revealed two statistically significant main effects: (1) a between effect for plaque condition, (2) an interaction effect between plaque condition and applied load. Post-hoc analysis of reduced modulus revealed significant differences between all applied load combinations except 3000*4000 µN. Additional backside surface analyses measured the difference between Non-impacted and

Impacted reduced modulus for each applied load (Table 16). Comparative analysis across each load revealed that 5000 μN had the largest magnitude of difference quantified by the largest effect size.

For the cross-sectional thickness profile, analysis of depth of penetration and reduced modulus revealed no differences across the sample face for a selected plaque condition. All measurements of mean reduced modulus were observed to be 2.90-2.95 GPa. As a result, no differences were also observed between plaque conditions.

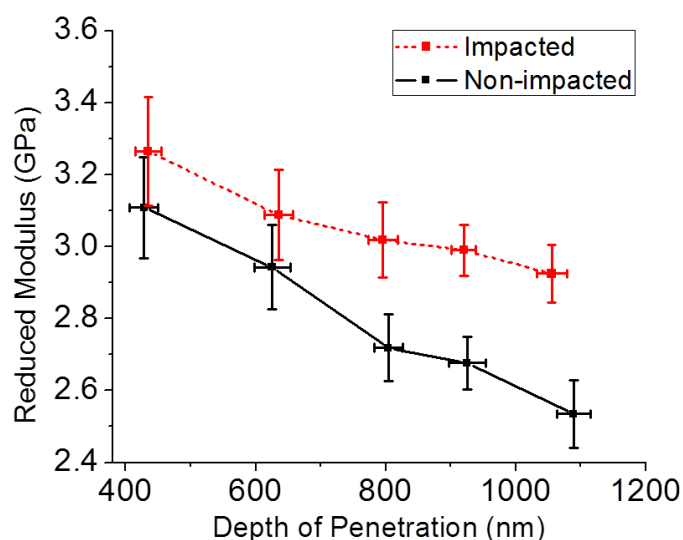


Figure 46. Reduced modulus as a function of depth of surface penetration at the backside surface between plaque conditions.

Mechanical Property Characterization - Surface Durometer

No significant differences were observed in Shore D hardness between plaque conditions. Shore D hardness values for Non-impacted and Impacted were 84.2 ± 1.3 and 84.8 ± 0.8 , respectively.

Mechanical Property Characterization - Tensile

Stress-strain tensile analysis revealed significant differences between plaque conditions for yield stress and UTS. The characteristic stress-strain curve shapes

between Non-impacted and Impacted were observed to be equivalent (Figure 47a); however, Impacted plaques reduced in yield stress and increased in UTS (Table 23). Additionally, all Impacted tensile samples were observed to retain the impact-induced whitening, as well as preferentially yield and fail along the whitened area (Figure 47c).

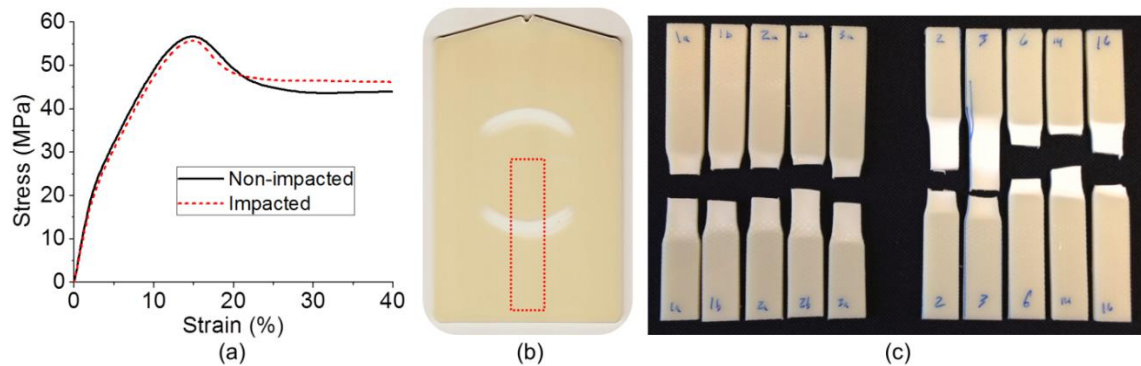


Figure 47. (a) Stress-strain curves for Non-impacted and Impacted plaque conditions. (b) Backside of Impacted plaque showcasing the location of the harvested tensile specimen. (c) (left) Non-impacted and (right) Impacted tensile samples post-test with Impacted samples retaining the impact-induced whitening, as well as preferentially yielding and failing along the whitened area.

Table 23

Tensile mechanical properties between plaque conditions

Plaque condition	Young's modulus (MPa)	yield stress (MPa)	ultimate tensile stress (MPa)
Non-impacted	955.5 ± 27.1	56.2 ± 0.3 ¹	44.0 ± 0.2 ²
Impacted	934.6 ± 21.6	55.3 ± 0.3 ¹	45.8 ± 0.2 ²

* Matching superscript number denotes statistical difference (p<0.05)

Discussion

On-field impact scenarios for American football helmets are forceful, rapid events that differ strongly in magnitude and frequency depending on the position in the field and the level of play. Exposure conditions for the helmet outer shell can vary by impact velocity, effective mass, location site on the shell, direction of the impulse vector, and

impacting surfaces (21). The impact protocol used in this study was selected to attempt to repetitively employ a single on-field linear impact condition to an American football helmet outer shell material. The discussion and interpretation of the results will focus primarily around performance changes and degradative processes related to impact-induced stresses experienced by the outer shell material. Furthermore, the ability to precisely predict the amount of natural end-use exposure that 12 repetitive drop linear impacts represented is complex. No accepted correlation currently exists between our laboratory surrogate testing, *in situ* drop (46) and pneumatic (47, 48) protocols for of full helmets, and on-field impact conditions (49). However, a controlled laboratory setting is suitable because on-field impacts and environmental conditions are highly variable.

Linear Drop Impact Testing

The use of an instrumented drop tower setup has been previously substantiated to study American football on-field tackling scenarios (51), helmet inner liner components (50), and helmet-liner surrogate setups (30-32). The linear drop test protocol used herein attempted to more accurately employ an on-field impact condition compared to previous setups (30-32, 50). The polyurethane drop dart with hardness (72 Shore D) comparable to the helmet-grade plaque (84 Shore D) was selected in an attempt to employ a shell-to-shell on-field impact event. The single block of VN600 foam for the plaque-foam helmet surrogate with a thickness of 25.4 mm was selected to match a common American football helmet design (52). The impact treatment of ten trials, which resulted in a total exposure of 12 repetitive impact trials, corresponded to the expected exposure frequency during an American football game across high school (22) and college levels (15, 16). The remaining input parameters of impact velocity (40), impact mass (39), MEP pad

anvil (39, 42), and interval between repetitive trials (39) matched established helmet standards. Furthermore, the use of a new block of VN600 foam for the final trial properly isolated the change in impact performance of solely the plaque and enabled an accurate comparison between Trial 1 and Trial 12.

The change in characteristic curve shape between Trial 1 (Non-impacted; history of zero impact trials) and Trial 12 (history of 11 impact trials) indicated a change in plaque impact performance (Figure 39). Compared to Trial 1, the Trial 12 curve visibly reduced in loading rate starting at ~1.5 msec until ~5 msec. The maximum deviation in force between force-time curves was observed around 3 msec. Borrowing from traditional stress-strain terminology to characterize analogous force-time behavior, the Trial 12 reduction in loading rate (i.e., reduction in stiffness) occurred in the anelastic regime whereby the mechanical response is reported to depend on thermal history (53). Computational drop impact analysis of a PET helmet shell reported that reductions in helmet shell stiffness led to decreased linear head accelerations at impact velocities of 4.4 and 5.4 m/sec, yet higher linear head accelerations at 7.7 m/sec. In a stress-strain curve, the anelastic regime begins at the deviation from the initial stress-strain linearity and ends at the yield peak, whereby the reversible elastic yielding phase (54) gives way to the macroscopic onset of irreversible plastic deformation (55), respectively. At the molecular-level, anelastic behavior is reported to initiate as van der Waals forces collapse and individual polymer chains begin displacing (56), while microscopically it has been reported as the appearance of surface-specific crazes (57).

The statistically significant decrease in peak force and increase in time to peak force further revealed that the impact treatment induced a change in plaque impact

performance. Due to the replacement of foam for Trial 12, we suggest that the changes in curve shape, peak force and time to peak force were the direct result of changes in impact energy management of the plaque material. As a result, our linear drop test protocol was substantiated to quantify differences in impact performance.

Visual Plaque Inspection and Colorimetric Characterization

The severe plaque deflection and foam deformation, observed during impact (Figure 40, left), showcased that the impact protocol delivered a substantial loading condition to the helmet surrogate system. The maximum deflection of the plaque was observed to occur at the edge of the dart, which matched the location of the rings of whitening visibly observed on the backside surface after each impact trial (Figure 40, right). Specifically, the rings formed only along the 6" axis of the plaque backside, which demonstrated the increased resistance to deformation (i.e., increased stiffness) along the shorter 4" width. Further, the lack of whitening on the plaque topside indicated that stresses during the impact event were greater at the backside surface.

The significant increase for L^* revealed a major surface color change between Non-impacted and Impacted plaques. Color changes in RT-PC (28, 33, 34) and RT-PET (35-37) blended systems under mechanical stress have been reported due to the cavitation of RT particles or delamination of the matrix-RT interface. In either case, the localized clusters and arrays of voids serve to alter the refractive index of the material and scatter the transmitted light. Additionally, neat PET systems are reported to whiten due to crystallization under plastic deformation (58, 59). In a semicrystalline material under stress, the whitened appearance can be the result of localized crazing of polymer chains

producing a void, or the growth of new or existing crystal domains. Thus, further property analysis is required to elucidate mechanisms responsible for stress-whitening.

Optical Microscopy

The presence of impact-induced rings of whitening only on the backside surface warranted investigation of stress-whitening into the bulk thickness of the plaque. The cross section of Impacted specimen (Figure 41, right) exposed that the whitening tapered off into the bulk of the sample to create a visual non-whitened/whitened boundary. Furthermore, following the boundary line away from the center of the specimen (i.e., moving to the top or the bottom of the Impacted cross-sectional face) revealed that the whitened area disappeared and the boundary line traced a non-linear half-circle shape (24, 28, 33, 34, 38). The maximum depth of whitening was measured at the center of the rings of whitening and quantified at 1.3-1.5 mm. As a result, we conclude that the impact exposure induced stress-whitening into the plaque up to a maximum of ~40-45%.

Scanning Electron Microscopy (SEM)

Nanoscale-level microscopy has been used extensively to examine fracture surfaces of rubber toughened systems to characterize deformation mechanisms and stress-strain behaviors (28, 33-37). Non-impacted and Impacted plaques did not experience catastrophic failure during impact testing, thus SEM samples were cryogenically cooled to preserve morphology prior to fracture required to gain exposure to the bulk material.

The Non-impacted and Impacted cryo-fracture surfaces (Figure 42) were each characteristic of a brittle fracture with a highly rough surface and a lack of directional deformation (37). For Impacted, RTs did not appear stretched or deformed, yet the absence of RTs suggested complete delamination of the matrix-RT interface due to the

impact treatment. Large pores bordered by elongated fibrils demonstrated the preferential yielding behavior of the PC/PET matrix. The resultant void size and concentration is postulated to scatter transmitted visible light and be a potential source of stress-whitening. For Non-impacted, RTs on the size range of 25-50 μm were estimated for the blended material. The smaller concentration and size of voids suggested that RTs dislodged from the matrix during cryo-fracture. As a result, we postulate that delamination at the matrix-RT interface resulted in void creation. However, further investigation is required to fully disqualify the presence of internal RT cavitation (28).

Hydrostatic Bulk Density

Increased porosity observed with SEM at the nanoscale prompted investigation into density changes of the material. By determining the depth of whitening using optical microscopy, the thickness of degraded material was effectively identified into the Impacted material. A grinding-polishing wheel was used to remove ~ 1.8 mm of the non-whitened topside specimen surface in order to isolate the whitened material. The lack of differences between plaque conditions suggested that 12 repetitive impacts did not alter the bulk density of the Impacted helmet-grade material.

Additional analysis harvested identical cylindrical specimens out of a commercial off-the-shelf outer shell and revealed no differences in bulk density. The match in bulk density between the helmet-grade plaque and the off-the-shelf outer shell suggested that our injection molding parameters are suitable to replicate commercial American football helmet outer shell materials, and provided further support toward meaningful interpretation of our results.

Thermal Property Characterization - MDSC

Thermal property analysis was conducted to further elucidate the source of impact-induced stress-whitening. MDSC was selected to examine the changes in reversible and nonreversible thermal phenomena in the multi-component blended material. A single heating ramp was unable to probe the lowest temperature phenomena due to the lower limit of the equipment (-90 °C) and a “start-up hook” artifact that is commonly observed during system equilibration (60). As a result, an initial cooling ramp examined the low temperature region. Additionally, a razor blade was cautiously used to acquire specimens; however, it is noted that the harvesting process inherently introduced localized stress to the edges of the milligram samples.

The morphological complexity of the helmet-grade blend material was manifested via the distinct features in the cooling and heating ramp MDSC thermograms (Figure 43). For the cooling ramp, the Non-reversible and Reversible heat flow transitions around -78 °C corresponded to the glass transition temperature (T_g) of ABS-RT (23). The T_g of ABS-RTs is commonly driven by the butadiene component, which is reported around -90 °C (5, 23). Within a blended material, the measured ABS-RT T_g will depend on the amount and condition of the rubber particle, as well as the interaction and adhesion with the matrix (5, 23). For the heating ramp, the Reversible step changes around 75 °C and 140 °C corresponded to the glass transition temperature (T_g) of PET and PC, respectively (30). The endothermic peak around 140 °C corresponded to the enthalpy recovery that occurred near the T_g of PC, which corresponds to the thermal history of the helmet-grade material and serves to quantify the degree of physical aging (30). The exothermic peak around 120 °C that preceded the 140 °C endothermic peak was representative of pre- T_g

artifacts (60). The exothermic peak around 200 °C was characteristic of the cold crystallization temperature (T_{cc}) of PET and the endothermic peak around 257 °C matched the T_m of PET (30, 32). The Non-reversible step change around 260 °C represented the onset of complete melting of all crystallites and the subsequent cessation of recrystallization events at the melting temperature (T_m) of PET (30).

Consistent significant outcomes were observed for PET T_{cc} , (band 4) whereby statistically significant reductions in peak temperature and area (Table 16) demonstrated a substantial increase in the degree of crystallization in the whitened area of Impacted plaques. The results supported colorimetric findings whereby an increase in the degree of crystallization is expected due to stresses generated by the impact treatment. For cold drawn films, a similar trend in PET T_{cc} peak area and peak temperature is observed (61, 62). The mechanical orientation of PET is reported to promote mobility and alignment of polymer chains which will facilitate molecular-level backbone rearrangements, enable confirmation across chain segments, and lead to reduced free energies for nucleation and crystal growth (62). This is called strain-induced crystallization and is more facile with increased levels of elongation and decreased strain rates.

Conversely, a variation in significant outcomes was observed for PET T_m (band 5). The lack of statistical difference in PET T_m area (Table 17) demonstrated that the total crystallinity was equivalent between plaque conditions upon reaching the melting transition during the heating ramp. In other words, the heat ramp through PET T_{cc} induced the cold crystallization for the Non-impacted condition, whereas the impact treatment and the heat ramp induced the cold crystallization for the Impacted condition. We postulate that a change in T_m area would require a change in crystallinity potential via

an alteration in the degree of polymerization (e.g., chain scission, crosslinking, etc.). The statistically significant reduction in PET T_m step change (Table 18) supported a less perfected crystal structure for the Impacted condition due to the lower temperature to cease all melting (63). Additionally, the lack of change in PET T_m peak temperature demonstrated a stability of the formed PET crystalline domains. As a result, we postulate that mechanical orientation during the 12 repetitive impacts elicited the strain-induced cold crystallization of PET in Impacted plaques.

Thermal Property Characterization - DMA

In addition to studying heat capacity changes with MDSC, the thermal dependence on visco-elastic properties was performed using DMA. Similar to bulk density samples, optical microscopy effectively identified the depth of whitening and ~1.8 mm of the top side specimen surface was removed in order to isolate and test only the degraded, whitened material. Rectangular bars were harvested in parallel with the rings of whitening in order to maximize the amount stress-whitening in each specimen. Finally, DMA testing above 170 °C induced the onset of bulk material softening during testing deformed the specimen, but the stress-whitening that was visible pre-test was no longer present post-test.

The viscoelastic complexity of the helmet-grade outer shell material was exhibited by the DMA thermograms which contained three regions (Figure 44). For Region 1, the E' onset temperature around -80 °C and the $\tan \delta$, dE' , and E'' peak temperatures around -70 °C (Table 19) corresponded to the ABS-RT T_g (64, 65). For Region 2, the E' onset temperature around 73 °C and the $\tan \delta$ and E'' peak temperatures around 80 °C (Table 20) represented the PET T_g (66-69). For Region 3, the E' onset

temperature around 139 °C, the Tan δ peak temperature around 149 °C, and the E'' peak temperature around 143 °C (Table 20) corresponded to the PC T_g (70, 71). The observed ABS-RT, PC, and PET T_g ranges corroborated with MDSC results.

The statistically significant increases in ABS-RT Tan δ , E', dE', and E'' T_g temperatures (Table 16) revealed a significant shift in the visco-elastic properties of the rubber. Similar upward shifts in RT Tan δ T_g have been reported in rubber toughened thermoplastic systems exposed to uniaxial compression (72-74) and tension (73). For PET-RT, maximum upward shifts of 7 °C and 4 °C were reported under static uniaxial compression or tension, respectively (37). The authors postulated that RT cavitation increased RT T_g because of increased butadiene density via a reduction in free volume.

The statistically significant increases in ABS-RT E'' peak area, peak height, and width at half height (Table 16) demonstrated a shift in the distribution of available energy damping mechanisms of the ABS-RT. Peak broadening of the RT T_g is reported for a RT blend under uniaxial tensile stress (74) and postulated to reflect a wider population of rubber particles with varying degrees of cavitation and deformation (37, 64, 65, 74). It is noted that additional shifts in width, height, and area for the Tan δ peak were potentially present (Figure 44, left), however the peak was too small for reliable results and therefore were not reported. Overall, the quantifiable thermogram shifts at ABS-RT T_g suggested the occurrence of RT cavitation and supported colorimetric and SEM results.

Assignment of the origin of relaxation peaks can be difficult in rubber toughened blends as the T_g of the rubber phase can sometimes overlap with the beta transition temperature (T_β) of the matrix material (5). The T_β for PC and PET, along with the ABS-RT T_g, are each commonly reported around the range of Region 1 (-85 to -65 °C).

Literature for mechanically deformed PC reported no shifts in T_{β} , but rather the formation a shoulder plateau extending downward in temperature off the T_g peak (70, 71). The shoulder plateau is postulated to form due to a pseudo-second phase whereby molecular mobility and ductility is increased in localized zones of the deformed glassy polymer (70, 71, 75-77). Literature for mechanical deformed (67) or annealed (66, 68, 69) PET is reported to increase orientation and crystallinity leading to no change in T_{β} , but rather an upward shift in T_g that is often accompanied by a decrease in peak intensity combined with peak broadening. Therefore, we postulate that only alterations to the ABS-RT component were quantified with DMA due to significant peak shifts in Region 1 combined with the lack thermogram changes around the PC and PET T_g peaks.

Thermal Property Characterization - TMA

The presence of thermally driven changes in the linear expansion and contraction were measured via expansion probe TMA. Specimens did not undergo a secondary grinding process to isolate the whitened material because the flat-tipped expansion probe is highly sensitive to flatness of the sample and no isolation process was found to retain the as-molded surface precision. Thus, it is noted that the Impacted sample was only ~40-45% whitened material and must be considered when interpreting the Impacted results. Finally, TMA testing above 240 °C caused the expansion probe to penetrate and deform the specimen surface during testing, but the stress-whitening that was visible pre-test was no longer present post-test.

The complexity of the uniaxial dimensional stability of the helmet-grade outer shell material was exhibited by the TMA thermograms which contained seven transitions (Figure 45). For T1, T2 and T3, the onset temperatures around -80 °C, 75 °C, and 138

°C, corresponded to the increase in linear expansion at the ABS-RT T_g (73, 78) PET T_g (79), and PC T_g (80, 81), respectively. In contrast, the expansion behavior observed for transitions T4 through T7 was not well reported in the literature. For T4, the onset at 144 °C corresponded to a decrease in linear expansion post-PC T_g (82). For T5, the peak temperature around 170 °C corresponded to a post-PC T_g linear contraction (83). For T6, the trough temperature around 180-195 °C corresponded to a switch to linear expansion that is described in PET fiber literature as crystal perfection (84) and aligned with the onset of the PET T_{cc} peak in our MDSC results (Table 21). For T7, the peak around 200-220 °C corresponded to a linear contraction that is reported in PET fiber literature as PET T_m (79, 84). Overall, the observed ABS-RT T_g , PC T_g , PET T_g and PET T_{cc} ranges corroborated with MDSC and DMA results.

The CTEs were quantified in between the seven transitions of the TMA thermograms (Table 22). For Pre-T1, T1*T2, T2*T3, T3*T4, and T4*T5, the CTE ranges of 50-60, 70-80, 110-135, 1600-1900, and 300-400 $\mu\text{m}/^\circ\text{C}$, corresponded to linear expansion below the ABS-RT T_g , between the ABS-RT T_g and PET T_g , between the PET T_g and PC T_g , at the post-PC T_g , and before the post-PC T_g softening, respectively. For T5*T6, the CTE range of -850 to -200 $\mu\text{m}/^\circ\text{C}$ represented the linear contraction pre-PET T_{cc} . For T6*T7, the CTE range of 1500-10500 $\mu\text{m}/^\circ\text{C}$ corresponded to thermal expansion pre-PET T_m .

The statistically significant increase in ABS-RT T_g (Table 16) demonstrated that the impact treatment altered the thermal expansion behavior of the butadiene rubber, and matched the ~5 °C upward shift in ABS-RT T_g observed in the DMA Region 1 results. The results provided further evidence for the occurrence of RT cavitation (73, 78).

The statistically significant differences in the PET T_{cc} trough, PET T_m peak, and Delta Height, as well as the CTEs of post-PC T_g expansion, pre-PET T_{cc} softening, and pre-PET T_m expansion (Table 16), collectively revealed a substantial shift in thermal expansion behavior between plaque conditions. The results supported the MDSC results that revealed an increase in PET crystallinity. Most notably, the impact treatment altered the thermogram curve shape above 170 °C, where the Impacted curve narrowed between T4 and T7 with a drastic increase in dimensional change after T6. The T6-T7 Height between the T6 trough and the T7 peak (Table 21) was ~4x larger for Impacted and the maximum dimension change of ~400 μ m equated to >10% uniaxial expansion.

The direction and degree of orientation of strain-induced crystallization is reported to govern the dimensional stability behavior of a semicrystalline material (85). Mechanically oriented PET is reported to exhibit thermal contraction parallel to the draw direction, yet exhibit thermal expansion in the perpendicular direction (86, 87). Furthermore, the amount of expansion or contraction, as well as the expansion-contraction transition, is influenced by draw ratio and temperature as well as annealing time and temperature (79, 86-89). Therefore, we hypothesize that repetitive impacts induced the orientation of PET chains and crystals parallel to the rings of whitening (Figure 48, middle). For Impacted, the orientation was perpendicular to the downward force of the expansion probe. Upon heating above 170 °C, the anisotropy of the oriented PET chains contracted perpendicular to the expansion probe and induced linear expansion (Figure 48, right). Comparatively for Non-impacted, the orientation due to the injection molding process was revealed by the T6-T7 CTE of the pre-PET T_m expansion and quantified by T6-T7 Height.

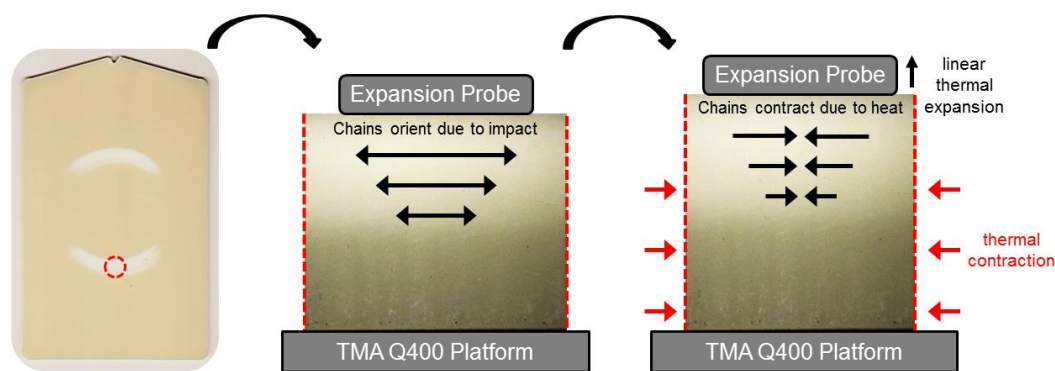


Figure 48. Impacted TMA specimen schematic showcasing the (left) harvested location and shape; (middle) placement during TMA testing and the direction of the impact-oriented chains relative to the probe; and (right) concurrent linear contraction perpendicular to the linear thermal expansion uniaxially measured by the probe.

Nanoindentation Surface Mechanical Property Characterization

The surface properties of the plaque backside were quantified (Figure 46) using quasi-static nanoindentation at five discrete loads and revealed that the impact treatment increased the resistance to deformation (i.e., stiffness increase) at the plaque backside surface. The results supported the increase in PET crystallization in MDSC results, the increase in PET orientation in SEM and TMA results, and the increase in butadiene density via RT cavitation suggested by colorimetric and DMA results. The interaction effects (Table 16) revealed that the rates of change in penetration depth and modulus across applied loads were different between Non-impacted and Impacted. For example, as the applied load increased ($1000 \mu\text{N} \rightarrow 5000 \mu\text{N}$) the difference in reduced modulus between plaque conditions increased ($0.15 \text{ GPa} \rightarrow 0.40 \text{ GPa}$), which suggested a nonlinear viscoelastic stress-strain behavior within the material (30). Additionally, the significant results across independent t-tests revealed that the Impacted reduced modulus was greater for each applied load. The consistent increase in effect size ($d=0.60 \rightarrow d=2.52$) with increase in applied load ($1000 \mu\text{N} \rightarrow 5000 \mu\text{N}$) confirmed the interaction effect for reduced modulus. In other words, the difference in reduced modulus grew (i.e.,

increased rate of change) with applied load, analogous to a favorable increase in the signal-to-noise ratio. Thus, an applied load of 5000 μN was selected to provide the highest potential to analyze property changes across the cross-sectional thickness.

Cross-sectional thickness profiling results suggested that the impact treatment did not alter the mechanical properties measured into the bulk of stress-whitening material. However, potential factors are postulated to cause the observed lack of differences. Initially, our hypothesis for profiling was two-fold: (i) for Non-impacted, a consistent reduced modulus of ~ 2.5 GPa across the sample face that matched the observed reduced modulus at 5000 μN (Figure 46) and (ii) for Impacted, a reduced modulus of ~ 2.9 GPa in the whitened area that would transition downward near the stress-whitening boundary (Figure 41) and decrease to ~ 2.5 GPa in the non-whitened area. As a result, we postulate that sample preparation may have precluded quantifiable differences along the cross-sectional thickness as supported by the observed significant backside surface results. Analysis suggests a smooth surface roughness is required for reliable results to quantify potential shifts in surface mechanical properties into the bulk.

Durometer Surface Mechanical Property Characterization

The quantification of surface mechanical properties on the micrometer scale was performed by traditional Shore D hardness measurements using a handheld durometer. The lack of Shore D differences between plaque conditions compared to the increase in reduced modulus at the nanometer scale further demonstrated a sensitivity difference between the two surface mechanical property measurement techniques (30). While the precise maximum applied load during Shore D testing was unknown, we postulate that the force was much larger than that for nanoindentation (5000 μN). As a result, the

analysis suggested that Shore D durometers are potentially overly forceful to quantify shifts in surface mechanical properties of injection-molded American football helmet outer shell materials exposed to repetitive linear drop impacts.

Mechanical Property Characterization - Tensile

Tensile mechanical properties between plaque conditions were quantified using a modified ASTM-D638 monotonic tensile test protocol. The strain rate (1.0 min^{-1}), use of sandpaper for sample preparation, and specimen width matched D638 setup conditions (45). Modified Type I specimens were harvested from the center of the rings of whitening using a band saw (Figure 47b). The whitened area was centered along the 3.5" length and centered within the 25 mm gauge length. The edges were manually sanded to eliminate flash and burrs prior to testing; however, the inability to precisely obtain a blemish-free finish resulted in stress-concentrating defects present along the sample surface. As a result, strain at break was highly variable and was not reported.

The equivalent characteristic curve shapes between plaque conditions (Figure 47a) demonstrated an equivalent overall response in stress-strain behavior. Additionally, minor whitening was observed along the necked region of all specimens. For all Impacted specimens, the onset of macroscopic yielding was observed to initiate at the whitened area in the center of specimens. The preferential necking (Figure 47c) suggested a localized decrease in the resistance to deformation (i.e., stiffness) in the stress-whitened material. Furthermore, the prominent ring of stress-whitening was elongated, but not erased during specimen failure. Compared to DMA and TMA specimens where whitening disappeared post-test, we postulate that the localized temperature did not sufficiently elevate to eliminate stress-whitening.

The statistically significant decrease in yield stress and increase in UTS (Table 16) demonstrated that 12 linear drop impacts resulted in a significant shift in tensile mechanical properties. The reduction in yield stress (Table 23) demonstrated a lowered onset of bulk-level irreversible viscoelastic deformation (i.e., earlier softening) and supported the decrease in peak force during impact testing. The increase in UTS demonstrated a higher applied stress required during the plastic flow regime and supported the increase in crystallinity in MDSC and TMA testing. Additionally, the plastic flow direction during testing was parallel to the postulated chain and crystal orientation in tensile specimens and further supported the increase in strain-hardening behavior. Specifically, changes in molecular-level characteristics, such as chain orientation, chain entanglement concentration, and intermolecular forces serve to drive morphological crystallinity changes at micro-level which collectively influence the system's ability to exhibit plastic flow at the macro-level (90). The lack of change in Young's modulus revealed no change in the resistance to deformation at low strains and supported the lack of change in E' during DMA testing. Overall, tensile results supported that impact exposure led to a significant bulk-level shift in mechanical properties whereby the localized ~40-45% of stress-whitened material led to a 2% decrease in yield stress and a 4% increase in UTS.

Interestingly, mechanical property testing of a blended RT system, that has undergone a stress-whitening event, was not found in the open literature. Rather, studies primarily induced fracture in specimens to elicit a stress-whitening response, thus eliminating the ability for analysis of mechanical property changes. We postulate this

study may be the first to analyze the changes in surface and tensile mechanical properties of a stress-whitened RT blended system that have not undergone catastrophic failure.

Conclusions

The investigation implemented an impact protocol that employed a single expected on-field impact condition repetitively to a plaque-foam helmet surrogate and quantified the effects upon the functional properties of a stress-whitened American football helmet outer shell material. The helmet-grade plaque was composed of a PC/PET blend material impact-modified with ABS-RTs. Changes in impact performance corresponded to significant shifts in surface and tensile mechanical properties. To our knowledge, this is the first time mechanical properties of a non-fractured, stress-whitened rubber-toughened material have been reported. Physical property analysis quantified the visually observed color change, revealed that up to 40-45% of the plaque thickness was whitened, and suggested elongation of the PC/PET matrix and delamination at the matrix-RT interface. Thermal property analysis further suggested the concomitant occurrence of ABS rubber-toughener cavitation (via DMA and TMA results), and strain-induced PET crystallization (via MDSC and TMA results). The overlap of thermal techniques verified temperature ranges and characteristic shifts in thermal phenomena.

The presence of cavitation and crystallization is not unforeseen, as the addition of rubber-toughener particles to a mechanically deformed semicrystalline matrix would not eliminate the potential for strain-induced crystallization. In effort to elucidate the potential source of stress-whitening, we postulate that the visually observed stress-whitening was due to voids generated via cavitation of the rubber particle leading to delamination at the RT-matrix interface. However, further microscopy investigation at

the nanoscopic level is required to confirm our hypothesis. Future work will also examine the origin of the stress-whitening disappearance observed post-test in DMA and TMA specimens, and explore the potential for physical, thermal, and mechanical property recovery with thermal annealing.

Currently, the degree and rate of impact performance changes of American football helmet components and constituent materials throughout service lifetimes is not clearly understood. This study collectively provides a suggested model towards the assessment of impact-induced degradation of protective headgear materials. Changes in physical, thermal, and mechanical properties were characterized in a step-wise progression and a battery of diagnostic tools was identified to evaluate concurrent changes at the nanoscopic, microscopic, and macroscopic levels. Interestingly, the aesthetic desire for selected paint designs or white pigmented outer shells could serve to mask the cosmetic indicator of stress-whitening in rubber-toughened helmet-grade blends. Additionally, continued development of a drop test protocol to accurately match the loading conditions of *in situ* and on-field impact events is still required. We believe that polymer analysis herein could afford polymer scientists and sports engineers an additional toolbox beyond traditional biomechanical measurements to compare dosage exposures and calculate scaling factors. Ultimately, the ability to conduct on-going diagnostic evaluations of material property changes of full helmet systems under end-use conditions could serve to (1) comprehensively understand the relationship between polymer-level degradation and helmet-level deterioration, (2) provide data-driven decisions for new helmet technologies, and (3) understand and predict (91) the potential increased risk of head injury to the athlete throughout the lifecycles of helmet shells.

References

- 1 Gale A and Mills NJ. Effect of polystyrene foam liner density on motorcycle helmet shock absorption. *Plastics and Rubber Processing and Applications* 1985, 5: 101-108
- 2 Vetter L, Vanderby R, and Broutman LJ. Influence of materials and structure on performance of a football helmet. *Polym Eng Sci* 1987, 27(15): 1113-1120
- 3 Gilchrist A and Mills NJ. Impact deformation of ABS and GRP motorcycle helmet shells. *Plastics and Rubber Processing and Applications* 1994, 21: 141-150
- 4 Ragagnin F. Analysis of the structural behavior of ski helmets during impact and penetration tests. 2013. Masters Thesis, University of Padova, Italy
- 5 Bucknall CB. Chapter 8: Rubber toughening. In: Haward RN and Young RJ (eds) *The physics of glassy polymers*. 2nd ed. London:Chapman & Hall, 1997, 363-412
- 6 Wypych G. *Handbook of Material Weathering*, 4th ed.; ChemTec: Toronto, 2008
- 7 Fisher E. 10-year helmet reconditioning policy – Press Release. National Athletic Equipment Reconditioners Association, 2011
- 8 Riddell 360 Fitting Instructions and Helmet Care – Helmet Warranties, 2011.
- 9 Schutt Helmet Fitting Instructions. 2011. Schutt Sports, Inc.
- 10 Xenith X2E Helmet Fitting Instructions. 2013. Xenith, LLC.
- 11 Xenith EPIC Helmet Fitting Instructions. 2013. Xenith, LLC
- 12 Rawlings Warranty Information. 2013. Rawlings Sports Goods, Inc.
- 13 Texas State Education Code – Section 33.094, 2011. Football Helmet Safety Requirements. Added September 1, 2011.

- 14 Pellman EJ, Viano DC, Tucker AM, et al. Concussion in Professional Football: Location and Direction of Helmet Impacts – Part 2. *J Neurosurgery* 2003, 53(4): 1328-1341
- 15 Crisco JJ, Fiore R, Beckwith JG, et al. Frequency and Location of Head Impact Exposures in Individual Collegiate Football Players. *J Athl Training* 2010, 45(6): 549-550
- 16 Broglio SP, Surma T, and Ashton-Miller JA. High school and collegiate football athlete concussions: biomechanical review. *Ann of Biomed Eng* 2012, 40(1): 37-46
- 17 Daniel RW, Rowson S, and Duma SM. Head Impact Exposure in Youth Football. *Ann of Biomed Eng* 2012, 40(4): 976-981
- 18 Cobb BR, Urban JE, Davenport EM, et al. Head Impact Exposure in Youth Football: Elementary School ages 9-12 years and the effect of practice structure. *Ann of Biomed Eng* 2013, 41(12): 2464-2473
- 19 Urban JE, Davenport EM, Golman AJ, et al. Head Impact Exposure in youth football: high school ages 14 to 18 years and cumulative impact analysis. *Ann of Biomed Eng* 2013, 41(12): 2474-2487
- 20 Wong RH, Wong AK and Bailes JE. Frequency, magnitude, and distribution of head impacts in Pop Warner football: The cumulative burden. *Clinical Neurology and Neurosurgery* 2014, 118: 1-4
- 21 Hoshizaki TB, Post A, Oeur RA, et al. Current and future concepts in helmet and sports injury prevention. *J Neurosurgery* 2014, 75 (4): 5136-5148

- 22 Broglio SP, Eckner JT, Martini D, et al. Cumulative Head Impact Burden in High School Football. *J Neurotrauma* 2011, 28: 2069-2078
- 23 Bucknall CB. Chapter 3: Characterisation of Structure. In: Bucknall CB, Holliday L and Kelly A. (eds) *Toughened Plastics*. 1st ed: Springer Science, 1977, 39-65
- 24 Parker DS, Sue HJ, Huang J, et al. Toughening mechanisms in core-shell rubber modified polycarbonate. *Polymer* 1990, 31: 2267-2277
- 25 Lazzeri A and Bucknall CB. Dilational bands in rubber-toughened polymers. *J Materials Science* 1993, 28: 6799-6808
- 26 Dompas D and Groeninckx G. Toughening behavior of rubber-modified thermoplastic polymers involving very small rubber particles: 1. A criterion for internal rubber cavitation. *Polymer* 1994, 35(22): 4743-4749
- 27 Pawlak A, Galeski A and Rozanski A. Cavitation during deformation of semicrystalline polymers. *Progress in Polymer Science* 2014, 39: 921-958
- 28 Cheng C, Hiltner A, Baer E, et al. Cooperative cavitation in rubber-toughened polycarbonate. *J Materials Science* 1995, 30: 587-595
- 29 Krzeminski DE. Effects of one season of end-use exposure to collegiate American football outer shells. 2012. Unpublished work.
- 30 Krzeminski DE, Fernando BMD, Rawlins JW, et al. Quantifying the effects of accelerated weathering and linear drop impact exposures of an American football helmet outer shell material. *Proc IMechE Part P: J Sports Engineering and Technology* 2014, 228(3): 171-187
- 31 Krzeminski DE, Lippa NM, Rawlins JW, et al. Evaluation of supplemental football helmet protection. *J Athl Training* 2013, 48(3): S-190

- 32 Krzeminski DE, Fernando BMD, Rawlins JW, et al. Effects of solvent exposure on material properties and impact performance of an American football helmet outer shell material. *Procedia Engineering* 2014, 72: 508-514
- 33 Cheng C, Peduto N, Hiltner A, et al. Comparison of some butadiene-based impact modifiers for polycarbonate. *J Appl Polym Sci* 1994, 53: 513-525
- 34 Cheng C, Hiltner A, Baer E, et al. Deformation of Rubber-Toughened Polycarbonate: Microscale and Nanoscale Analysis of the Damage Zone. *J Appl Polym Sci* 1995, 55: 1691-1702
- 35 Loyens W and Groeninckx G. Ultimate mechanical properties of rubber toughened semicrystalline PET at room temperature. *Polymer* 2002, 43: 5679-5691
- 36 Loyens W and Groeninckx G. Rubber toughened semicrystalline PET: influence of the matrix properties and test temperature. *Polymer* 2003, 44: 123-126
- 37 Loyens W and Groeninckx G. Deformation mechanisms in rubber toughened semicrystalline polyethylene terephthalate. *Polymer* 2003, 44: 4929-4941
- 38 Lee CB and Chang FC. Toughening behavior of elastomer modified polycarbonates based on the J-Integral. *Polym Eng Sci* 1992, 32(12): 792-803
- 39 NOCSAE (ND) 001-13m14b. Standard test method and equipment used in evaluating the performance characteristics of protective headgear/equipment. National Operative Committee on Standards for Athletic Equipment 2013
- 40 NOCSAE (ND) 002-13m13. Standard performance specification for newly manufactured football helmets. National Operative Committee on Standards for Athletic Equipment 2013

- 41 Krzeminski DE, Fernando BMD, Lippa NM, et al. Effects of impact exposure and thermal annealing on mechanical properties of an American football helmet outer shell material. *Proceedings 37th Meeting American Society of Biomechanics* 2013
- 42 ASTM F1446-13. Standard test methods for equipment and procedures used in evaluating the performance characteristics of protective headgear. American Society for Testing and Materials International 2013
- 43 ASTM D792-13. Standard Test Methods for Density of Plastics by Displacement. American Society for Testing and Materials International 2013
- 44 Oliver WC and Pharr GM. An improved technique for determining hardness and elastic modulus using load and displacement sensing indentation experiments. *J Materials Research* 1992, 7(6): 1564-1583
- 45 ASTM D638-03. Standard test method for tensile properties of plastics. American Society for Testing and Materials International 2003
- 46 Rowson S, Duma SM, Greenwald RM, et al. Can helmet design reduce the risk of concussion in football? *J Neurosurgery* 2014, 120: 9190-922
- 47 Duma SM and Rowson S. Chapter 7: The Biomechanics of Concussion: 60 Years of Experimental Research. In: Slobounov SM and Sebastianielli (eds) *Concussions in Athletics: From Brain to Behavior*. 1st ed. New York: Springer, 2014, 115-137
- 48 Johnston JM, Ning H, Kim JE, et al. Simulation, fabrication and impact testing of a novel football helmet padding system that decreases rotational acceleration. *Sports Engineering* 2015, 18: 11-20

- 49 Post A, Oeur A, Hoshizaki B, et al. Differences in region-specific brain tissue stress and strain due to impact velocity for simulated American football impacts. *Proc IMechE Part P: J Sports Engineering and Technology* 2014, 228(4): 276-286
- 50 Krzeminski DE, Goetz JT, Janisse AP, et al. Investigation of linear impact energy management and product claims of a novel American football helmet liner component. *Sports Technology* 2011, 4(1-2): 65-76
- 51 Halkon B, Webster J, Mitchell S, et al. Development of a test methodology for the assessment of human impacts in sport. *Procedia Engineering* 2012, 34: 813-818
- 52 Viano DC and Halstead D. Change in size and impact performance of football helmets from the 1970s to 2010. *Ann of Biomed Eng* 2012, 40(1): 175-84
- 53 Chen K and Schweizer KS. Theory of Yielding, Strain Softening, and Steady Plastic Flow in Polymer Glasses under Constant Strain Rate Deformation. *Macromolecules* 2011, 44:3988-4000
- 54 Cheng S and Wang SQ. Elastic Yielding after Cold Drawing of Ductile Polymer Glasses. *Macromolecules* 2014, 47, 3661-3671
- 55 Robertson RE and Patel AM. The elastic, anelastic and plastic components of strain in the load-extension curve for bisphenol-a polycarbonate. *Polym Eng Sci* 1972, 12(5): 346-352
- 56 Zartman GD, Cheng SC, Li X, et al. How melt-stretching affects mechanical behavior of polymer glasses. *Macromolecules* 2012, 45: 6719-6732
- 57 Cheng S, Johnson L and Wang SQ. Crazing and strain localization of polycarbonate glass in creep. *Polymer* 2013, 54:3363-3369.

- 58 Klement JJ and Geil PH. Deformation and annealing behavior. II. Thick polyethylene terephthalate films. *J Macromolecular Science, Part B: Physics* 1971, 5(3), 535-558
- 59 Tant MR and Wilkes GL. Physical Aging Studies of Semicrystalline Poly(ethylene terephthalate). *J Appl Polym Sci* 1981, 26:2813-2825
- 60 Cassel B. How Tzero Technology Improves DSC Performance Part I: Flat Baselines and Glass Transition Measurements. TA Instruments, Inc.
- 61 Goschel U. Chapter 6: Structure Development and Mechanical Behavior During Uniaxial Drawing of PET. In: Fakirov S (ed) Handbook of Thermoplastic Polyesters: Homopolymers, Copolymers, Blends, and Composites. 1st ed Weinheim, FRG: Wiley, 2002, pp.289-316
- 62 Lu XF and Hay JN. Crystallization orientation and relaxation in uniaxially drawn poly(ethylene terephthalate). *Polymer* 2001, 42:8055-8067
- 63 Wang ZG, Hsiao BS, Sauer BB, et al. The nature of secondary crystallization in poly(ethylene terephthalate). *Polymer* 1999, 40:4615-4627
- 64 Morbitzer L, Kranz D, Humme G, et al. Structure and Properties of ABS Polymers. X. Influence of Particle Size and Graft Structure on Loss Modulus Temperature Dependence and Deformation Behavior. *J Appl Polym Sci* 1976, 20:2691-2704
- 65 Morbitzer L, Humme G, Ott KH, et al. Struktur und Eigenschaften von ABS-Polymeren. *Die Angewandte Makromolekulare Chemie* 1982, 108:123-140
- 66 Illers KH and Breuer H. Molecular motions in polyethylene terephthalate. *J Colloid Science* 1963, 18, 1-31

- 67 Xia Z, Sue HJ, Hsieh AJ, et al. Dynamic Mechanical Behavior of Oriented Semicrystalline Polyethylene Terephthalate. *J Polymer Science: Part B: Polymer Physics* 2001, 39:1394-1403
- 68 Bedoui F and Guigon M. Linear viscoelastic behavior of poly(ethylene terephthalate) above T_g amorphorous viscoelastic properties vs crystallinity: Experimental and micromechanical modeling *Polymer* 2010, 51:5229-5235.
- 69 Nguyen TL, Bedoui F, Mazeran PE, et al. Mechanical Investigation of confined Amorphous Phase in Semicrystalline Polymers: Case of PET and PLA. *Polym Eng Sci* 2015, 55(2), 397-405
- 70 Etienne S, Lamorlette C, and David L. Molecular mobility and structural state relationship in amorphous polymers. *J Non-Crystalline Solids* 1998, 235, 628-634
- 71 Munch E, Pelletier JM, and Vigier G. Increase in Molecular Mobility of an Amorphous Polymer Deformed Below T_g. *J Polymer Science: Part B: Polymer Physics* 2008, 46, 497-505
- 72 Lin CS, Ayre DS, and Bucknall CB. A dynamic mechanical technique for detecting rubber particle cavitation in toughened plastics. *J Materials Science Letters* 1998, 17: 669-671
- 73 Bucknall CB, Rizzieri R and Moore DR. Detection of incipient rubber particle cavitation in toughened PMMA using dynamic mechanical tests. *Polymer* 2000, 41:4140-4156
- 74 Bucknall CB. Cavitation of Rubber Particles Dispersed in a Rigid Polymer Matrix. *Proceedings to 2004 SEM X International Congress & Exposition on Experimental & Applied Mechanics*, 2004

- 75 Bauwens-Crowet C and Bauwens JC. The relationship between the effect of thermal pre-treatment and the viscoelastic behavior of polycarbonate in the glassy state. *J Materials Science* 1979, 14, 1817-1826
- 76 Trznadel M, Pakuta T, and Kryszewski M. The influence of internal stresses on viscoelastic properties of oriented glassy polymers. *Polymer* 1988, 29, 619-625
- 77 Zhou Z, Chudnovsky A, Bosnyak CP, and Sehanobish K. Cold-Drawing (Necking) Behavior of Polycarbonate as a Double Glass Transition. *Polym Eng Sci* 1995, 35(4), 304-309
- 78 Bucknall CB, Rizzieri R, and Moore DR. Detection of cavitation in rubber phase of rubber toughened poly(methyl methacrylate) using thermal contraction measurements. *Plastics, rubber, and composites* 2001, 30(4):183-189
- 79 Miller GW. Thermal Analyses of Polymers. XIII. Crystalline Character of the 70 °C Transition of Poly(ethylene terephthalate). *J Polymer Science: Polymer Physics* 1975, 13:1831-1844.
- 80 Kato T and Kambe H. A thermomechanical investigation of highly cold-drawn polycarbonate. *J Appl Polym Sci* 1978, 22:1767-1774
- 81 Foreman J, Sauerbrunn SR, and Marcozzi CL. Exploring the Sensitivity of Thermal Analysis Techniques to the Glass Transition. TA Instruments, Inc.
- 82 Miller GW. Thermal Analyses of Polymers. VII. Calorimetric and Dilatometric Aspects of the Glass Transition. *J Appl Polym Sci* 1971, 15: 2335-2348.
- 83 Belaribi C, Marin G, and Monge P. Viscoelastic and thermal behavior of partially compatible polymer blends polycarbonate/tetramethylpolycarbonate. *European Polymer Journal* 1986, 22(6):481-485

- 84 Jaffe M. Chapter 7: Fibers. In: Turi E. (ed) Thermal Characterization of Polymeric Materials. 1st ed. New York: Academic Press, Inc, 1981, pp.709-792
- 85 Bair HE, Akinay AE, Menczel JD, et al. Chapter 4: Thermomechanical analysis (TMA) and thermodilatometry (TD). In: Menczel JD and Prime RB. (eds) Thermal Analysis of Polymers: Fundamentals and Applications. 1st ed. Hoboken, NJ: John Wiley & Sons, 2009, pp. 319-386.
- 86 Choy CL, Ito M, and Porter RS. Thermal Expansivity of Oriented Poly(ethylene terephthalate). *J Polymer Science: Polymer Physics* 1983, 21:1427-1438
- 87 Pereira JRC and Porter RS. Extrusion drawn amorphous and semi-crystalline poly(ethylene terephthalate): 3. Linear thermal expansion analysis. *Polymer* 1984, 25:869-876
- 88 Hinrichsen G, Luedecke W, and Springer H. Thermal-mechanical analysis of drawn poly(ethylene terephthalate) and poly(amide) films. *Thermochimica Acta* 1983, 61: 161-168
- 89 Karagiannidis PG, Stergiou AC, and Karayannidis GP. Study of crystallinity and thermomechanical analysis of annealed poly(ethylene terephthalate) films. *European Polymer Journal* 2008, 44:1475-1486
- 90 Boyce MC and Haward RN. Chapter 5: The post-yield deformation of glassy polymers. In *The Physics of Glassy Polymers*, 2nd ed.; Haward RN, Young RJ, Eds.; Chapman and Hall: London, 1997: 213-293

CHAPTER VI

SUMMARY AND FUTURE WORK

Summary

The purpose of this dissertation is to gain a greater scientific understanding of the changes in functional material properties and impact performance of an American football helmet outer shell material under expected service life exposure conditions, through the following five objectives:

Objective 1 (Chapters II-V): develop a linear drop test impact protocol to employ expected on-field impact conditions to American football components and shell-liner helmet surrogates

Objective 2 (Chapter II): define the linear impulse and compression behavior of a novel American football helmet liner component

Objective 3 (Chapter III): quantify the effects of accelerated weathering exposure on the functional material properties and impact performance of an American football outer shell material

Objective 4 (Chapter IV): (a) develop a method to accurately replicate solvent exposure during the reconditioning painting process and (b) quantify shifts in functional material properties and impact performance of an football outer shell material

Objective 5 (Chapter V): quantify the effects of repetitive linear drop exposures and impact-induced stress-whitening on the functional material properties of an football outer shell material

In Chapter II, the linear impulse and compression behavior of a novel helmet liner component was defined across increasing impact velocities. The investigation of impact energy management served to further define and substantiate published findings and product claims. It was postulated that the addition of the foam-filled pad to the liner improved the attenuation of linear impact energy and increased velocity-specific durability. Additionally, an instrumented drop test setup was substantiated to investigate linear impact attenuation performance.

In Chapter III, the effects of 480 hours of accelerated weathering across chemical, physical, thermal, and mechanical properties of an American football helmet outer shell material were quantified. Linear impact performance was analyzed with a novel protocol attempting to employ expected on-field impact conditions with the use of a plaque-foam helmet surrogate. It was postulated that laboratory exposure to UV light, oxygen, moisture, and elevated temperatures induced molecular degradative bi-products and physical aging up to ~1% into the plaque thickness which led to altered aesthetic properties, chemi-crystallization, and an increased resistance to surface indentation and tensile deformation. Statistically significant results identified a battery of diagnostic tools to characterize the weathering-induced degradation of a helmet-grade PC-PET blend material, and the comprehensive approach was suggested towards the evaluation of additional service life exposures as well as the examination of on-field deterioration of full helmet outer shells.

In Chapter IV, a spraying method to accurately represent solvent exposure during the reconditioning painting process was substantiated. The effects of increased exposure levels of n-Butyl acetate across physical, thermal, and mechanical properties of an

American football helmet outer shell material were quantified. It was postulated that solvent-induced plasticization, crystallization, and stress-cracking of up to ~3% into the plaque thickness led to an increase in surface porosity which scattered light and decreased tensile properties. Statistically significant results identified a battery of diagnostic tools to characterize the solvent-induced degradation of outer shell material. Linear impact performance was analyzed with an adapted protocol attempting to better replicate on-field impact conditions (compared to Chapter III).

In Chapter V, the effects of repetitive linear drop exposures and impact-induced stress-whitening across physical, thermal, and mechanical properties of an American football helmet outer shell material were quantified. Changes in linear impact performance were quantified with a further engineered protocol attempting to more accurately replicate on-field impact conditions (compared to Chapter IV). It was postulated that impact exposure induced rubber-toughener (RT) cavitation that generated voids via delamination at the RT-matrix interface at up to ~40-45% into the plaque thickness which led to rings of stress-whitening, strain-induced crystallization, increased butadiene RT density, and shifts surface modulus and tensile properties. Statistically significant results identified a battery of diagnostic tools to characterize material property changes for impact-induced degradation of rubber-toughened outer shell materials. It is hypothesized that this is the first time surface and tensile mechanical properties of a non-fractured, stress-whitened rubber-toughened material have been reported.

Overall, a step-wise progression of analysis to concurrently quantify and understand changes in material properties at the molecular, microscopic, and macroscopic levels was demonstrated by evaluating service life exposures of weathering, solvent, and

repetitive impacts. Changes across chemical, physical, thermal, and mechanical properties were evaluated following individual laboratory exposures to 480 hours of accelerated weathering, increasing intensities of n-Butyl acetate solvent, and repetitive linear plaque-foam impacts. This dissertation preliminarily substantiated (i) an engineered drop test setup attempting to accurately replicate on-field impact conditions to investigate linear impact attenuation performance, and (ii) polymer techniques and protocols that could elucidate the rates and degrees of material degradation as a function treatment duration and intensity.

Future Work Introduction

Future work extending from this dissertation has the potential to continue in several directions: (I) investigation of additional treatment conditions to helmet-grade plaques, (II) substantiation of additional quantitative techniques to evaluate shifts in functional material properties, (III) characterization of impact performance of additive helmet technologies, and (IV) monitoring *in situ* degradation of full helmet outer shells. The preliminary and pilot research completed across these sections will be discussed.

For Section I, the next step from the research in Chapter V is to explore the effects of additional treatment conditions to helmet-grade plaque materials. The thermal annealing of stress-whitened material was explored to determine the potential for aesthetic recovery and thermo-mechanical rejuvenation. The long-term goal is to validate an annealing protocol that could be potentially introduced into current helmet outer shell reconditioning practices to provide greater helmet lifespan consistency.

For Section II, extensive work was performed to substantiate the use of traditional polymer science and engineering techniques to characterize the effects of degradation to

service life exposures. Therefore, the potential for additional quantitative techniques must be continually investigated. Pilot work regarding the use of infrared thermography will be described.

For Section III, a novel impact protocol was continuously engineered and adapted in attempt to accurately employ on-field impact conditions. Investigation of linear impact attenuation using a plaque-foam helmet surrogate has the potential to expand into the evaluation of after-market technologies for American football helmets. Preliminary study of a supplemental football helmet padding protection system and its individual components was completed via and the results are detailed herein.

For Section IV, the next step from the research in Chapters III-V is to expand beyond the controlled setting of the laboratory and into the natural end-use environment. New research must examine on-field changes in functional properties of constituent helmet materials and explore how polymeric degradation will lead to changes in helmet outer shell function throughout its lifecycle. The ability to monitor degradation of helmet outer shells in real-time may lead to knowledge that can be leveraged for the development of new technologies, tools, equipment, and policies aimed towards greater helmet lifespan consistency, and the potential reduced risk of head injury.

Thermal Annealing

Introduction

The investigation in Chapter V of this dissertation thoroughly quantified the degradative effects of impact-induced stress-whitening on the functional properties of helmet-grade materials. Visual inspection of Impacted material following DMA testing (up to 180 °C) and TMA testing (up to 235 °C) revealed that the stress-whitening visibly

present at pre-test was no longer present in the post-test condition. A review of the scientific literature reveals that thermal annealing close to a material's glass transition temperature (T_g) is reported to rejuvenate its thermo-mechanical history (1, 2).

The elimination of mechanically-induced stress-whitening in semicrystalline thermoplastics has been reported (3-5). However, studies of thermal treatments of impact-modified PC and PET do not include assessments of material properties following mechanical testing (6, 7). Therefore, we aim to elucidate the origin of the impact-induced stress-whitening disappearance observed post-test in DMA and TMA specimens and explore the potential for physical, thermal, and mechanical property recovery. The purpose of this work was to investigate the effects of impact exposure and thermal annealing on the (i) impact performance, (ii) colorimetric, tensile, and surface mechanical properties of an American football helmet outer shell material. This study explored two hypotheses: thermal annealing will (1) visually and colorimetrically erase impact-induced stress-whitening, and (2) will rejuvenate impact performance and mechanical properties.

Experimental

Helmet-grade plaques (N=20) (material details described previously in Chapters III-V) were randomly assigned into four material conditions (n=5): (1) Non-impacted, (2) Non-impacted/Annealed, (3) Impacted, and (4) Impacted/Annealed (Figure 49). Impacted plaques underwent a treatment of 12 repetitive impacts that matched the linear drop test protocol described Chapter V. Impact performance was measured with an additional 13th trial and results were analyzed via an independent t-test comparing Impacted and Impacted/Annealed plaques. Overall, 190 impacts were performed.

Annealed plaques underwent a thermal annealing treatment in a convection oven at 175 °C for 5 min. Plaques were removed and air cooled.

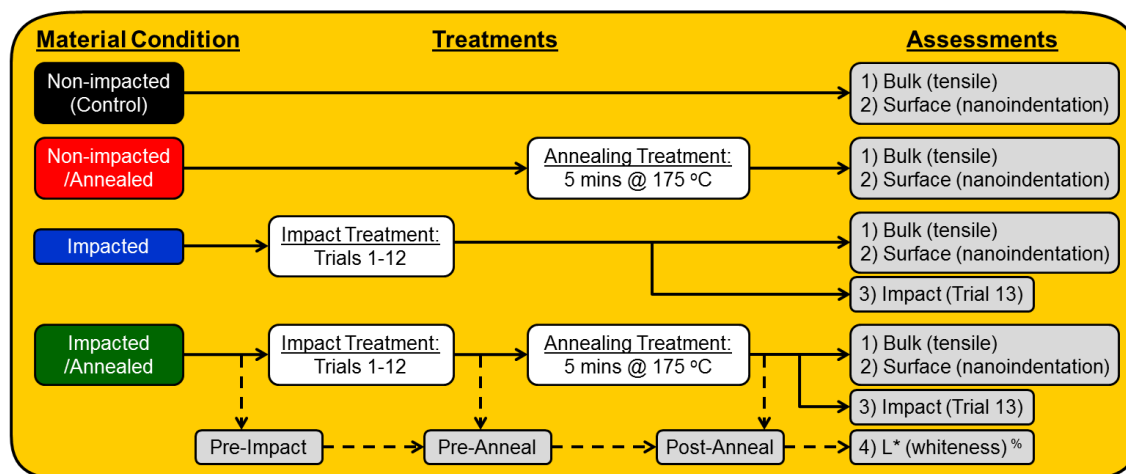


Figure 49. Experimental schematic showing treatments and assessments (n=5) across material conditions. (%= Colorimetric test).

Surface color change was quantified via L* whiteness following the protocol as described in Chapter V and analyzed on Impacted/Annealed plaques via a one-way repeated measures ANOVA with 3 levels: (1) Pre-impact (Pre-Trial 1), (2) Pre-anneal (Post-Trial 12), and (3) Post-anneal (Post-Trial 12) (Figure 49).

Tensile mechanical properties were measured following the protocol as described in Chapter V. Modified ASTM-D638 Type I specimens for Impacted/Annealed were harvested directly from plaques whereby marks were placed around the impact-induced rings of whitening to preserve their location after the thermal annealing treatment (Figure 50b). The dependent variables examined were Young's modulus, yield stress, and ultimate tensile stress (UTS). Results were analyzed via three separate one-way ANOVAs with 4 levels (material condition).

Surface mechanical properties were quantified using load-controlled quasi-static nanoindentation at pre-selected loads of 500, 1000, 1500, 2000, and 2500 μN . Dependent

variables examined were depth of surface penetration and reduced modulus. Results were analyzed via a 4 between (material condition) x 5 between (applied load) ANOVA.

Statistical analyses were performed using Statistical Package for Social Sciences software. For all analyses, alpha level was set a priori at $\alpha = 0.05$. Post-hoc analyses were performed via Tukey HSD tests and effect sizes were calculated using Cohen's d for an independent t-test and Cohen's f for an ANOVA.

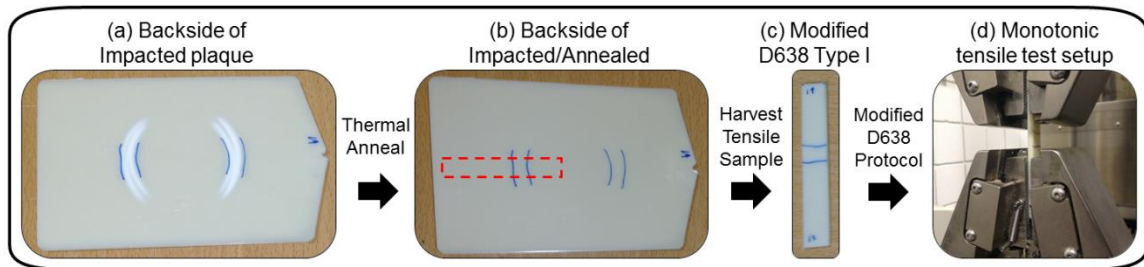


Figure 50. (a) Backside of Impacted plaque after 12 trials, displaying impact-induced rings of whitening. (b) Backside of Impacted/Annealed plaque showcasing that annealing visually erased whitening. Dashed box: Location of harvested tensile sample. (c) Tensile sample harvested from Impacted/Annealed plaque. (d) Tensile test setup with annealed rings of whitening placed between clamps.

Results and Discussion

Numerical results are reported as mean \pm one standard deviation, unless otherwise noted.

Visual Inspection and Colorimetric Characterization

Each impact test induced visible whitening to the plaque (Figure 50a). The visible disappearance of whitening along with a significant difference in mean L^* ($F_{2,8}=563.38$, $p<0.05$, $f=11.91$) (Figure 51a) indicated that the thermal annealing treatment adequately erased the impact-induced whitening. L^* values were 78.4 ± 0.1 , 87.4 ± 0.4 , and 79.1 ± 0.8 for Pre-impact (Pre-Trial 1), Pre-anneal (Post-Trial 12), and Post-anneal (Post-Trial 12), respectively.

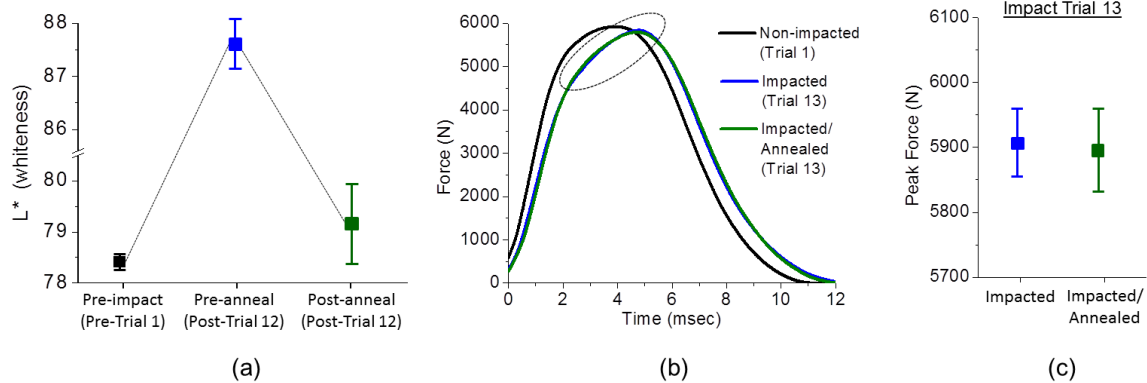


Figure 51. (a) L^* whiteness values across Pre-impact, Pre-anneal, and Post-anneal conditions ($\# = p < 0.05$). (b) Smoothed force-time curves of plaque-foam systems. (c) Trial 13 peak force for Impacted and Impacted/Annealed plaques.

The change in characteristic curve shape between Non-impacted and Impacted plaques (Figure 51b) along with a significant difference in mean peak force between trials 1 and 12 ($t=7.93$, $p<0.05$, $d=1.47$) indicated the impact treatment induced a change in plaque impact performance. The absence of significance in mean peak force along with no qualitative change in curve shape between Impacted and Impacted/Annealed (Figure 51c) suggested that the annealing treatment did not alter nor rejuvenate the impact energy management of a plaque with an impact history of 12 repetitive trials.

Tensile Mechanical Properties

The characteristic stress-strain curve shapes across material conditions were observed to be equivalent (Figure 52, left). Significant differences observed for yield stress ($F_{3,16}=6.93$, $p<0.05$, $f=1.32$) and UTS ($F_{3,16}=21.21$, $p<0.05$, $f=2.30$) indicated both the impact and annealing treatments altered bulk tensile properties (Table 24). Post-hoc analysis of yield stress revealed that: (i) the impact treatment caused softening, (ii) the annealing treatment on Non-impacted plaques caused softening, and (iii) the annealing treatment on Impact plaques elicited recovery. Post-hoc analysis of UTS revealed that (i) the impact treatment caused hardening and (ii) the annealing treatment on Impact plaques

elicited recovery. Further analysis revealed reductions in Young's modulus (observed trend) when comparing Annealed and Non-annealed conditions for a given impacted condition, thus further suggesting thermal annealing softened the material.

Visual inspection of tensile samples post-test revealed all Impacted specimens preferentially yielded at the whitened area (Figure 52, right), whereas Impacted/Annealed specimens did not preferentially yield at the whitened area that existed prior to anneal. In summary the yield stress and UTS results, as well as the observed preferential yielding behavior, suggested that the thermal annealing treatment potentially induced tensile mechanical property rejuvenation in Impacted plaque material.

Table 24

Tensile properties across material conditions

Material Condition	Young's modulus (MPa)	yield stress (MPa)	ultimate tensile stress (MPa)
Non-impacted	955.5 ± 27.6	56.2 ± 0.3 ^{1, 2}	44.0 ± 0.2 ⁵
Non-impacted/Annealed	920.7 ± 26.7	55.0 ± 0.8 ^{1, 3}	43.4 ± 1.9 ^{6, 8}
Impacted	934.6 ± 21.6	55.3 ± 0.3 ²	45.8 ± 0.2 ^{5, 6, 7}
Impacted/Annealed	910.9 ± 32.6	56.5 ± 0.8 ³	44.7 ± 0.3 ^{7, 8}

* Matching superscript number denotes the Tukey HSD post-hoc combination was statistically different ($p < 0.05$)

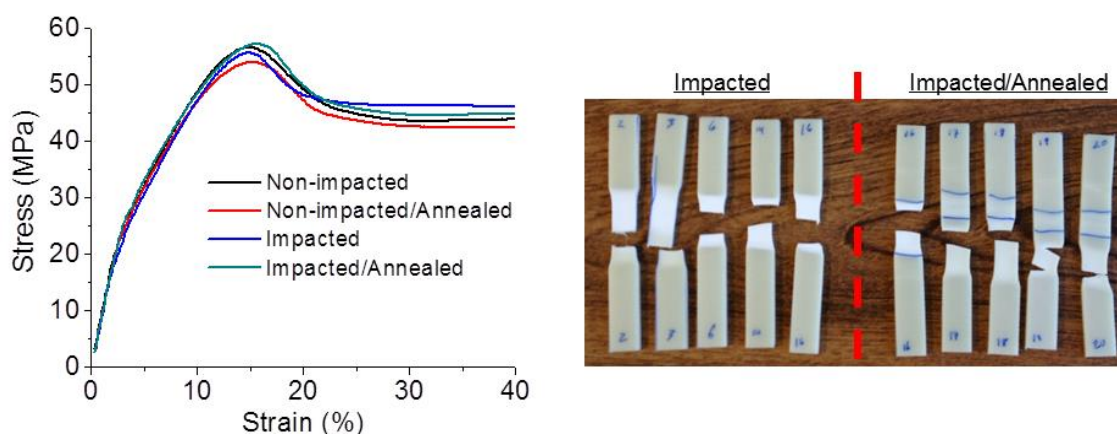


Figure 52. (left) Stress-strain curves across material conditions. (right) Impacted and Impacted/Annealed tensile samples post-test showcasing the differential preferential yielding behavior via location of whitening.

Nanoindentation results suggested that the thermal annealing treatment altered surface mechanical properties up to a depth of $\sim 1.0\ \mu\text{m}$. Differences were observed in reduced modulus between material conditions ($F_{3,80}=4.35$, $p<0.05$, $f=0.39$). Post-hoc analysis of reduced modulus revealed that Annealed material was less resistant to deformation than Non-annealed for a given impacted condition (Figure 53).

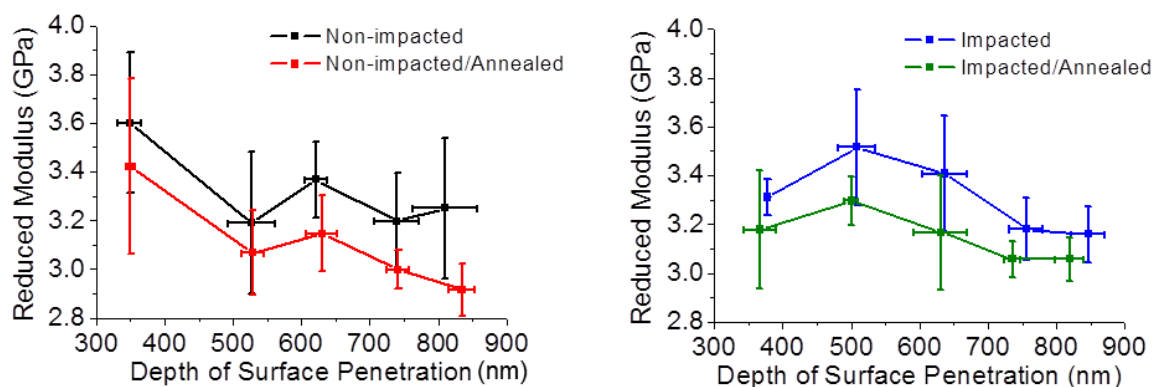


Figure 53. Reduced modulus as a function of depth of surface penetration for (left) Non-impacted and (right) Impacted material conditions.

Conclusions

This study tested the hypotheses that thermal annealing above the T_g of the outer shell helmet-grade material will (1) erase impact-induced stress-whitening and (2) rejuvenate the impact performance and mechanical properties of impact-degraded material. The thermal annealing of Impacted material (1) erased impact-induced rings of whitening, (2) failed to alter plaque impact performance, (3) elicited that potential rejuvenation of tensile properties and yielding behavior, and (4) reduced the surface modulus. As a result, we postulate that thermal annealing above T_g aesthetically recovered the helmet-grade plaque, and potentially rejuvenated the thermo-mechanical history of the American football outer shell material.

Our findings warrant a more comprehensive investigation of the effects of thermal annealing on the functional properties of helmet-grade materials. Future work should aim to: (1) incorporate additional physical and thermal property techniques to quantify stress-whitening – such as SEM, MDSC, DMA, and TMA substantiated in Chapter V – and explore if degradative shifts in measured properties recover back to Non-impacted values, (2) vary the duration and temperature of the thermal annealing treatment to determine the rate and extent of material rejuvenation, and (3) explore the effects of annealing full helmet outer shells as a potential way to aesthetically recover helmet systems and potentially mitigate the risk of head injury by providing greater helmet life-span consistency.

Infrared Thermography

Thermal properties are also measureable at the bulk scale using infrared thermography (IRT). Heat is essentially the infrared light emitted from an object and IRT captures the energy and displays an image of spatial temperature distribution. Surface temperature changes of an American football helmet outer shell material exposed to a linear drop impact were quantified using IRT. A single helmet-grade plaque, as previously described in Chapters III-V, was impacted using an instrumented drop tower at 3.0 m/sec under ambient conditions with a 5.0 kg drop mass assembly containing a 44 kN load cell tup and 38.1 mm diameter rounded steel drop dart. The steel anvil had a 76.2 mm cutout and fixture clamps such that deflection of the plaque occurred. The IRT measurement was conducted on the plaque backside, which was visible via the anvil cutout. Results revealed (1) a focal maximum temperature increase that matched the drop dart (Figure 54, left) and (2) a step-wise increase from ambient temperature ($\sim 24^{\circ}\text{C}$) to

over 35 °C in less than 0.5 secs (Figure 54, right) due to the drop mass coming to a rest.

Future work should (i) monitor and characterize changes in bulk temperature response as a possible predictive tool of helmet-grade material degradation and (ii) incorporate IRT and high speed video to compare the resultant area of impact-induced stress-whitening.

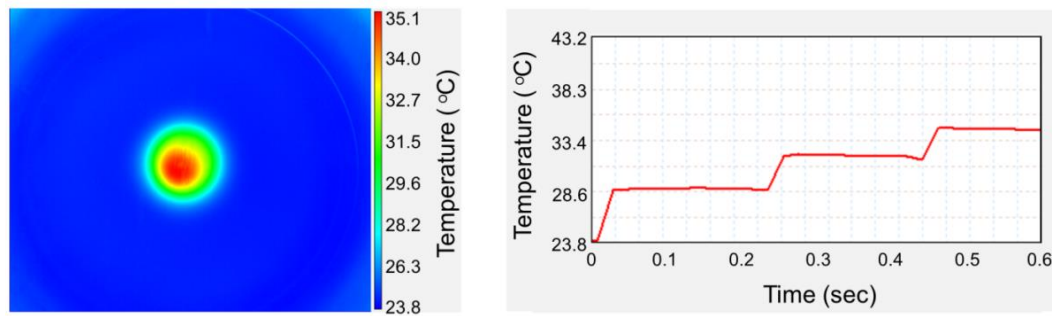


Figure 54. IRT image showcasing the (left) focal maximum temperature increase and (right) step-wise increase versus time of the backside of an impacted plaque.

Additive Helmet Technology

Introduction

Increasing padding thickness is generally associated with a reduction in peak force and an extension of impact event duration (8). Thus, additive padding systems are available as aftermarket enhancements for protective head gear and are aimed towards the abatement of sports-related concussion. Currently, standards do not exist to direct and assess the design, functionality, or validity of such systems (9, 10). However, popularity of supplemental technology usage among athletes has rapidly increased without peer-reviewed scientific information to address the clinical significance of such products (11).

EXO Skeleton® PADS (Unequal Technologies, Kennett Square, PA)

supplemental football helmet padding protection system is composed of a Kevlar® fiber mesh adhered to a thin polyurethane foam (PU Foam) layer (Figure 55). Product claims include substantial additive effects to football helmet performance parameters via

reduction of Severity Index (SI) and G-Force (up to 50% SI and/or 25% G), which are purported to reduce the risk of the brain injury of concussion (12). However, neither product systems nor components have been validated in the peer-reviewed literature. Therefore, the purpose of this preliminary study is to characterize and evaluate the impact performance of a supplemental helmet protection system.

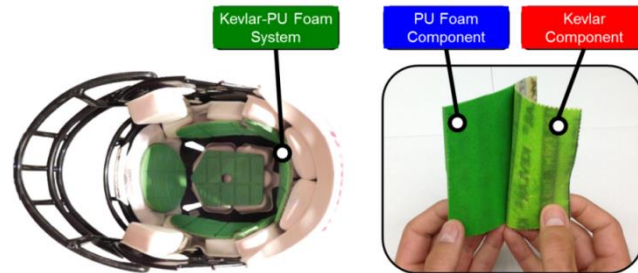


Figure 55. (left) Recommended placement of the Kevlar-PU Foam additive technology in a football helmet (Kevlar facing towards inner liner). (right) Separation of the system showcasing the PU Foam padding component and Kevlar fiber mesh component.

Experimental

Kevlar-PUFoam was randomly selected and manually separated (Figure 55, right) into Kevlar and polyurethane foam (PU Foam) components to produce four sample conditions ($n=3$): (1) Control, (2) Kevlar, (3) PU Foam, and (4) Kevlar-PU Foam. Testing was performed across two impact setups: (i) steel anvil only and (ii) a plaque-foam helmet surrogate with 25.4 mm thick VN600 foam (Figure 56). Overall, eight total groups were tested ($n=3$; $N=24$) using an instrumented drop tower. Impacts were performed at 5.5 m/sec under ambient conditions against a flat steel anvil with a 4.9 kg drop mass assembly containing a 44 kN load cell tup and 38.1 mm diameter PU drop dart (150M medium grade, Lixie Hammers, Central Falls, RI).

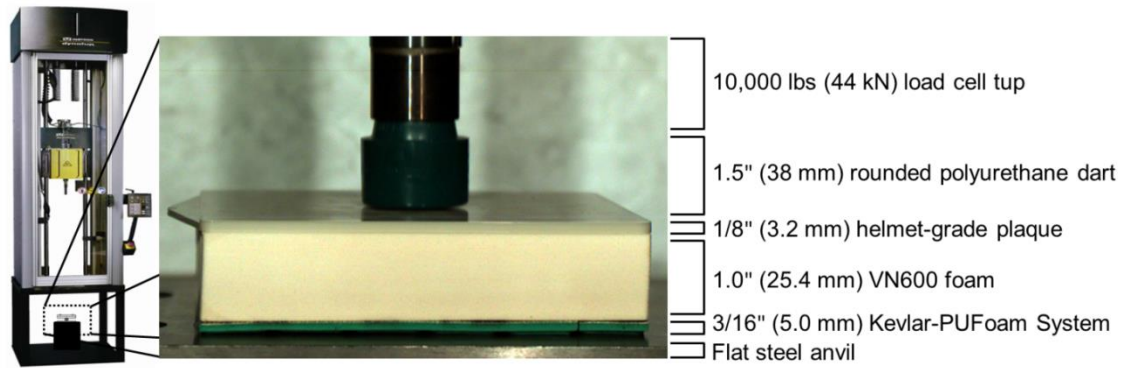


Figure 56. Instrumented drop tower with plaque-foam helmet surrogate atop Kevlar-PU Foam at pre-impact.

Peak impact force was analyzed via two separate (impact setup) one-way ANOVAs with 4 levels (sample condition). For all statistical analyses, alpha was set a priori to $\alpha=0.05$. Post-hoc analyses were performed via Tukey HSD tests and effect sizes were calculated using Cohen's f and Cohen's d . Additionally, percent reduction in peak impact force (compared to control) was calculated and compared between impact setups. Severity Index (SI) was calculated and compared across sample conditions, but only for Plaque-foam impact setup and reported as mean percent reduction (compared to control).

Results

Compared to Control, the force-time curve shape was reduced in curve height and extended in duration across all conditions, with PU Foam and Kevlar-PU Foam appearing equivalent (Figure 57, left). Significant main effects were observed for peak impact force ($F_{3,8}=28.86$, $p<0.05$, $f=3.28$) (Table 25). Post-hoc analysis revealed: (i) Control was different than Kevlar ($d=3.56$), PU Foam ($d=6.77$), and Kevlar-PU Foam ($d=7.65$); and (ii) Kevlar was different than PU Foam ($d=3.21$) and Kevlar-PU Foam ($d=4.08$).

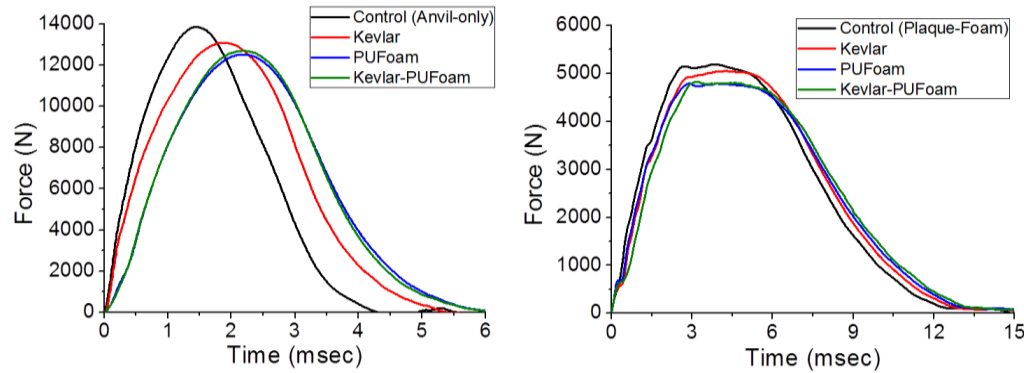


Figure 57. Smoothed force-time curves of single impacts across sample conditions for (left) Anvil-only setup and (right) Plaque-foam setup.

Compared to the Control, force-time curve shape reduced in curve height and extended in event duration across all conditions, with PU Foam and Kevlar-PU Foam appearing equivalent (Figure 57, right). Significant main effects were observed for peak impact force ($F_{3,8}=42.79$, $p<0.05$, $f=3.99$) (Table 26). Post-hoc analysis revealed: (i) Control was different than Kevlar ($d=4.13$), PU Foam ($d=8.45$), and Kevlar-PU Foam ($d=9.07$); and (ii) Kevlar was different than PU Foam ($d=4.32$) and Kevlar-PU Foam ($d=4.94$). Additionally, percent reduction in mean SI was equivalent for PU Foam and Kevlar-PU Foam, while Kevlar was less than PU Foam and Kevlar-PU Foam.

Table 25

Impact performance parameters across sample conditions for anvil-only setup

Sample Condition	Peak Impact Force (N)	% Reduction in Peak Impact Force
Control	$13,975 \pm 245$ ^{1, 2, 3}	-
Kevlar	$13,345 \pm 205$ ^{1, 4, 5}	4.5%
PU Foam	$12,779 \pm 181$ ^{2, 4}	8.6%
Kevlar-PU Foam	$12,624 \pm 145$ ^{3, 5}	9.7%

* Matching superscript number denotes the Tukey HSD post-hoc combination was statistically different ($p<0.05$)

Table 26

Impact performance parameters across sample conditions for plaque-foam setup

Sample Condition	Peak Impact Force (N)	% Reduction in Peak Impact Force	% Reduction in Severity Index
Control	5340 \pm 47 ^{1, 2, 3}	-	-
Kevlar	5093 \pm 89 ^{1, 4, 5}	4.6%	4.2%
PU Foam	4835 \pm 41 ^{2, 4}	9.5%	7.0%
Kevlar-PU Foam	4798 \pm 38 ^{3, 5}	10.1%	7.2%

* Matching superscript number denotes the Tukey HSD post-hoc combination was statistically different ($p < 0.05$)

Discussion and Conclusions

Similar magnitudes of performance between impact setups specific to % reduction in peak impact force (Table 25 and 26) indicated impact attenuation provided by the additive components was maintained, and the addition of a plaque-foam helmet surrogate system did not confound impact performance. Addition of the Kevlar-PU Foam system and its individual components to the helmet surrogate each reduced peak impact force and SI, thus supporting basic product claims (12). However, no statistical differences were found between the PU Foam with or without the Kevlar component, which revealed that the foam component served as the primary linear, compressive impact management mechanism. Overall, this work substantiated our impact setup to evaluate the impact performance of additive helmet technologies with a plaque-foam helmet surrogate.

Monitoring in situ Degradation

Introduction

Throughout each season and across the helmet lifespan, exposure to cyclic environmental conditions and impact events serve to degrade material properties over time. Though helmets may still register below skull fracture thresholds, material property degradation may translate into helmets that leave athletes at a higher risk for concussion.

In fact, the known reduction in protective capacity of football helmet systems has led to a self-adopted industry change whereby a policy has limited the age limit regarding the outer shell component to ten years (Fisher_2011). However, the degree and rate of impact performance deterioration of American football helmet components and their constituent materials is not clearly understood. To date, no scientific information is available to detail the specific environmental effects of typical helmet use. The current analyses are devoid of assessments of material property changes of helmet grade polymers under on-field environments.

In situ helmet degradation

In order to monitor helmet systems throughout their lifetimes, non-destructive methods must be implemented to ensure helmet performance is not altered by the measurement. Spectroscopic and colorimetric methods were shown in Chapter III to successfully track accelerated weathering-induced degradation. Our hypothesis was that chemical changes detectable with ATR-FTIR and yellowing index (YI) would occur via exposure to on-field environmental conditions, specifically outdoor weathering. Preliminary work first compared helmet-grade plaques exposed to 480 hrs of accelerated weathering (AW) (see Chapter III) to natural weathering (NW) during the Spring of 2012 in Hattiesburg, MS. After 125 days of natural weathering, ATR-FTIR results revealed similar shifts in polymer functional groups between weathering groups (Figure 58). The reduction in spectral peaks at 2925 and 2855 cm^{-1} represented a loss in alkyl content relative to initial material composition, and the concurrent band broadening at 1720 cm^{-1} accompanied with a subtle shoulder formation around 1690 cm^{-1} represented increase carbonyl linkage concentrations. Colorimetric results revealed a comparable increase in

YI between weathering groups with values of 26.3 ± 0.2 , 30.8 ± 0.4 , and 29.7 ± 0.4 for Non-weathered, AW, and NW conditions, respectively.

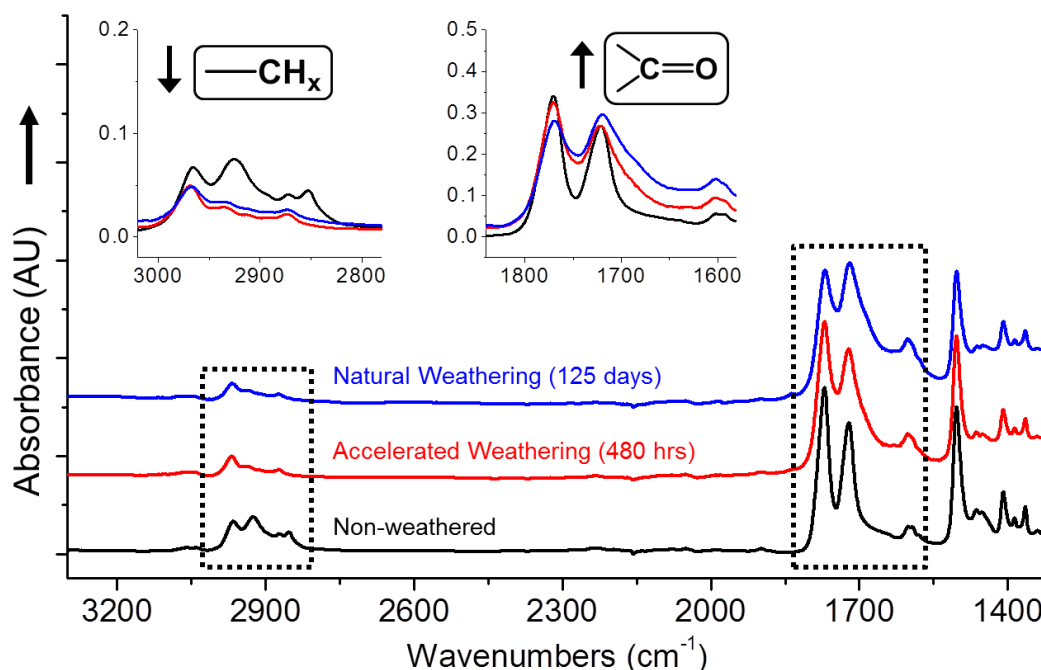


Figure 58. Full ATR-FTIR spectra of a helmet-grade plaque comparing Non-weathered Accelerated Weathering, and Natural Weathering conditions. Inset spectra showcase the differential across weathering conditions specific to alkyl composition (\downarrow $-\text{CH}_x$) at 3000-2800 cm^{-1} and carbonyl formation (\uparrow $-\text{C}=\text{O}$) at 1800-1600 cm^{-1} .

As a result of the observed differences due to outdoor weathering in helmet-grade plaques, pilot work was conducted to monitor brand new full helmet systems outfitted to the University of Southern Mississippi football team for the 2012 Fall season. Randomly selected Riddell and Schutt helmet outer shells were characterized using YI and ATR-FTIR (Figure 59, left) before use during the pre-season in July 2012 and post-season in January 2013 (prior to helmet reconditioning). Colorimetric results revealed similar YI between helmet groups at pre-season with values of 130.3 ± 0.4 and 129.6 ± 0.4 for Riddell and Schutt, respectively. For both YI and ATR-IR results, analysis revealed no differences between pre-season and post-season. However, the use of ATR-FTIR and CIELAB as non-destructive methods to analyze full outer shells was substantiated.

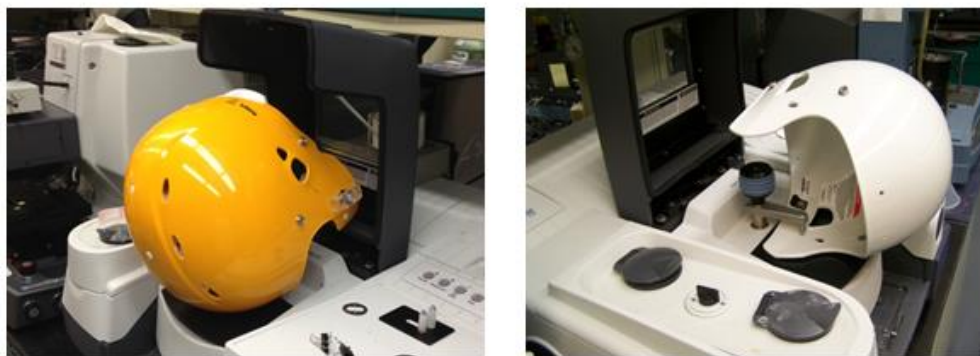


Figure 59. Off-the-shelf football helmet outer shells from (left) Riddell and (right) Xenith fixtured into an ATR-FTIR spectrometer.

The damage-free characterization of Riddell and Schutt helmets prompted further analysis of additional off-the-shelf outer shells (Figure 59, right). Results revealed differences in alkyl content ($3000\text{--}2800\text{ cm}^{-1}$) and carbonyl concentrations ($1800\text{--}1600\text{ cm}^{-1}$) between Xenith, Schutt, Riddell, and Rawlings helmet manufacturers (Figure 60). The observed differences in chemical compositions further demonstrated the ability to monitor *in situ* helmet degradation across multiple helmet systems.

Water contact angle measurements were also performed on helmet shells at pre-season and post-season time points. Our hypothesis was that chemical changes to the outer shell via exposure to on-field environmental conditions would alter the hydrophobicity of the surface material. A droplet of deionized water was pipetted onto the top of helmet shell and a high definition photograph was taken with a black background (Figure 61a). The photograph was imported for analysis into DropSnake Software (Figure 61c). Water contact angles of 78.9 ± 3.0 and 78.3 ± 1.6 were observed for Riddell and Schutt helmets at pre-season, respectively. However, water contact angle measurements were found too difficult for post-season measurements due to the high concentrations of scratches and gouges to the helmet surface. As a result, water contact angle is not viable measurement to monitor *in situ* helmet degradation.

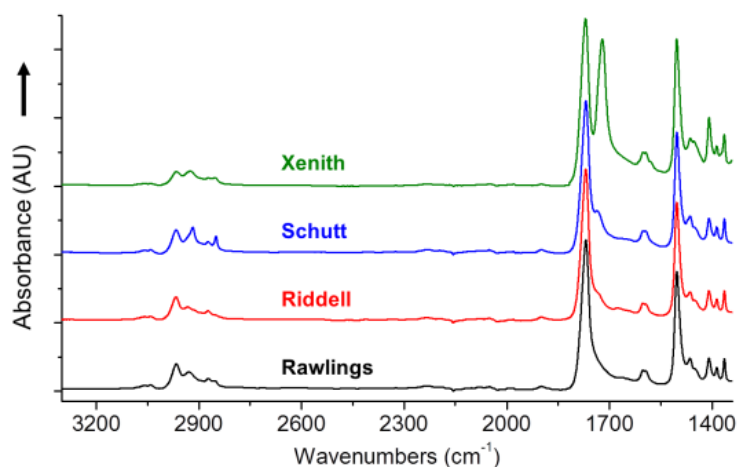


Figure 60. Full ATR-IR spectra across a representative American football helmet outer shell model from each of the four major helmet manufacturers.

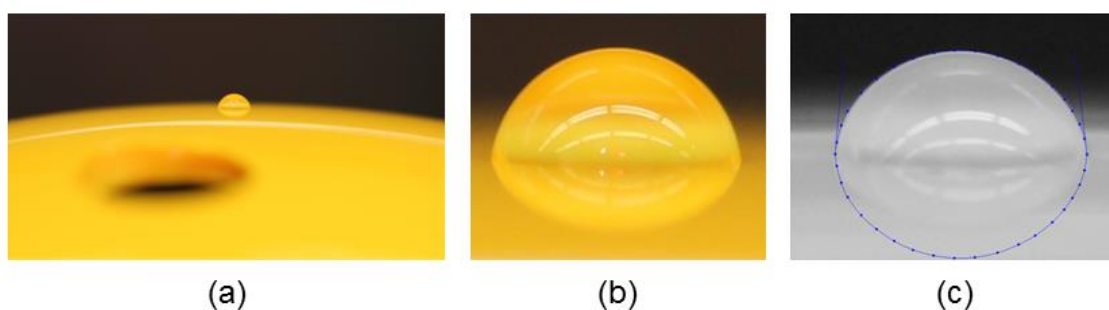


Figure 61. (a) High definition photograph of deionized water droplet on a helmet outer shell. (b) Zoomed in and cropped image imported into DropSnake Software. (c) Output image of analysis highlighting the water contact angle measurement in blue.

The ability to use current thermal and mechanical techniques may be limiting due to their destructive nature; however, assessments of property changes of helmet grade polymers under on-field environments is required. Preliminary work examined compared the linear thermal expansion between a helmet-grade plaque and an off-the-shelf helmet outer shell using thermo-mechanical analysis (TMA). The TMA protocol matched the protocol described in Chapter V, except that the Probe Force was set to 0.01 N. Examination of TMA thermograms (Figure 62) between conditions revealed seven distinctive transitions: (T1) onset at -75 °C, (T2) onset at 75 °C, (T3) onset at 140 °C, (T4) onset at 145°C, (T5) peak at 170 °C, (T6) trough at 185-195°C, and (T7) peak at

200-225°C. Analysis revealed equivalent thermogram plots with deviations in T6 and T7 peak temperatures. Further evidence was provided that the helmet-grade plaque material matched an off-the-shelf helmet outer shell (see Chapter III). In summary, the TMA protocol was substantiated towards the investigation of full helmet outer shells.

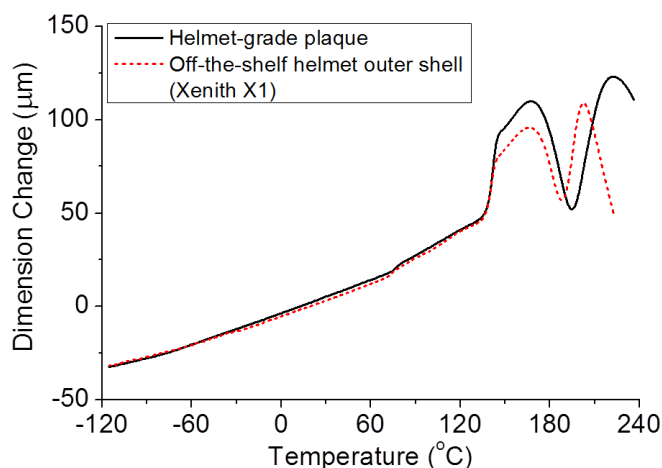


Figure 62. TMA thermograms between a helmet-grade plaque and an off-the-shelf shell.

Conclusions

The preliminary use of laboratory techniques to analyze full helmet outer shells exposed to end-use conditions has been substantiated. Further investigation should aim to optimize current ATR-FTIR, CIELAB, water contact angle, and TMA protocols, as well as incorporate additional techniques such as MDSC, DMA and nanoindentation. In order to understand how service life exposures precisely affect the on-field impact performance of full helmet systems, changes in material properties need to be quantified at the molecular, microscopic, and bulk levels. To improve upon current technologies, it is required to comprehensively understand the cumulative relationship between material aging and degradation, a decrease in impact performance, and the potential increased risk of head injury to the athlete throughout the lifecycle of the outer shell.

References

- 1 Kierkels JTA, Dona CL, Tervoort TA, et al. Kinetics of Re-embrittlement of (Anti)plasticized glassy polymers after mechanical rejuvenation. *J Polymer Science: Part B: Polymer Physics* 2007, 26:134-147
- 2 McKenna GB. Mechanical rejuvenation in polymer glasses: fact or fallacy? *Journal of Physics: Condensed Matter* 2003, 15:S737-S763
- 3 Lee JK, Kim JH, Chu HC, et al. Macroscopic observation of healing process in Stress-whitened polypropylene under hydrostatic pressure. *Polym Eng Sci* 2002, 42(12):2351-2360
- 4 Lee YW and Kung SH. Elimination of stress whitening in high-molecular-weight polyethylene. *J Appl Polym Sci* 1992, 46:9-18
- 5 Pae KD, Chu HC, Lee JK, et al. Healing of stress-whitening in polyethylene and polypropylene at or below room temperature. *Polym Eng Sci* 2000, 40(8):1783-1795
- 6 Brady JM. The effect of thermal aging on impact-modified engineering resins. *Polymer* 1992, 33(14):2981-2988
- 7 Cheng TW, Keskkula H, and Paul DR. Thermal aging of impact-modified polycarbonate. *J Appl Polym Sci* 1992, 45:531-551
- 8 Moss WC and King MJ. Impact response of US Army and National Football League helmet pad systems. 2011. Lawrence Livermore National Laboratory, DTIC Document.
- 9 Fisher E. NAERA Release - After Market Enhancements – Press Release. 2013. NAERA Organization.

- 10 Montgomery A. Certification to NOCSAE standards and Add-on Helmet Products. August 7 – Newsletter. 2013. National Operative Committee on Standards for Athletic Equipment
- 11 Walter KD. No evidence that helmet add-ons reduce concussion risk. *American Academy of Pediatrics*. Published online August 23, 2013.
- 12 EXO Skeleton CRT Product Brochure. 2012. Unequal Technologies Company